OPTICAL-FIBRE-BASED BIOMIMETIC ARTIFICIAL COMPOUND EYES

JIANG HENG

PhD

The Hong Kong Polytechnic University

2025

The Hong Kong Polytechnic University

Department of Applied Physics

OPTICAL-FIBRE-BASED BIOMIMETIC ARTIFICIAL COMPOUND EYES

JIANG HENG

A thesis submitted in partial fulfillment of the requirements for the degree of

Doctor of Philosophy

August 2024

Certificate of Originality

I hereby declare that this thesis is my own work and that, to the best of my knowledge and belief, it reproduces no material previously published or written, nor material that has been accepted for the award of any other degree or diploma, except where due acknowledgement has been made in the text.

(Signed)

JIANG Heng (Name of the student)

Abstract

Natural selection has driven arthropods to evolve fantastic natural compound eyes (NCEs) with unique anatomical structures, providing a promising blueprint for artificial compound eyes (ACEs) to perceive complex environments. NCEs have two main types – apposition and superposition – adapted for daytime and nighttime vision respectively. However, traditional ACEs have mostly been able to mimic only the apposition type, and have difficulties in achieving both static imaging and dynamic perception simultaneously. To address these limitations, this PhD research has developed two types of biomimetic ACEs that faithfully replicate the structures of NCEs. The thesis consists of three main parts:

The first part focuses on a novel artificial ommatidium, which is the basic imaging unit of ACEs. It is designed and fabricated using a conical-microlens plastic optical fibre, serving as flexible and nonbrittle light guides to collect and transmit light from a curved light detection surface to a flat imaging sensor chip. The conical microlens with a 35° half-apex angle and a rounded tip enables to lower the acceptance angle and improve the angular resolution of the plastic optical fibres. And a unique fabrication technique is developed using 3D printing, electroplating, and moulding processes to produce ~200 artificial ommatidia in a batch.

The second part is devoted to a novel apposition ACE, which is assembled using 271 artificial ommatidia. This ACE mimics the key anatomical structures of NCEs, including the facet lens, crystalline cone, rhabdom, and pigment cells. It demonstrated exceptional capabilities, such as a 180° field of view, real-time

panoramic direct imaging without distortions, and the ability to detect ultrafast angular motion up to 100 times faster than the response speed of dragonflies.

The third part turns to a new optic superposition ACE using the artificial ommatidia again but having a different arrangement. This ACE incorporates spatial and temporal adjustments in both hardware and software to perform well under 1000 times varying light intensities, including focus mode switching, binning mode, Gaussian spatial summation, and exposure time lengthening. The precise mimicry of NCE archetypes and anatomical structures enabled the superposition ACE to meet the requirements for both static and dynamic perception.

In summary, this thesis makes significant scientific contributions by developing exceptional biomimetic ACEs that faithfully replicate the anatomical structures of NCEs. The novel conical-microlens plastic optical fibres enable effective light transmission from curved to flat surfaces. The meticulously assembled apposition and superposition ACEs demonstrate unprecedented capabilities, outperforming natural systems in key metrics such as field of view, imaging speed, and motion detection. These remarkable biomimetic characteristics could facilitate applications of ACEs in emerging fields such as surveillance, unmanned drones, medical imaging, autonomous driving, and virtual reality.

List of Publications and Awards

Journal papers

[1] **Heng Jiang**, Chi Chung Tsoi, Weixing Yu, Mengchao Ma, Mingjie Li, Zuankai Wang, and Xuming Zhang*, "Optical Fibre based Artificial Compound Eyes for Direct Static Imaging and Ultrafast Motion Detection," *Light: Science & Applications*, vol. 13, no. 1, p. 256, 2024, DOI: 10.1038/s41377-024-01580-5.

[2] **Heng Jiang**, Chi Chung Tsoi, Lanrui Sun, Weixing Yu, Hao Fan, Mengchao Ma, Yanwei Jia, and Xuming Zhang*, "Biomimetic Curved Artificial Compound Eyes: A Review," *Advanced Devices & Instrumentation*, vol. 5, p. 0034, 2024, DOI:10.34133/adi.0034.

[3] **Heng Jiang**, and Xuming Zhang*, "Superposition Artificial Compound Eyes for Static and Dynamic Adaptive Light Perception," (to be submitted).

[4] Yu Du, Linjie Liu, Bingxuan Zhu, **Heng Jiang**, Xuming Zhang, and Chenxi Wang, "Low-temperature fusion bonding of aluminosilicate glass via intermediate water," Ceramics International, vol. 50, no. 7, Part A, pp. 10252-10258, 2024, DOI: https://doi.org/10.1016/j.ceramint.2023.12.335.

Conference papers

[1] **Heng Jiang**, Cheuk Lun Lau, and Xuming Zhang*, "Learn from butterfly's eyes," in *PolyU Academy for Interdisciplinary Research Conference 2023 (PAIR Conference 2023)*, 8-11 May 2023, Hong Kong, **Best Poster**

Presentation.

[2] **Heng Jiang**, Yu Du, Chi Chung Tsoi, and Xuming Zhang*, "Feasibility Study of Artificial Compound Eye using Optical Fibers," in *Progress In Electromagnetics Research Symposium 2023 (PIERS 2023)*, 3-6 July, 2023, Prague, Czech Republic, European Union.

[3] **Heng Jiang**, Yu Du, Chi Chung Tsoi, and Xuming Zhang*, "A Novel Artificial Compound Eye," in *Joint Annual Conference of Physical Societies in Guangdong-Hong Kong-Macao Greater Bay Area 2023*, 31 July-4 August 2023, Hong Kong.

[4] **Heng Jiang**, Chi Chung Tsoi, Weixing Yu, and Xuming Zhang*, "Bioinspired Cameras with 180^{o} Static Imaging and Optical Flow Detection," in *11th Asia-Pacific Conference of Transducers and Micro-Nano Technology 2024 (APCOT2024)*, 23 to 26 June 2024, Singapore.

Patents

[1] Xuming Zhang, **Heng Jiang**, and Chi Chung Tsoi. A microlens, Chinese Patent of Invention CN115437045B, 15 August 2023. (张需明，姜衡，蔡智聪，一种微透镜，中国发明专利，专利授权号：CN115437045B，授权时间：2023/8/15）

[2] Xuming Zhang, **Heng Jiang**, and Chi Chung Tsoi. An artificial compound eye imaging system, Chinese Patents of Invention CN115717933A, 7 March 2023. (张需明，姜衡，蔡智聪，一种人工复眼成像系统，中国发明专利，专利公开号：CN115717933A，公开时间：2023/3/7）

[3] Xuming Zhang, **Heng Jiang**, and Chi Chung Tsoi, A connection method

between optical fibre and microlens, Chinese Patent of Invention CN115437067A, 12 December 2022. (张需明，姜衡，蔡智聪，一种光纤与微透镜的连接方法，中国发明专利，专利公开号：CN115437067A，公开时间：2022/12/12）

Awards

[1] **Heng Jiang**, "Artificial compound eyes for full-vision camera (ACEcam) using lensed plastic optical fibers," in *Postgraduate Research Seminar 2022 (PRS2022)*, 15-24 August 2022, Hong Kong, **Best Presentation Award.**

[2] **Top Performer**, Micro Fund 2024/2025 Cohort 1.

[3] **Runner-up position** in the National Finals of the second “Guanghua Star” Optical Competition, Team leader, 2024. （第二届光华之星光学竞赛全国总决赛亚军，队长，2024）

Acknowledgements

When I was a child, I never imagined that I would one day pursue a Doctor of Philosophy degree. It is the support from many that has given me this opportunity. Therefore, I want to express my gratitude to all those who have helped me along the way.

First, I would like to thank my country, China. Thanks to the education provided by the government, I had the chance to learn essential knowledge. Although my primary school in the countryside was not as well-equipped as those in cities, the teachers there guided me with love and patience. As I grew older, I had the opportunity to attend better schools with financial support from my country. It is difficult to say whether I would have been able to attend university without the substantial efforts made by my country, including financial aid and the promotion of the importance of education. I also want to extend my thanks to the Hong Kong Special Administrative Region for giving me the opportunity to study at The Hong Kong Polytechnic University.

Second, I want to express my gratitude to Professor Xuming Zhang. He taught me a great deal, not only in scientific research but also in life. From him, I learned how to become a true man. His positive attitude has been a significant source of encouragement for me. He also taught me how to conduct meaningful scientific research and how to write effectively. I also want to thank my group mates: Dr. Huaping Jia, Dr. Fengjia Xie, Dr. Chi Chung Tsoi, Dr. Yao Chai, Dr. Yujiao Zhu, Ms. Yuhui Liu, Mr. Yu Du, Mr. Zirui Pang, Mr. Liang Wan, Ms. Wing Yan Leung, and Mr. Xu Li.

Third, I want to thank my parents. They have always understood and

supported my decisions, giving me the courage to pursue my dreams. Whenever I felt confused, it was also them who guided me with their love and patience.

Last but not least, I want to thank my friends. The time spent with them has brought me great happiness. I would like to specifically thank Mr. Zhongwen Bi. Our discussions on scientific research, philosophy, and economics have been mutually enriching, and I hope he obtains his PhD degree successfully.

Once more, thank you to everyone who has shown me love, patience, and support.

Table of Contents

List of Figures

List of Tables

Chapter 1 Introduction

1.1 Background

Natural selection drives the diversification of visual systems across biological organisms, facilitating adaptation for survival. Emulating natural visual mechanisms inspires the development of biomimetic imaging archetypes endowed with remarkable capabilities, including high resolution, expansive field of view (FOV), and agile motion detection sensitivity. Among these biomimetic imaging devices are artificial single-chamber eyes, emulating vertebrate ocular structures such as those found in humans, and artificial compound eyes (ACEs), replicating the multifaceted eyes of arthropods like bees (Fig. 1-1) [1]. Artificial single-chamber eyes employ a single imaging sensor chip to capture light information through lenses, resulting in superior imaging resolution. However, their FOV and motion sensitivity remain constrained.

ACEs, composed of numerous artificial ommatidia, provide another avenue for biomimetic imaging devices. In nature, the resolution of compound eyes is contingent upon the number of ommatidia, ranging from fewer than 20 in subterranean insects to several tens of thousands in dragonflies [2]. Consequently, the resolution of natural compound eyes (NCEs) typically falls below that of single-chamber eyes due to the limitation in the number of ommatidia. Conversely, owing to the distribution of ommatidia along a curved surface, the FOV of NCEs exceeds that of single-chamber eyes. Additionally, the flicker fusion frequency (FFF), indicative of motion sensitivity, in NCEs is nearly ten

times higher than that in natural single-chamber eyes (205 Hz in *Glossina morsitans* [3],[4] compared to 24 Hz in humans [5]). Thus, ACEs, which mimic NCEs, have the potential to harness these advantages.

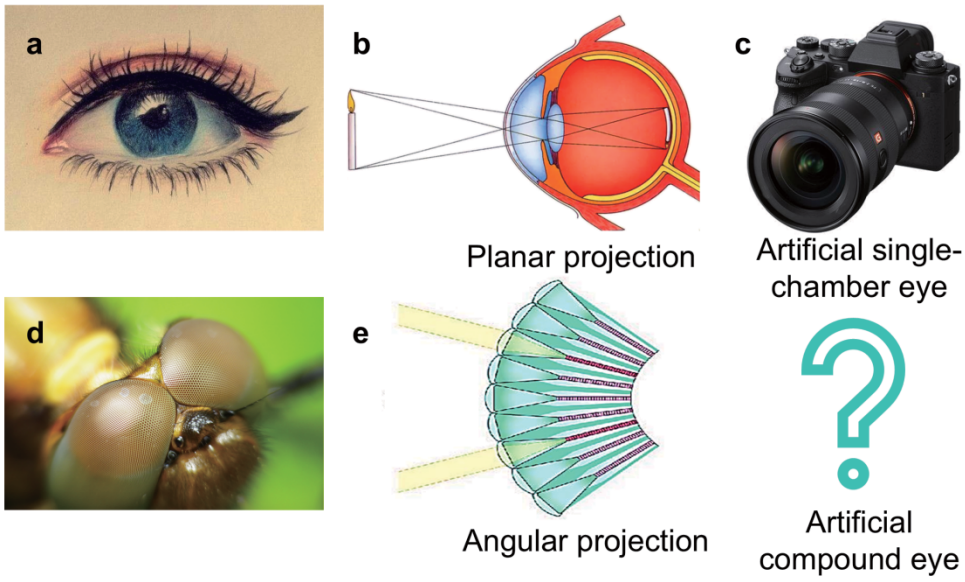

Figure 1-1. Natural visual systems and biomimetic imaging devices. a, Natural single-chamber eye. **b,** Imaging principle of natural single-chamber eyes. **c,** Cameras inspired by natural single-chamber eyes. **d,** Natural compound eye. **e,** Imaging principle of natural compound eyes.

ACEs, with their unique performance advantages, hold vast potential for extensive applications. For instance, their wide FOV enables them to excel in surveillance and unmanned drones. The infinite depth of field contributes to an enhanced sense of realism in augmented reality experiences. Their high motion detection capability facilitates kinestate tracking and motion state control in robots, unmanned aerial vehicles, and even spacecraft. Hence, the compelling dissection of ACEs is warranted.

Research on ACEs still faces numerous limitations. The FOV of most ACEs

is less than 180°, constraining their ability to receive light across a wide range. Furthermore, imaging with ACEs still requires post-processing, such as employing single-pixel imaging technique [6], scanning method with mapping algorithms [7],[8], and backpropagation neural networks [9], thus hindering direct imaging capabilities. Crucially, it is hard for the current ACEs to simultaneously satisfy the requirements for real-time direct imaging and dynamic motion detection. Additionally, most ACEs focus on the replication of apposition NCEs, not on the superposition NCEs due to the difficulty of mimicking the adjustment of anatomical structure and ganglia of superposition NCEs with circadian rhythm. As a result, ACEs cannot operate effectively under adaptive light intensities.

In this thesis, we will introduce two types of biomimetic ACEs that faithfully replicate the structures of NCEs. Self-designed conical microlensed plastic optical fibres function as the light guides in both ACEs to transmit the light from the curved light detection surface to a flat imaging sensor chip. The first apposition ACE achieves a 180° FOV, and enables real-time panoramic direct imaging, distance estimation, infinite depth of field, and ultrafast dynamic motion detection. The second optic superposition ACE further enhances these capabilities, particularly under adaptive light intensities. These imaging and ultrafast dynamic motion detection capabilities thus allow ACEs to find niche applications in various fields.

1.2 Objectives of research

The overarching objective of this thesis is to develop apposition and optic

superposition ACEs by replicating the anatomical structures and ganglia of NCEs. More specifically, three primary objectives will be pursued.

(1) A novel artificial ommatidium. The conical microlensed plastic optical fibre faithfully mimics the anatomic structure of the natural ommatidium to work as the artificial ommatidium, the basic imaging unit of ACEs. Specifically, optical fibres here serve as light guides, transmitting light from the curved light detection surface to a flat imaging sensor chip. Plastic optical fibres are selected for their flexible and non-brittle properties at large bending angles. However, the plastic fibres have a large acceptance angle and thus low angular resolution. Therefore, a suitable microlens that can reduce the acceptance angle of plastic optical fibres should be designed and fabricated.

(2) Apposition artificial compound eye. 271 conical microlensed polymer optical fibres (artificial ommatidia) are integrated into a dome-like structure to faithfully mimic the structure of apposition NCEs. This apposition ACE should enable real-time, 180^{o} panoramic direct imaging and depth estimation within its nearly infinite depth of field. Moreover, it should respond to an ultra-high angular motion with the ability to identify translation and rotation

(3) Optic superposition compound eye. This Optic ACE using the artificial ommatidia again but having a different arrangement, employs spatial and temporal adjustments in both hardware and software, including focus mode switching, binning mode, Gaussian spatial summation, and exposure time lengthening, to accurately replicate the adjustments in the anatomical structure and ganglia of optic NCEs, enabling optimal performance under varying light intensities.

1.3 Outline of thesis

Chapter 1 introduces the background of ACEs. The motivations and objectives of this doctoral research are also included in Chapter 1.

Chapter 2 provides a comprehensive literature review of biomimetic curved artificial compound eyes (BCACEs), which are closely associated with the ACEs proposed in this thesis. A series of parameters are introduced to delineate the characteristics of BCACEs. Following this, two primary types of BCACEs are introduced, each with further sub-categories. The chapter further explores fabrication methods and applications related to the BCACEs.

Chapter 3 presents the first work: design and fabrication of a novel artificial ommatidium. Theoretical optical path analysis and simulations reveal that a conical microlens with a 35° half-apex angle and a rounded tip can reduce the acceptance angle of plastic optical fibres from 60° to about 45°. A unique batch fabrication technique for these conical microlensed plastic optical fibres is also developed.

Chapter 4 exhibits the second work: optical fibre (artificial ommatidium) based apposition artificial compound eyes for direct static imaging and ultrafast motion detection. An apposition ACE is assembled using 271 of these conical microlensed plastic optical fibres and characterized. This assembled ACE faithfully mimics the anatomic structure of NCEs and thus obtains 180° real-time panoramic direct imaging without distortions across a nearly infinite depth of field and ultra-fast dynamic motion detection ability.

Chapter 5 reports the third work: optic superposition artificial compound eyes for static and dynamic adaptive light perception using the artificial

ommatidia again. The precise adjustment of anatomical structure and ganglia of NCEs are mimicked in this chapter. Specifically, spatial (mode switch and Gaussian spatial summation) and temporal (longer exposure time) approaches are implemented to enhance the ACE's ability to perceive static and dynamic perception under adaptive light intensities.

Chapter 6 is the conclusions and future work. At first, the novel artificial ommatidium and ACEs mentioned in this thesis are briefly concluded. Then several advancements are proposed: (1) incorporating micro apertures to further reduce the acceptance angle of plastic optical fibres and increase angular resolution; (2) combining microfluidic technology with coherent image optical fibre bundles to achieve 180^{o} high-resolution imaging with tunable focal length, thereby mimicking the integration of vertebrate single-chamber eyes and NCEs.

Chapter 2 Literature review

In this chapter, biomimetic curved artificial compound eyes (BCACEs) will be reviewed. This work starts with a simple classification of NCEs and then provides a comprehensive review of main parameters, operational mechanisms, recent advancements, fabrication methodologies, and potential applications of BCACEs. Finally, discussions are provided on future research and development.

2.1 Introduction of BCACEs

In 1665, Robert Hooke discovered that the cornea of a grey drone fly, in which *Pearls* (i.e., corneal facet lenses) were orderly arranged, was fundamentally different from that of a human being [10]. This discovery marked the beginning of the observation and research of NCEs. Two centuries later, another renowned biologist, Sigmund Exner, proposed the concept of the basic unit of an NCE, which was so-called the ommatidium [11]. A typical ommatidium collects light at a specific angle through a corneal facet lens and then conveys it to the photoreceptor cells via a crystalline cone and a rhabdom (light guide) (see Fig. 2-1a). Axon bundles subsequently innervate ommatidia through synaptic connections in lamina cartridges. Deeper neural centers (medulla and lobula) process the primary signals before transmitting the information to the central

brain (see Fig. 2-1b).

The NCEs have several types of anatomical structures [12] as illustrated in Fig. 2-1b-d (to be elaborated in section 2.2), which are very different from other types of eyes [13]. The NCEs offer significant advantages, including wide FOV, exceptional motion detection sensitivity, and an infinite depth of field. Specifically, wide FOV is easy to understand based on Fig. 2-1. The exceptional motion detection sensitivity can be attributed to two key factors. Firstly, the miniature vision of NCEs significantly diminishes the signal transmission distance between the photoreceptor and the brain. Secondly, NCEs exhibit a non-spiking graded signal transmission rate between the retina and lamina neurons (1,650 bit s^{-1}), surpassing that of human spiking neurons (~300 bit s^{-1}). This discrepancy arises from the presence of a refractory period in spiking neurons, imposing constraints on the speed of information transmission [14],[15]. The infinite depth of field is a result of the low acceptance angle of each ommatidium, causing incident light to approach near parallelism. ACEs that replicate NCEs can also harness these benefits. Consequently, they have found niche applications in various micro-optics fields such as micro-cameras [16], medical imaging [17], and elementary motion detectors [18]. Noteworthily, ACEs and artificial retinas are truly mirror concepts, with the former mimicking the natural compound eyes of arthropods for panoramic perception and high-speed dynamic motion detection, while the latter emulates the retinas of vertebrates' eyes to assist in the improvement of visual loss in the fields of medicine and bioengineering [19].

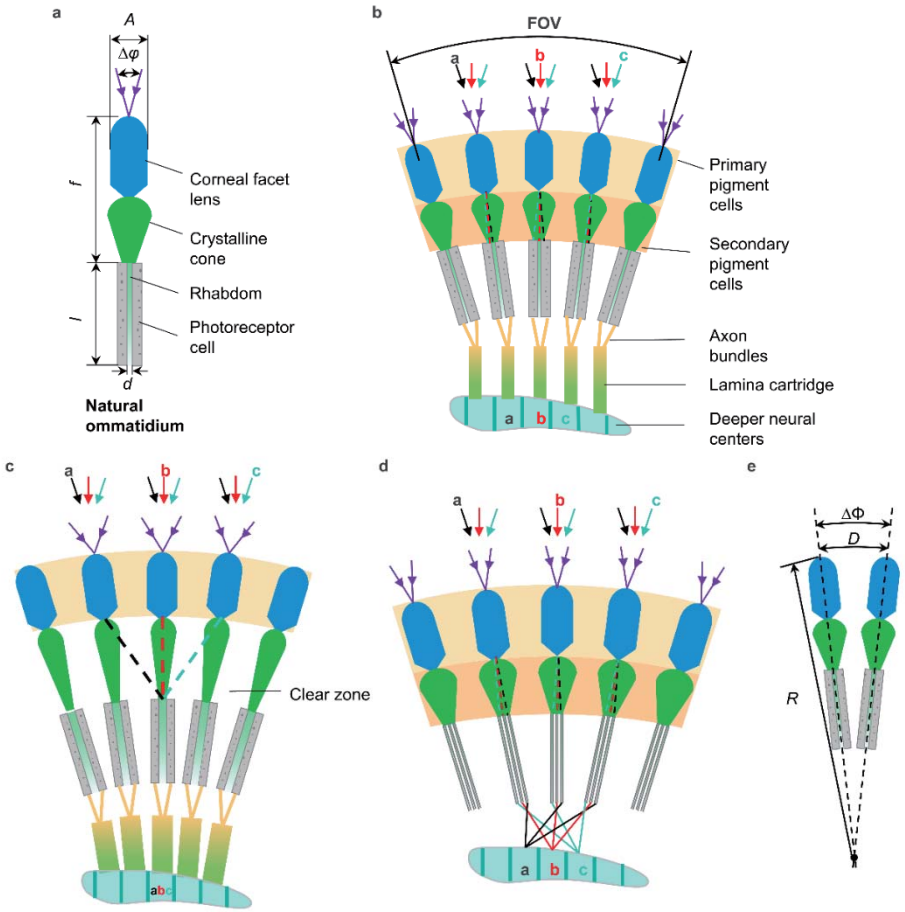

Figure 2-1. Schematic diagrams of natural compound eyes. a, Natural ommatidium. **b,** Apposition natural compound eye. **c,** Optic superposition natural compound eye. **d,** Neural superposition natural compound eye. **e,** Interpretation for inter-ommatidial angle.

ACEs can be generally divided into three categories: planar micro-lens arrays, artificial compound eyes using metalenses, and biomimetic curved artificial compound eyes (BCACEs). With regard to the first one, all micro-lenses are arranged in a plane to replace a single lens with higher resolution and variable focal lengths. A few reviews have covered the progress and implementation of planar micro-lens arrays [20]-[24]. Nussbaum gave a comprehensive discussion of the planar ones on their designs and fabrications

[20], emphasizing properties of plano-convex micro-lens arrays (e.g., radius of curvature, focal length, and packing density), fabrication techniques (e.g., reflow method, reactive ion etching), testing methods, and potential applications. On this basis, some planar micro-lenses were proposed with fixed and tunable focal lengths [21],[24]. For example, Brückner et al. reported an approach to stitch the partial images recorded by planar micro-lenses to compose a conclusive image of the entire field of view [21]. Similarly, Tanida [22] and Shankar et al. [23] presented their designs with ultra-thin multiple channels. Additionally, Ren reported a dielectrophoresis-based tunable-focus liquid micro-lens array [24]. However, the planar micro-lens arrays usually have very limited FOV, therefore this type will not be discussed further.

Metalenses consist of a 2D array of subwavelength scatterers that manipulate wavefronts, inducing abrupt phase changes at the interface. Through the precise design of the geometrical nano-parameters of these scatters, incident light from various directions is efficiently scattered into the substrate via discrete nano-building blocks, generating photocurrents [25]-[28]. The utilization of metalenses in the design of ACEs represents an emerging approach, pointing towards a promising future. When compared to traditional BCACEs, ACEs incorporating metalenses exhibit several merits, such as a FOV (e.g., 170^{o} [25]) comparable to that of most BCACEs, a more compact design, and the potential to overcome chromatic aberration effects [26]. However, this type of ACE also encounters certain limitations. For example, its focusing efficiency at the edge is much lower than at the centre (e.g. 45% at an incident of 85^{o} compared to 82% at a normal incident [25]); it is challenging for metalens-based ACEs to achieve or surpass a FOV of 180^{o}, which may be more feasible for BCACEs. It is important

to note that while an artificial compound eye utilizing metalenses operates by amalgamating separate light information from a wide FOV like an NCE, its underlying specific working principle deviates significantly from that of an NCE. Therefore, it is pertinent to mention that the details of this deviation from NCE principles are beyond the scope of this paper.

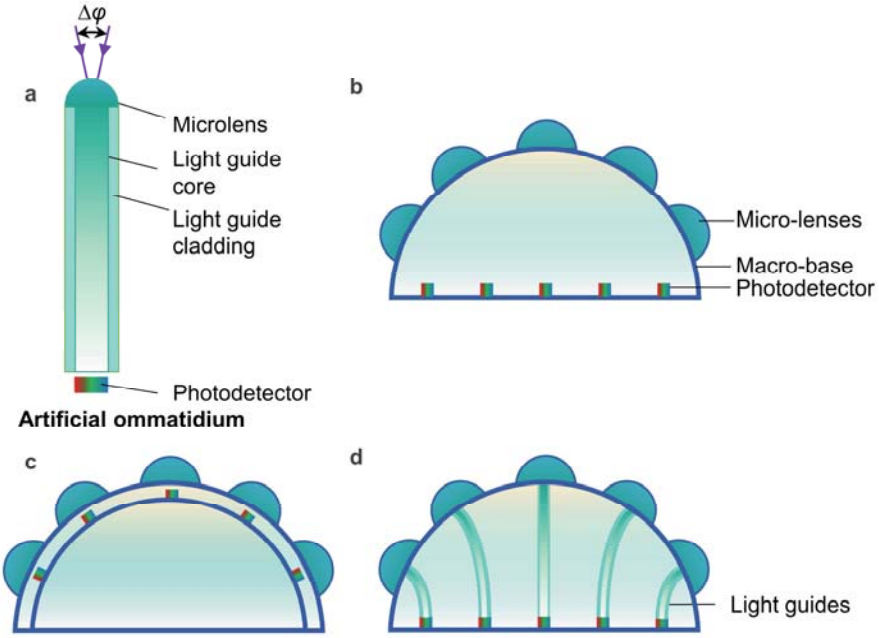

Figure 2-2. Schematic diagrams of BCACEs. a, Artificial ommatidium. **b,** Simplified BCACE. **c,** BCACE with a photodetector array within a curved surface. **d,** BCACE with light guides.

Regarding BCACEs, the fundamental structural unit is the artificial ommatidium, comprising several key components: the micro-lens (dispersed across a curved surface to ensure perpendicularity to panoramic light), a cone with dielectric properties (mimicking the crystalline cone in nature to facilitate the guidance of focused light from the micro-lens into the light guide core), the light guide core (analogous to the rhabdom found in nature), light guide cladding, and the photodetector, as shown in Fig. 2-2a. Therefore, BCACEs possess a

broad FOV, minimal geometric aberration (although other aberrations such as chromatic aberration and astigmatism may still remain), exceptional optical uniformity, resolution, and sensitivity, rendering them suitable for a broader spectrum of applications.

The investigation of BCACEs experienced a tortuous process. Fig. 2-3 summarizes the categories of BCACEs. According to the reported designs of BCACEs, two types exist: ones with fixed focal lengths and ones with tunable focal lengths, meaning that the focal length of the former's micro-lens array is fixed while the latter's can be altered. In the case of fixed focal length BCACEs, some research was devoted to designing and optimizing simplified BCACEs [29]-[32]. The reason to call this kind of BCACEs simplified BCACEs is that they are typically composed of a curved macro-base and a micro-lens array (not completed ommatidia, Fig. 2-2b). Because of the imperfection, it is difficult to ensure light from each micro-lens focuses on the same detection plane, especially when the number of micro-lenses is large. Therefore, some researchers proposed BCACEs with photodetector arrays within curved surfaces as shown in Fig. 2-2c [7],[8],[33]-[35]. Although it is promising to use a photodetector array within a curved surface to record the light information from the curved micro-lens array, it still suffers hard fabrication and reproduction. In this way, some researchers proposed the BCACEs with light guides as shown in Fig. 2-2d [6],[9],[36]-[40]. With the help of light guides, the photodetector array within a curved surface can be replaced by the planar photodetector array, increasing the robustness of the BCACEs. Besides, such BCACEs are more similar to NCEs in anatomic structures.

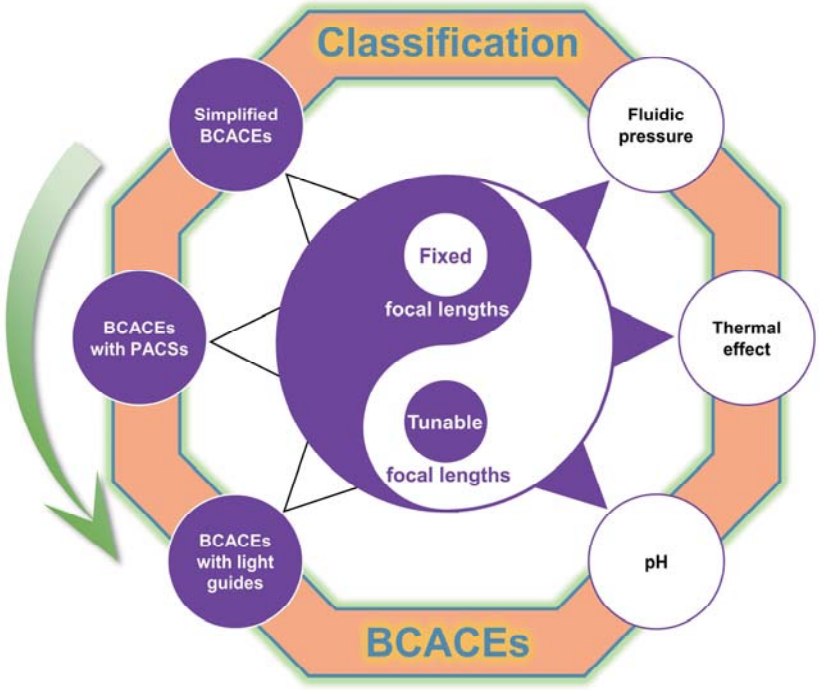

Figure 2-3. Category of biomimetic curved artificial compound eyes (BCACEs), PACSs representing photodetector arrays within curved surfaces.

In the case of tunable-focal-length BCACEs, they can be classified into distinct groups depending on the techniques utilized to alter the shapes of micro-lenses in order to finally modify the focal lengths, for example: fluidic pressure [41],[42], thermal effect [43],[44], and pH [45].

This chapter is divided into eight sections. Section 2.1 introduces the concept of BCACEs. In section 2.2, we offer an in-depth exploration of NCEs. Moving on to section 2.3, we propose several parameters for evaluating BCACEs. Section 2.4 provides a detailed discussion of BCACEs, focusing on their operational mechanisms. Moving on to section 2.5, we present various fabrication methods for BCACEs. Additionally, section 2.6 showcases some applications, followed by a brief discussion in section 2.7. Finally, we conclude

the article in section 2.8.

2.2 Classification of natural compound eyes

NCEs can be specifically classified into three distinct types: *apposition* NCEs, *optic superposition* NCEs, and *neuron superposition* NCEs [46]. Apposition NCEs typically arrange ommatidia along a curved surface and separate them with pigment cells (see Fig. 2-1b). Due to the small diameter of the rhabdom and the presence of pigment cells, the light information from each ommatidium can only be focused on its corresponding rhabdom and transmitted to the corresponding deeper neural centre. Consequently, the acceptance angle of each ommatidium is limited (approximately 1° for bees [47],[48]), resulting in high resolution. However, this limited acceptance angle also leads to low optical sensitivity. Therefore, such NCEs are typically found in diurnal insect eyes.

Optic superposition NCEs are similar to the apposition type during the day, apart from a longer crystalline tract in the clear zone (see Fig. 2-1c) and a larger rhabdom diameter. This larger rhabdom diameter results in a broader acceptance angle for optic superposition NCEs (e.g., 19° for moths during the day, data sourced from ref [49],[50]). While the increased acceptance angle reduces imaging resolution, it enhances sensitivity to light. When dim light is present, pigment migration causes light from neighbouring micro-lenses to converge onto one rhabdom through the clear zone [51]-[53], further increasing the optical level in one rhabdom. Therefore, such NCEs are better suited for insects adapted to nocturnal life and low-light conditions [46].

In contrast to the previously mentioned NCEs with fused rhabdoms, neural superposition NCEs feature separate rhabdomeres, each receiving light input from different visual axes, representing different points in the environment (see Fig. 2-1d). Axons from each individual rhabdomere transport light input originating from the identical visual axis but emerging from separate ommatidia, ultimately converging into a shared lamina cartridge [46]. This configuration allows for both high resolution and high optical sensitivity at the cost of complex anatomical structures.

2.3 Characteristics of biomimetic curved artificial compound eyes

The evaluation of BCACEs in this section focuses on two key merits: panoramic imaging and high sensitivity to motion. In terms of the former, we consider factors such as FOV, acceptance angle of each ommatidium, inter-ommatidial angle, imaging quality, and optical sensitivity. Regarding the latter, the emphasis is on illustrating the highest angular perception speed.

2.3.1 Field of view

The concept of FOV originates from NCEs, as illustrated in Fig. 2-1b. It represents the collective acceptance angle of compound eyes and serves as a crucial parameter to showcase the panoramic imaging and dynamic motion detection capabilities of BCACEs.

2.3.2 Acceptance angle of each ommatidium

The acceptance angle of each ommatidium, denoted as $\Delta\varphi = d/f$, is also derived from NCEs [7],[47]. Here, d represents the rhabdom diameter, while f signifies the focal length of the facet lens (see Fig. 2-1a). In some assays [33],[39], the full width at half maximum (FWHM) of the angular sensitivity function (ASF) is roughly to be seen as the acceptance angle. This parameter serves as a critical element in determining the resolution and optical sensitivity of the compound eye.

2.3.3 Inter-ommatidial angle

The inter-ommatidial angle, denoted as $\Delta\Phi = D/R$, is defined as the angular separation between two neighbouring ommatidia. Here, D represents the arc distance between neighbouring ommatidia, while R signifies the local radius of curvature. Typically, this parameter is either equal to or slightly larger than $\Delta\varphi$ for apposition compound eyes. This is because if $\Delta\Phi$ were much larger than $\Delta\varphi$, there would be a significant gap between neighbouring ommatidia, resulting in a loss of light information. Conversely, if $\Delta\Phi$ were smaller than $\Delta\varphi$, there would be substantial overlap between neighboring ommatidia, leading to a reduction in resolution. While this parameter is derived from NCEs [47], as shown in Fig. 2-1e, it can also be applied to evaluate BCACEs using the same definition.

2.3.4 Quantitative imaging performance metric

The Modulation Transfer Function (MTF) serves as a ubiquitous parameter employed for evaluating the imaging quality of an optical system. It represents the system's ability to transfer input modulation to output modulation. Typically,

MTF is calculated by dividing the output contrast by the input contrast, with contrast C defined as:

$$C = \frac{I_{\max} - I_{\min}}{I_{\max} + I_{\min}}, \tag{2-1}$$

where $I_{\max}$ and $I_{\min}$ represent the maximum and minimum intensities of the object, respectively. Additionally, MTF is graphically represented with the x-axis representing spatial frequency (light pairs per micrometre, lp/mm), and the y-axis representing MTF. MTF serves as a crucial parameter for evaluating the imaging quality of BCACEs. However, it is important to note that BCACEs in their current stage exhibit poor imaging quality, to the extent that they can not even be effectively assessed using MTF. Looking ahead, as BCACEs continue to undergo rapid development and improvements in imaging quality, MTF can become a genuinely valuable tool for their evaluation.

2.3.5 Optical sensitivity

The term optical sensitivity S describes the light-gathering abilities of compound eyes under varying light intensities. When dealing with a broad-spectrum light source, S behaves as follows,

$$S = \left(\frac{\pi}{4}\right)^2 A^2 \left(\frac{d}{f}\right)^2 \left(\frac{kl}{2.3 + kl}\right), \tag{2-2}$$

and if the light source is monochromatic, S follows

$$S = \left(\frac{\pi}{4}\right)^2 A^2 \left(\frac{d}{f}\right)^2 \left(1 - e^{-kl}\right), \tag{2-3}$$

where A, d, f, k, and l denote the diameter of the compound eye's aperture, the diameter of the rhabdom, the focal length, the absorption coefficient of the photoreceptor cells on the rhabdom, and the length of the rhabdom, respectively

(see Fig. 2-1a) [54]. In both equations, $(\pi/4)^2A^2$ accounts for the sectional dimension of the ommatidium, (d/f) is the acceptance angle of the ommatidium, and $kl/(2.3+kl)$ and $(1-e^{-kl})$ represent the light absorption abilities. Therefore, the optical sensitivity S is subject to the size, the acceptance angle, and the light absorption ability of ommatidia. In a similar matter, this nature-inspired parameter can be employed for the evaluation of BCACEs.

2.3.6 Highest angular perception speed

If one BCACE is employed to track an object moving from one side of the BCACE to the opposite side, the time Δt can be determined as follows:

$$\Delta t = \frac{\mathrm{FOV}}{\omega}, \tag{2-4}$$

where ω symbolizes the angular speed. Each BCACE has the lowest detection interval time Δt_{dec}. For example, if the photodetector of the BCACE is a complementary metal oxide semiconductor (CMOS) chip, Δt_{dec} is determined by the frame rate of the CMOS. Obviously, Δt should not be smaller than Δt_{dec}, i.e.,

$$\Delta t \geq \Delta t_{dec}, \tag{2-5}$$

and thus,

$$\frac{\mathrm{FOV}}{\omega} \geq \Delta t_{dec}. \tag{2-6}$$

Here, the highest angular perception speed can be expressed as

$$\omega_{\max} = \frac{\mathrm{FOV}}{\Delta t_{dec}}. \tag{2-7}$$

2.4 Classification of BCACEs

Table 2-1. Comparison of typical biomimetic curved artificial compound eyes

Type of BCACE	Num-bers of ommat-idia	Shape of micro-lenses	BCACE radius	Field of view (Max-imum)	Materials	Fabrication methods	Ref
Ones with fixed focal lengths							
Simplified BCACEs	61	Round	4.33mm	48°	PDMS*	-	[29]
	-	Hexagon	40μm	60°	SU-8 resin	Laser direct writing	[30]
	19	Hexagon	45μm	120°	SU-8 resin and PDMS	Laser direct writing	[31]
	581	Round	-	108°	PDMS, silicon, photoresist et al.	Lithography, plasma etching, gas-assisted deformation et al.	[32]
BCACEs with PACSs†	180	Round	6.96mm	160°	PDMS, silicon, silicone, et al.	Combine, stretch, and et al.	[7]
	630	Round	6.4mm	180°× 60°	Glass, printed circuit board, et al.	Dicing, bending, and et al.	[33]
BCACEs with light guides	8370	Hexagon	1.25mm	-	PDMS, silicon, photoresist et al.	Lithography and gas-assisted deformation.	[36]
	522	Hexagon	2.5mm	170°	Acrylate resin, UV-curable diacrylate polymer, and silicone	Projection micro stereo-lithography 3D printing and microfluidic assisted moulding technique	[39]
Ones with Tunable focal lengths							
Fluidic pressure	100	Round	50mm	-	PDMS	-	[41]
	9	Round	-	120°	PDMS, SU-8	Lithography	[42]
Thermal effect	~900	Round	-	160°	Graphene	Template-directed self-assembly method	[43]
	3	Round	-	-	PDMS, N-isopropyl-acrylamide, and et al.	Lithography	[44]
pH	7(fixed base)	Hexag-on	32μm (tunable base) 50um (fixed base)	80°	Bovine serum album protein and SU-8 resin	Laser direct writing	[45]

*: Polydimethylsiloxane

†: Photodetector arrays within curved surfaces

Within this section, the discussion will delve further into BCACEs, specifically exploring their operational mechanisms. Firstly, we will introduce three types of BCACEs with fixed focal lengths. Subsequently, various methods for altering the

focal lengths of BCACEs will be discussed. A general comparison of representative BCACEs is provided in Table 2-1.

2.4.1 BCACEs with fixed focal lengths

2.4.1.1 Research on simplified BCACEs

During the initial stage of the research, researchers were devoted to the layout of micro-lenses in an ordered manner (compactness had not yet been deliberated). For example, as shown in Fig. 2-4a, Li's group [29],[55],[56] suggested dividing the curved surface of the BCACE into three equal sections, each spanning an angle of 120° (distinguished by different colours: red, yellow, and green), with each section having a distinct focal length, ultimately enabling limited zoom capability. To ensure that all micro-lenses on the curved surface effectively converge light onto a planar photodetector array, micro-lenses in each segment are categorized into five tiers based on their deviation angle concerning the central micro-lens, as shown in Fig. 2-4b.

The effective focal lengths of micro-lenses at all tiers can be determined through the thin lens manufacturing equation:

$$\frac{1}{f_n} = \left(n_i - 1\right)\left(\frac{1}{r_n} - \frac{1}{R}\right), \tag{2-8}$$

where f_n represents the effective focal length of the nth micro-lens, r_n denotes the radius of curvature of the nth micro-lens, R signifies the radius of the curved surface base, and n_i stands for the refractive index of the material used for this simplified BCACE. By using this formula, the effective radii of micro-lenses can be estimated, and then all micro-lenses can be designed by using Zemax to focus onto a planar photodetector array. However, as the number of micro-lenses

increases, this method becomes increasingly challenging due to the inherent design drawbacks and the complexity involved in both design and fabrication.

Furthermore, Lian's team developed a simplified form of BCACE (Fig. 2-4c) in an effort to enhance compactness [32]. However, Lian's design has an inverted light path compared to Li's design, where light passes through the micro-lenses on the curved surface and focuses onto a plane as shown in Fig. 2-4d. It follows an optical path from one point or plane to another, without directly addressing the intricate light propagation from the curved surface to a plane.

Moreover, the round lens shape and fill factor (FF, the ratio of the area which directs light to the photo-sensor, to the total contiguous area occupied by the microlens array, approximately 50-70%) of the aforementioned BCACE are significantly distinct from those found in natural ones, leading to a considerable impact on the signal-to-noise ratio. In this way, Wu's lab optimized the shape of the micro-lens as a hexagon to achieve a 100% fill factor so as to achieve a favourable light signal-to-noise ratio as depicted in Fig. 2-4e&f [30]. To assess the optical performance of this design quantitatively, they measured the point spread functions (PSFs) along the *x* and *y*-axes, as illustrated in Fig. 2-4g&h. These measurements were then compared with those of a single reference lens, depicted in Fig. 2-4i&j. The results show that the FWHM of this BCACE remains stable, even when exposed to tilted incident light., while the FWHM of a single lens increases dramatically, showing that the imaging distortion of Wu's design is tiny.

Similarly, Jin's team also fabricated hexagonal-shaped compound eyes with different numbers of micro-lenses as shown in Fig. 2-4k&l, showing that the hexagonal shape had a high optical imaging uniformity [31].

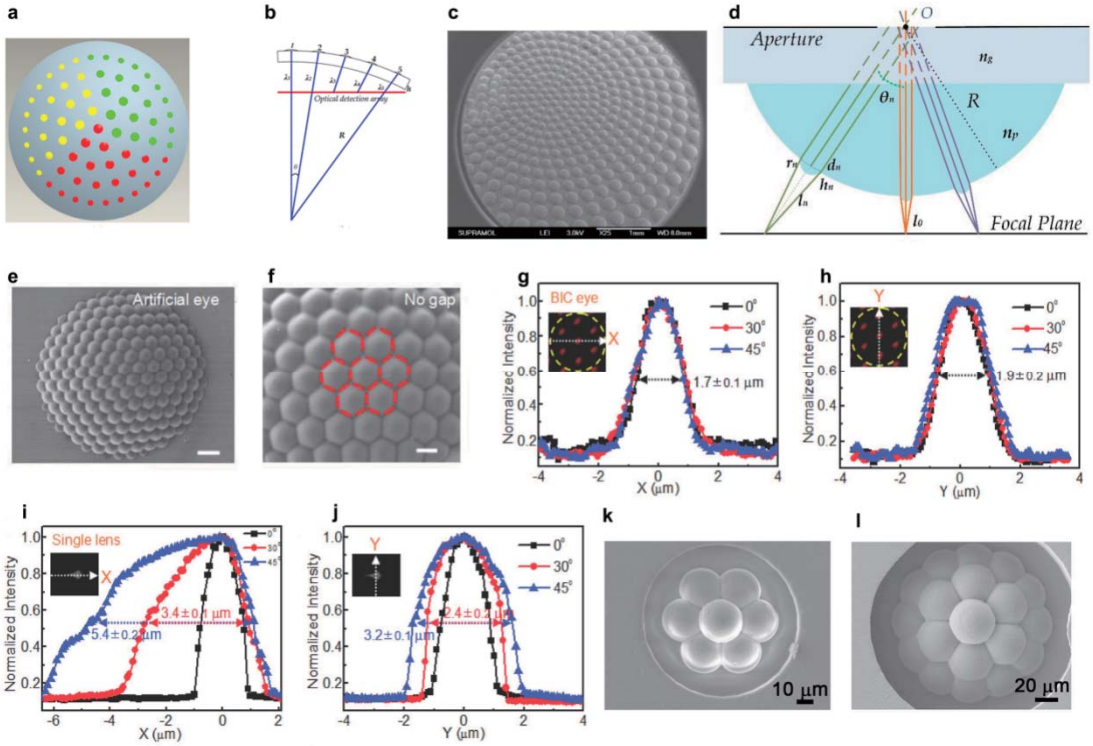

Figure 2-4. Simplified BCACEs. a, Area division of the variable focus surface compound eye proposed by Li's group, where the three different hues represented the three regions divided. **b,** Positional relationship between micro-lenses and the focus planes at all levels: *R*-curved base radius; θ-suborbital deflection angle; λ_{1-5}-distance between the micro-lenses and the optical detection array [29]. **c,** Scanning electron microscopy (SEM) image of Lian's BCACE at side view. **d,** Light path design of Lian's BCACE [32]. **e,** Top-view SEM images of Wu's BCACE. **f,** 30°-Tilted magnified SEM images of the BCACE and the 100% FF of hexagonal micro-lenses. **g, i,** Comparison of *x*-direction PSF for Wu's BCACE and single micro-lens. **h, j,** *y*-direction PSF of Wu's BCACE and a single lens. The insets in g-j are the focus spots of Wu's BCACE and single micro-lens under 30° light incidence [30]. **k,l,** 3D images of Jin's BCACE with 7 micro-lenses **(k)** and 19 micro-lenses **(l)** [31].

Here, simplified BCACEs primarily concentrate on the micro-lenses situated on the curved surface. Despite the principal role of micro-lenses within the compound eye, in-depth research into numerous other critical components is lacking, resulting in several inherent limitations. For example, the absence of pigment cells leads to severe crosstalk between neighbouring ommatidia. Similarly, despite certain endeavours being made to direct the light from micro-lenses onto a focal plane, due to the absence of effective light guides, it is a significant challenge to design and fabricate this kind of compound eye with satisfactory FOV and image resolution. Correspondingly, BCACEs with photodetector arrays within curved surfaces and BCACEs with light guides attempt to address these challenges.

2.4.1.2 Research on BCACEs with photodetector arrays within curved surfaces

Since a solo micro-lens array component was unable to effectively focus light onto a common planar photodetector as the number of micro-lenses increased, researchers thus explored the possibility of replacing the planar photodetector array with a curved one. By ensuring a proper spatial relationship between each micro-lens and photodetector, it is possible for the micro-lens to successfully focus light onto its corresponding photodetector. Regarding this kind of BCACE, some researchers focused on constructing a system and testing its static characteristics [7], while others researched dynamic characteristics [33].

Specifically, Song et al. proposed a type of BCACE inspired by the arthropod eye and tested it [7],[34]. As shown in Fig. 2-5a, the two major subsystems are combined to form the hemispherical apposition compound eyes,

the top subsystem providing optical imaging function and defining the overall mechanics which comprises 180 effective micro-lenses, and the bottom subsystem, responsible for photodetection and electrical read-out, comprising a complementary array of photodiodes and blocking diodes [7]. Following a series of dimensional and material selections, each photodiode is positioned at the focal point of a corresponding micro-lens to create an integrated imaging system, as depicted in Fig. 2-5b. In consequence, both subsystems are combined and stretched from the planar layout to the hemispherical shape under the hydraulic actuation as shown in Fig. 2-5c. Furthermore, an upper perforated sheet and a lower bulk support (see Fig. 2-5e) are constructed from black silicone to minimize stray light. Here, the black silicone is made by mixing the carbon black powder (Strem Chemical) into a thin silicone film membrane (Ecoflex, Smooth-on), which undergoes laser machining. In addition, there is a thin film insert featuring metalized contact pads that connect to a printed circuit board, serving as an interface for external control electronics. These combined subsystems are bonded together to constitute the complete apposition compound eye, as depicted in Fig. 2-5d. Therefore, a BCACE is obtained, with the micro-lenses and the supporting posts as corneal lenses and crystalline cones respectively, and photodiodes as photoreceptors on the rhabdom, as compared with NCEs.

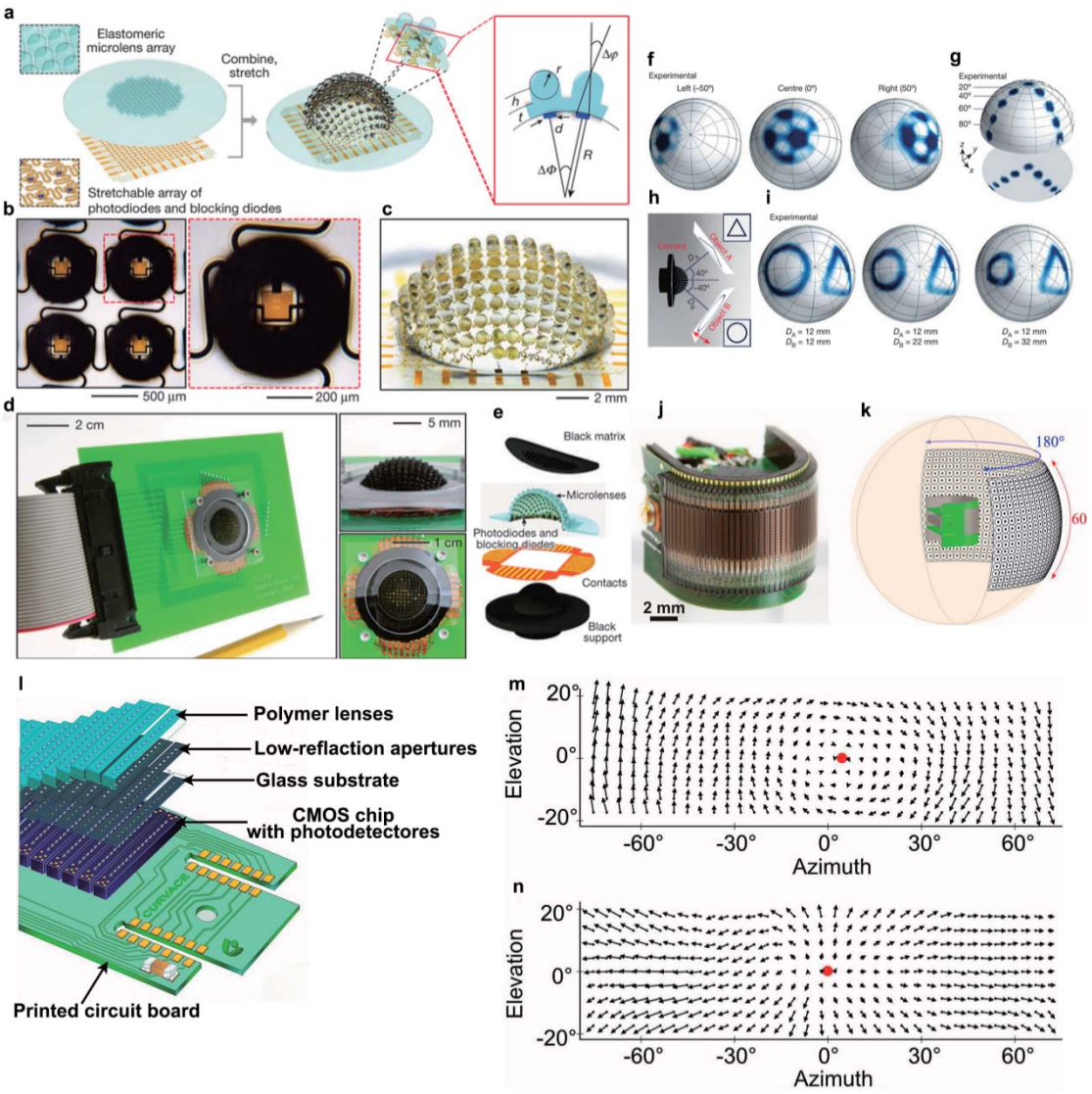

Figure 2-5. BCACEs with photodetector arrays within curved surfaces. a-i, BCACE proposed by Song's group [7]. **a,** Illustrations of an array of elastomeric micro-lenses and their supporting posts connected by a base membrane, as well as a corresponding array of silicon photodiodes and blocking diodes interconnected. **b,** Optical micrograph of four adjacent ommatidia in a flat configuration (on the left), along with an enlarged view (on the right). **c,** Image of a representative system after hemispherical deformation. **d,** Photograph of a finished compound eye installed on a printed circuit board, serving as an interface to external control electronics (on the left), with close-up views in the insets. **e,** Exploded-view illustration of this BCACE components. **f,** Images of a

soccer ball illustration taken from three distinct polar angles in relation to the camera's centre. **g,** Composite image displaying the sequential illumination of the compound eye using a collimated laser beam at nine different angles of incidence, shown on a hemispherical surface (top) and projected onto a plane (bottom). **h,** Schematic illustration of an experimental arrangement designed to illustrate essential imaging characteristics. One object (object A, marked as a triangle) is positioned at an angular location of 40° with a distance of D_A, while the other (object B, denoted as a circle) is at -40° with a distance of D_B. **i,** Photographs of these objects captured at various D_B values. **j-n,** BCACE proposed by Floreano's group [33]. **j,** Image of the prototype. **k,** Illustration of the panoramic FOV of the prototype. **l,** Scheme of the three layers that compose this BCACE. **m&n,** Dynamic optical flow detection involving the identification of a red dot as the centre or focal point of motion. **m,** Rolling motion toward a wall adorned with random black and white patterns. **n,** Linear translation toward this wall.

Some static experiments were thereby carried out. Since photodiodes are discrete, the scanning procedure is imperative for the ultimate formation of an image. In Fig. 2-5f, images of a line-art soccer ball illustration positioned at three distinct angular orientations: -50° (left), 0° (centre), and 50° (right) demonstrate that this compound eye boasts the ability to scan images from various angles without anomalous blurring or aberrations. Quantitative analysis can be conducted by illuminating with a laser at angles varying from -80° to 80° in 20° increments, in both the x and y directions. This is demonstrated in a consolidated image shown in Fig. 2-5g, demonstrating that the FOV is 160°. Fig. 2-5h&i

illustrate this compound eye can accurately and simultaneously render numerous objects situated at significantly diverse angular orientations and distances.

In order to further improve the FOV, this group endeavoured to mimic the anatomical structure of a fiddler crab's compound eyes [8]. In this work, the author followed the herein-before research principle to precisely align each micro-lens and its corresponding photodetector on curved surfaces and used a black layer to prevent crosstalk. The major progress of this work lies in the expansion of FOV to a range of 160° vertically and 300° horizontally. Furthermore, the graded micro-lens closely mimics the flat corneal lens and the observed graded refractive index (RI) structure in the fiddler crab's eye. As a result, it exhibits few alterations in its focusing power when exposed to changes in the external medium. Consequently, this artificial compound eye is capable of producing clear amphibious images, even when objects are positioned at varying distances in the air.

In contradistinction to the research conducted by Song et al., which primarily concentrated on the static properties of BCACEs, Floreano et al. exhibited a distinct emphasis on their dynamic characteristics [33],[35]. Fig. 2-5j is the image of their prototype whose FOV is $180^{o} \times 60^{o}$ as shown in Fig. 2-5k [33]. This prototype consists of three major layers: an optical layer, a photodetector layer, and a printed circuit board as shown in Fig. 2-5l. Specifically, the optical layer is constituted of an assemblage of exceptionally transparent polymer micro-lenses and two low-reflectivity opaque metal layers, each featuring corresponding pinhole patterns, the former focusing light precisely onto the photodetector layer, while the latter suppressing optical crosstalk. Besides, the photodetector layer aims to record the signal for

subsequent processing, and the printed circuit board aims to collect and transmit the signals emitted from the ommatidia to the processing units.

Since photodetectors are discrete, the direct imaging result of this artificial compound eye is mosaic. Consequently, it is more appropriate to investigate its dynamic characteristics. For example, Fig. 2-5m&n illustrate the capability of this artificial compound eye to detect dynamic optical flow under various motion conditions.

In this section, the research on BCACEs evolves to incorporate a hybrid configuration of micro-lens arrays and photodetector arrays. This facilitates the recording of light information from a curved micro-lens array by replacing the conventional planar photodetector array with a photodetector array within a curved surface. However, there are also several limitations associated with this approach. Firstly, the fabrication and reproduction of the photodetector array within a curved surface are challenging due to the distribution of photodetectors on a curved surface. Secondly, the presence of interspaces between photodetectors hinders the artificial compound eye from fulfilling the requirements of both static imaging and dynamic motion detection. This is due to the need for a scanning procedure to achieve static imaging, which ultimately reduces the imaging rate significantly. Consequently, dynamic motion detection relies on direct imaging, and the mosaic images can not be avoided. Thirdly, while this artificial compound eye design bears a greater resemblance to natural compound eyes compared to previous versions that only incorporate micro-lenses, it still lacks certain components found in natural compound eyes, such as light guides.

2.4.1.3 Research on BCACEs with light guides

Similar to NCEs, BCACEs discussed in this section harness light guides to transmit light information from micro-lenses to photodetectors. The incorporation of light guides eliminates the necessity for arranging photodetectors along a curved surface. This modification leads to a reduction in the design and fabrication complexity of photodetector arrays within curved surfaces and an enhancement in the efficiency of light transmission.

Such particular artificial compound eye designs are rooted in the work of Lee et al. in 2006 [36]. In their study, Lee proposed the use of the disparity in refractive indices between the light guide core and the light guide cladding (or waveguide core and waveguide cladding, as presented in this paper) to mimic the function of the rhabdom found in natural ommatidia, serving as the light guide, as illustrated in Fig. 2-6a. Both the light guide core and cladding in this instance are fabricated from SU-8 material. The distinction lies in the fact that the SU-8 material used for the core undergoes UV exposure, whereas the SU-8 material for the cladding does not. This differential treatment results in a final refractive index difference with a value of 0.029.

While Lee's initial proposal aimed to employ a light guide for transmitting optical information from a curved micro-lens array to a planar surface, he encountered limitations in achieving both static imaging and dynamic motion detection. This challenge stems from his utilization of a photomultiplier, which is essentially a point detector, rather than a photodetector array for capturing light signals.

After this basic research, subsequent investigations in this section can be categorized into two distinct approaches: the utilization of optical fibre light guides and homemade light guides.

For the former, the origins could be retraced to a US patent awarded in 2008 [37]. As illustrated in Fig. 2-6b, a pivotal attribute of this patent involves the utilization of a glass optical fibre bundle to convey light information from the curved lenslet array to the flat detector array. Fig. 2-6c further delineates the fabrication process for such a light guide bundle. Initially, a fused imaging fibre conduit is created by subjecting an aligned bundle of straight glass fibres to heat. Subsequently, this fused conduit is heated once more at its centre and then drawn to create a double-tapered imaging fibre conduit, which is subsequently divided into two segments. The segmented imaging fibre taper is further modified by undergoing a second cut to achieve the desired length. Following this, the larger end is shaped into a dome, and the light guide bundle is finalized after polishing both ends.

However, due to the limited bending resistance of glass optical fibres, the FOV of this BCACE is constrained. Plastic optical fibres, known for their superior flexibility and resistance to bending, prove to be more suitable for achieving a broader FOV. Consequently, in Ma's work on BCACEs [6],[9],[57]-[62], plastic optical fibres were integrated with post-processing algorithms to accomplish imaging [6] and orientation detection [9], respectively. For instance, a single photodetector is employed to replace the photodetector array in capturing light information from all optical fibres, as illustrated in Fig. 2-6d. Subsequently, a single-pixel imaging technique is utilized to reconstruct the image [6]. Additionally, an image sensor is employed to record light information

from optical fibres, as depicted in Fig. 2-6e, followed by the utilization of a neural network to detect the target's orientation [9]. Similarly, Krishnasamy employed fibre bundles to assemble a compound eye for object tracking [38].

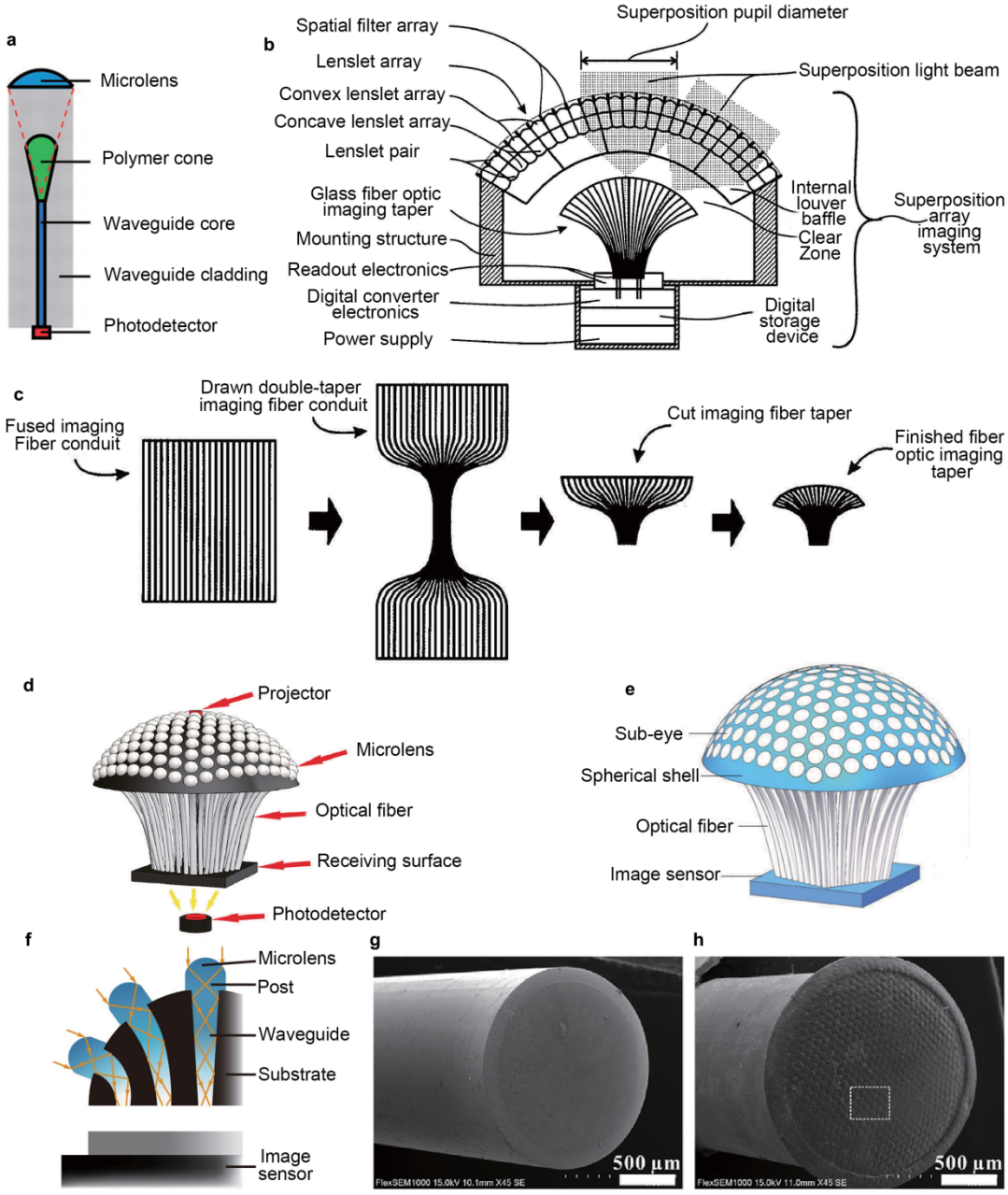

Figure 2-6. BCACEs with light guides. a, Artificial ommatidium proposed by Lee's group [36]. **b,** Schematic cross-sectional view of an array imaging system. **c,** Schematic flow diagram showing the process steps to fabricate a light guide bundle [37]. **d,** Schematic diagram of a single-pixel BCACE [6]. **e,** Schematic diagram of a BCACE mimicking bee's eyes [9]. **f,** Labelled cross-section of a

BCACE with home-made light guides [39]. **g&h,** Integration of a micro-lens array and a plastic optical fibre used for illumination [40]. **g,** Polished original planar plastic optical fibre end face. **h,** Fabricated plastic optical fibre end face.

While it shows promise to employ plastic optical fibres as light guides to replicate natural compound eyes, several limitations still exist. Firstly, the overall size is prohibitively large due to the dimensions of the plastic optical fibres used. Secondly, FOV remains insufficient and can be enhanced through modifications to the 3D structure. Thirdly, direct imaging of the current design proves challenging due to the discrete distribution of plastic optical fibres and the wide acceptance angle of each fibre. Fourthly, both imaging and dynamic detection require post-processing, necessitating either sequential pattern projection on the BCACE (single-pixel imaging [63]) or extensive prior knowledge (neural network [64]). These factors impede practical applications.

Another concept involves the utilization of homemade light guides. Dai et al. suggested employing silicone as the light guide core (with a refractive index of 1.50, as depicted in Fig. 2-6f), along with UV-curable diacrylate polymer serving as the light guide cladding (with a refractive index of 1.46, constituting the substrate in Fig. 2-6f) [39]. By adopting this approach, light can be efficiently transmitted from a curved surface to a planar image sensor. Nevertheless, it is important to note that this method faces limitations in terms of fabrication and still exhibits a constrained FOV.

The integration of a curved micro-lens array, light guides, and photodetectors closely mimics the anatomical structure of natural compound eyes, effectively circumventing the challenges associated with fabricating

photodetector arrays within curved surfaces. Consequently, this approach holds the most promise for further enhancing the performance of BCACEs. However, these BCACEs still exhibit certain limitations. For instance, FOV is constrained, and it is challenging to simultaneously fulfil static imaging and dynamic motion detection within a single BCACE. Additionally, the acceptance angle of an individual ommatidium remains relatively large.

One additional point worth mentioning is that a micro-lens array integration with light guides can serve not only for imaging and dynamic motion detection but also for illumination when the light propagation direction is reversed, i.e., from the light guide to micro-lenses. For instance, Liu et al. previously suggested the incorporation of a micro-lens array at the distal end of a plastic optical fibre [40], as depicted in Fig. 2-6g&h. When light is introduced from the far opposite end of the plastic optical fibre, the micro-lens array improves the evenness of light emission over a broad field of view.

2.4.2 BCACEs with tunable focal lengths

The direct approach for modifying the focal length of compound eyes involves the manipulation of the micro-lenses distributed along the surface of the macro-base. In certain studies, the alteration of micro-lenses alone is employed to adjust focal lengths, while in others, modifications are made not only to the micro-lenses but also to the macro-base itself, thereby enabling adjustments to the FOV. Specifically, BCACEs of this nature are categorized based on the methods employed for tunability.

2.4.2.1 Fluidic pressure

Among various methods to tune shapes, fluidic pressure is the simplest method. Wei et al. incorporated the structural benefits pertaining to insect apposition NCEs and human eyes to form an adaptive BCACE as shown in Fig. 2-7a [42]. A big, transparent polymeric membrane, capable of transitioning from a flat surface into a spherical cap with diverse radii of curvature, is utilized to replicate the dome-shaped structure found in insect NCEs. A grid (3x3) of lenses, comprised of petite transparent polymeric membranes with fluidic structures beneath, is situated atop the big membrane. The focusing power of the lenses can be modified by changing the volume of the fluid, enabling the achievement of an accommodation function. A microfluidic channel network consisting of two layers facilitates fluid delivery, allowing for distinct deformation of both the big membrane and the small membranes of individual lenses.

Similarly, Cheng et al. also proposed a BCACE using liquid lenses to minimize defocus aberration [41]. The defocus aberration here refers to the situation where the focal points of microlenses distributed on the curved plane are not aligned on a single common plane, leading to blurred or unclear images. Fig. 2-7b depicts the model, encompassing the object plane, the compound eye, the aperture array, and the image plane. Each individual micro-lens within the compound eye is saturated with a kind of liquid optical medium, enclosed in a microcavity sealed by a polydimethylsiloxane (PDMS) membrane. Within the same ring, an annular liquid microchannel is incorporated into the sidewall of the cavity to facilitate the injection of liquid, thereby connecting the micro-lenses. As the liquid is introduced or removed from the liquid microchannel through a syringe pump, the PDMS membrane undergoes deformation, leading to an alteration of the focal length. In various rings, the liquid lenses exhibit distinct

optical characteristics, whereas those within the same ring share identical parameters. Likewise, the aperture array serves to prevent optical signal interference.

2.4.2.2 Thermal effect

The thermal effect provides another way to change the focal lengths of BCACEs. Wang et al. proposed a kind of graphene-based BCACE as shown in Fig. 2-7c [43]. All micro-lenses are fabricated with graphene nanosheets (GNSs) which can absorb energy and convert it to thermal energy when driven by near-infrared (nIR) pulsed laser irradiation based on Maxwell's electromagnetic wave theory [65],[66], resulting in the increment of the temperature of micro-lenses. Correspondingly, the pressure differential at the air-solution interface, which directly dictates the configuration of the liquid meniscus, will be tuned with the increment of the temperature based on Adamson's theoretical model [67],[68]. Hence, when near-infrared (nIR) irradiation is activated, the photothermal conversion initiated by GNSs prompts the liquid in the micro-lenses to escape from the microcavity. Conversely, when the nIR laser is deactivated, the resulting cooling leads to the liquid within the micro-lenses retracting back into the microcavity, i.e. shapes of micro-lenses are tuned with changes of the nIR laser conditions. In this way, every micro-lens on the surface of the macro-base is tuned precisely.

Similarly, Zhu et al. utilized a thermoresponsive and reversible hydrogel ring made of N-isopropyl acrylamide (NIPAAm) as a microactuator for fine-tuning the focal length [44]. With a decrease in temperature from above to below the lower critical solution temperature (LCST) of the hydrogel, the hydrogel absorbs water and undergoes swelling. As the volume alteration induced by

water in the cavity is less pronounced than in the hydrogel ring, it results in a net volume change that governs the curvature of the water-oil meniscus as shown in Fig. 2-7d&e. Therefore, the focal lengths of these liquid micro-lenses can be adjusted by altering the environmental temperature. To validate this principle, in that paper, an array consisting of three micro-lenses, denoted by smaller dashed-line circles in Fig. 2-7f, is positioned onto a hemispherical glass dome. A small resistor is positioned adjacent to each micro-lens to regulate the local temperature. Fig. 2-7g illustrates the lateral view of the water menisci at various temperatures. The upper image was captured at 23°C, whereas the lower one was taken at 55°C, revealing a significant alteration in the curvature radius of the water-air meniscus.

2.4.2.3 pH

Inspired by the adaptable crystalline lens, which is aided by the ciliary muscles of the human eye, BCACEs here are fabricated with bovine serum album (BSA) protein [45]. Fig. 2-7h illustrates the pH-induced actuation mechanism, which is ascribed to the existence of carboxyl groups and amino groups linked at the isoelectric point within the BSA molecular chains. These groups can undergo deprotonation or protonation based on varying pH levels [69]-[72]. The electrostatic interaction among these groups induces the expansion or contraction of BSA structures, resulting in alterations in the focal length. Similarly, in order to verify the principle, based on whether the FOV can be altered, two types of BCACEs are proposed: entire protein-based BCACE and composite BCACE. The former is fabricated with BSA entirely, so with variations in the pH of the surrounding environment, the macro-base and micro-lenses are concurrently adjusted, resulting in an adaptable FOV and focal length (Fig. 2-7i). The latter

comprises a macro-base made with chemically inert SU-8 and micro-lenses made with BSA, resulting in the focal length being solely tuned at a fixed FOV (Fig. 2-7j).

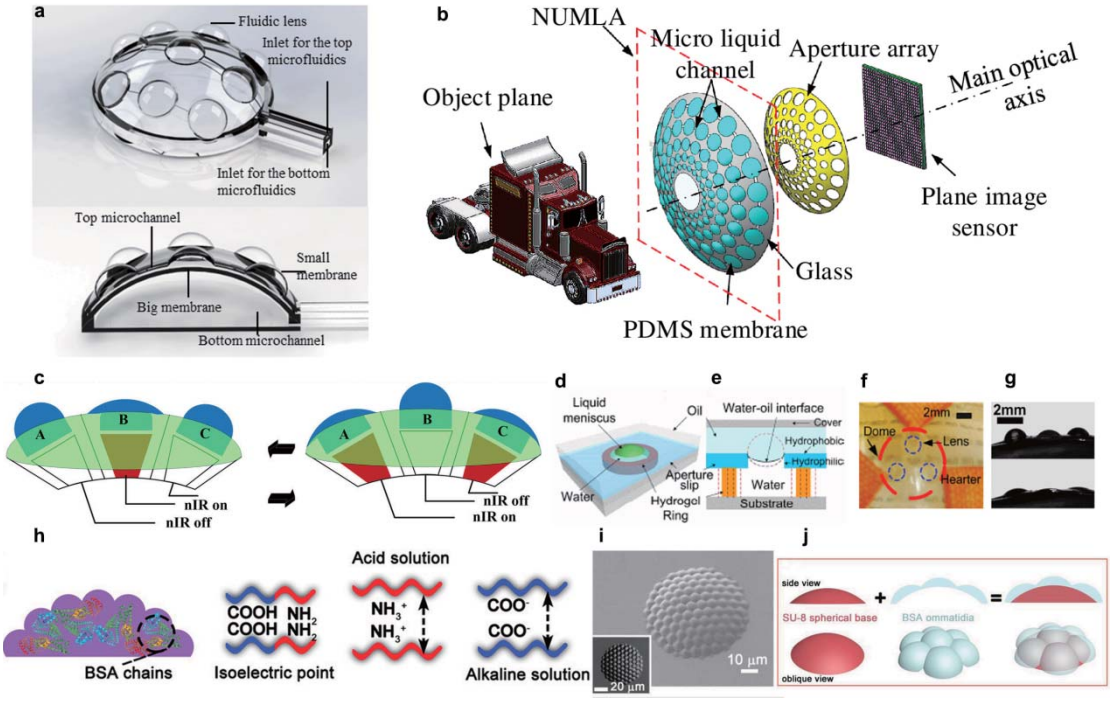

Figure 2-7. BCACEs with tunable focal lengths. a, Working principle of the BCACE which distributes an array of membrane-encased fluidic lenses on a big flexible membrane [42]. **b,** Schematic diagram of the BCACE with self-adaptive focal length adjustment to minimize defocus aberration [41]. **c,** Adaptation of the microscopic lens shapes under nIR irradiation [43]. **d&e,** Structure and mechanism of an adaptable-focus micro-lens controlled by a thermoresponsive hydrogel ring. **d,** 3-D diagram of a single micro-lens. **e,** Cross-section of a single micro-lens [44]. **f,** Photo of a micro-lens array with three micro-lenses on a glass hemisphere. **g,** Lateral view of the water droplets at two different temperatures (Top: 23°C; bottom 55°C) [44]. **h,** Fundamental mechanism of protein-based BCACEs with adjustable features [45]. **i&j,** Protein-based BCACEs. **i,** SEM image of the entire protein-based BCACE, and the inset is an optical microscopy

image. **j,** Illustrative representation of the composite BCACE comprising a passive SU-8 hemispherical macro-base and active BSA-based micro-lenses [45].

In this section, we have analyzed three methods employed to modify the focal lengths of BCACEs. It is worth noting that in addition to these three mentioned methods employed in BCACEs, there are numerous other techniques available for adjusting the focal lengths of micro-lenses, which have not yet been utilized in BCACEs. The integration of these methods with BCACEs holds the potential for significant advancements, which will be further elaborated upon in the subsequent discussion section. Furthermore, it feasible to develop an artificial compound eye with a complete anatomical structure, including light guides, that also features adjustable focal lengths. The author's ongoing efforts involve combining microlenses adjustable via microfluidic techniques with imaging optical fibre bundles that serve as light guides. This integration could enable artificial compound eyes to achieve adjustable focal lengths while maintaining a complete anatomical structure.

2.5 Fabrication methods

2.5.1 Fabrication of curved micro-lens arrays used in BCACEs

The common approach for producing a curved micro-lens array involves a combination of lithography, thermal embossing, and gas-assisted deformation. For example, Lian et al. combined these methods to form a BCACE as shown in Fig. 2-8a-j [32]. Firstly, the photoresist is spin-coated on a silicon substrate and a conventional lithography procedure is employed to transfer the mask patterns

onto the photoresist (Fig. 2-8a). After that, the plasma etching process is used to transfer the patterns onto the silicon wafer (Fig. 2-8b-c). Next, a passivation layer is developed on the mould's surface to ease the demoulding process. (Fig. 2-8d). Furthermore, a polymer (cycloolefin copolymer, 500 μm thickness) is pressed under a pressure of 200 mbar at 145℃ for 6min (thermal embossing, Fig. 2-8e). After purging with nitrogen gas for 10 minutes and cooling to 80°C, it is possible to detach the polymeric micro-lenses with different focal lengths (Fig. 2-8f). What's more, soft lithography (Fig. 2-8g) and gas-assisted deformation (Fig. 2-8h) are employed for pattern transfer and the conversion from a planar to a curved structure. Subsequently, a photosensitive resin is poured onto the deformed membrane and solidified by exposure to ultraviolet (UV) light (Fig. 2-8i). Finally, the BCACE with multifocal micro-lenses is obtained successfully (Fig. 2-8j). Besides, the curved micro-lens array can also be manufactured using a combination of lithography and a two-step thermal reflow process [73].

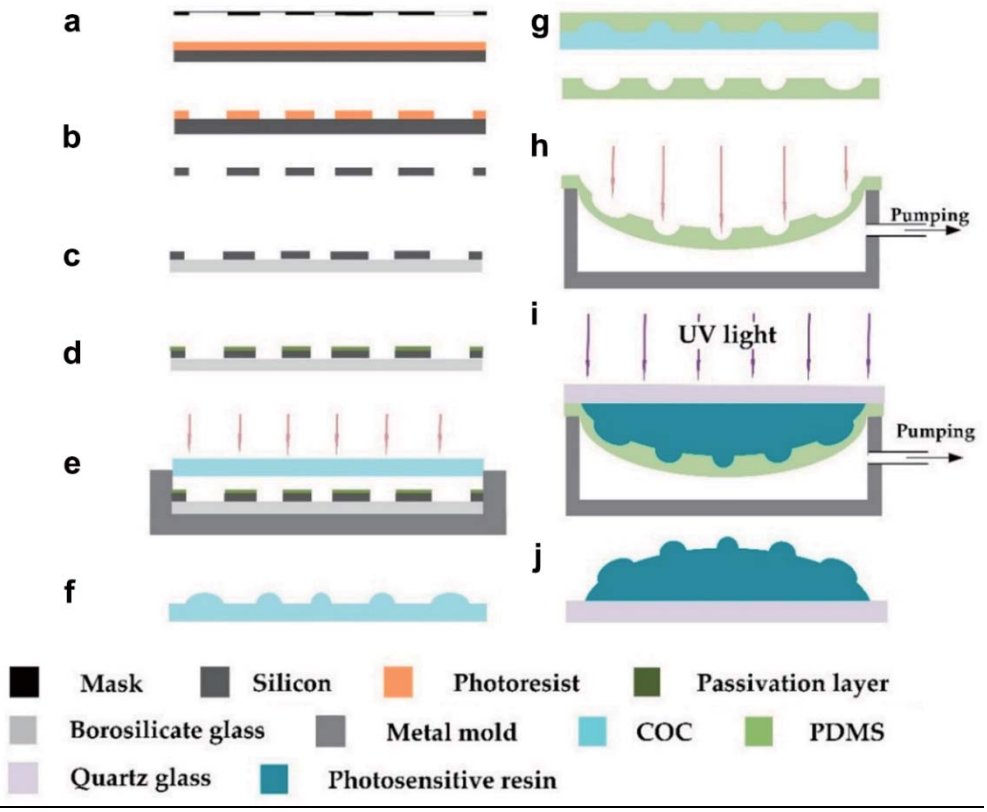

Figure 2-8. Schematic diagram of the fabrication process combining lithography, thermal embossing, and gas-assisted deformation [32]. a, Photoresist spin-coated on a silicon substrate and exposed. **b,** Development and etching of silicon wafers. **c,** Bonding of patterned silicon substrate to borosilicate glass. **d,** Growth of a passivation layer on the surface. **e,** Heating and pressing of the polymer. **f,** Polymer peeled off to get a micro-lens array pattern. **g,** Replication of the structure on the polymer using PDMS. **h,** Deformation of the PDMS membrane and packaging in a sealed cavity under a pressure difference. **i,** Pouring and curing of a photosensitive adhesive. **j,** BCACE peeled off.

Li et al. also proposed the integration of inkjet printing and air-assisted deformation to form a BCACE [74]. Fig. 2-9a-c demonstrate the inkjet printing procedure for the micro-lens array. Firstly, the micro-lens morphology is governed by precisely controlling the quantity of droplets deposited in the identical location with a high degree of accuracy. Subsequently, the device is annealed for 15 minutes at 90°C, exposed to UV treatment until full cross-linking is achieved, and then subjected to an additional 30-minute annealing at 100°C. As a result, a planar micro-lens array is obtained. Fig. 2-9d-f demonstrate the air-assisted deformation process. In the first step, PDMS is used for the pattern transfer process. Subsequently, the negative air pressure is employed to create a deformed elastomer membrane. After achieving pressure stability, solvent-free UV-curable epoxy resin is introduced into the created cavity, covered with a coverslip, and then exposed to UV light for a complete cross-linking process lasting 5 minutes. Finally, after peeling, the compound eye is produced.

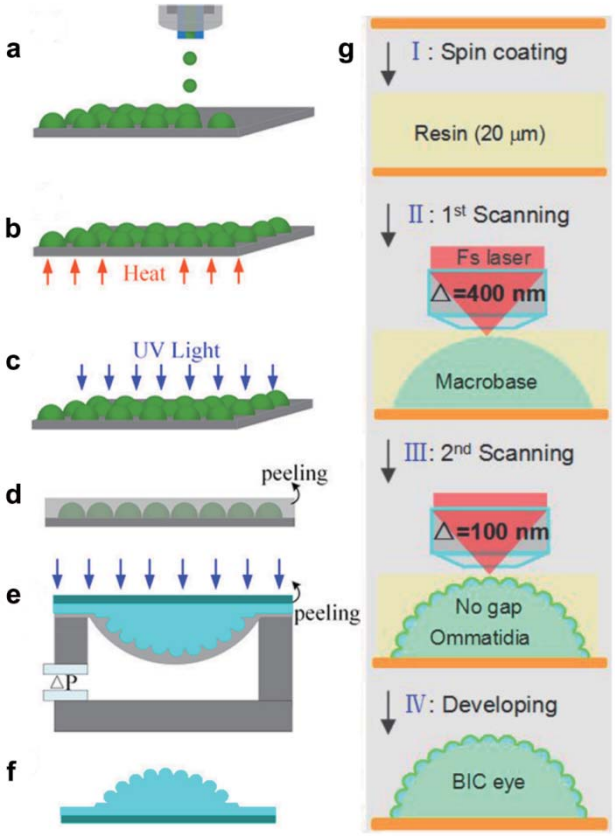

Figure 2-9. Schematic diagram of the fabrication process combining inkjet printing and air-assisted deformation [74], and fabrication process including the laser direct writing method [30]. a−c, Fabrication of the micro-lens array. **a,** A micro-lens array fabricated through inkjet printing, where the geometry and dimensions of the micro-lens are regulated by the number of superimposed drops. **b, c,** Heating and UV irradiation. **d,** PDMS moulding. **e,** Membrane deformation. **f,** Formation of the BCACE. **g,** Schematic for the fabrication of a BCACE by the laser direct writing method [30].

Similarly, Wang et al. proposed the creation of a BCACE based on GNSs using air-assisted deformation, as illustrated in Fig. 2-10 [43]. Following the formation of a transparent hemispheric dome through the mentioned air-assisted

deformation, numerous microcavities are retained within this dome (Fig. 2-10a-c). Subsequently, the dome is immersed in a vacuum beaker filled with glycerol/graphene nanosheets solution before being withdrawn (Fig. 2-10d-e). Ultimately, the droplet is adsorbed into the microcavity, facilitated by the capillary breakup, serving the purpose of a GNS-based microlens (Fig. 2-10f).

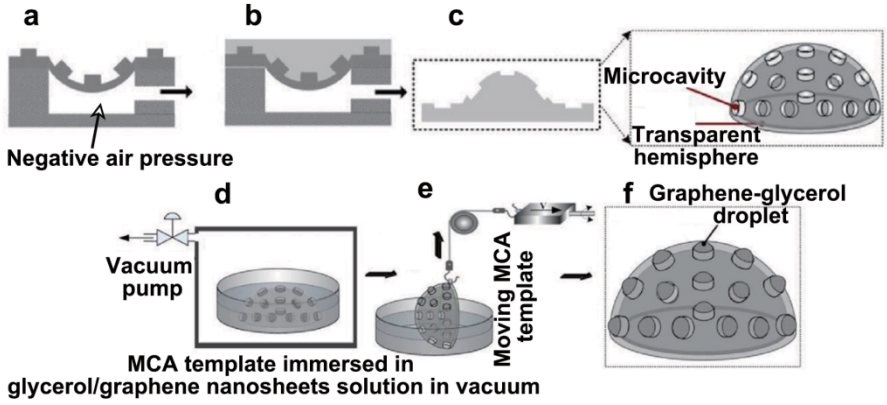

Figure 2-10. Fabrication of BCACE based on graphene nanosheets (GNSs) [43]. a, PDMS elastomer membrane shaped into a hemispheric dome under negative air pressure. **b,** UV-curable epoxy resin dispensed on deformed elastomer, fully cross-linked. **c,** Microcavity array (MCA) template resulted from manually peeling off the NOA (Norland optical adhesive) hemispheric shell. **d,** MCA template vacuum-immersed in glycerol/graphene nanosheets solution to fill each microcavity. **e,** Beaker with glycerol/graphene nanosheets solution, where the MCA template moves at 0.16 mm/s and the temperature is maintained at 15ºC. **f,** BCACE with GNSs serving as microlenses.

Recently, the femtosecond laser direct writing technology has become a promising method because of its effective ability to realise various 3D complex microstructures and high precision [30],[31],[45],[75]-[77]. For example, the femtosecond laser direct writing technology is employed to obtain micro-lenses

with sizes as small as microns [30], as shown in Fig. 2-9g. After spin-coating the resin, the macro-base and micro-lenses are fabricated, respectively, by forming voxels with different dimensions, thus producing the curved micro-lens array used in BCACEs.

The aforementioned fabrication methods can be broadly classified into two types. The first involves the initial formation of a two-dimensional lens array, followed by deformation into a three-dimensional lens array through fluid-assisted techniques. The second type employs laser direct writing technology to directly generate a three-dimensional lens array. The first type, upon the creation of a three-dimensional lens array template, facilitates batch production; however, due to constraints in the processing methods of two-dimensional lens arrays, lenses in this category tend to exhibit a relatively undiversified nature. Correspondingly, the second type of solution possesses a higher degree of processing freedom, allowing for the fabrication of lenses with diverse shapes, while sacrificing some fabrication time and cost.

2.5.2 Integration of BCACEs

This integration can be categorized into two distinct types: (1) the integration of a curved micro-lens array and a photodetector array a within curved surface, and (2) the integration of a curved micro-lens array, optical light guides, and a planar photodetector array.

Regarding the first type, an initial step involves the integration of a planar micro-lens array with a planar photodetector array, ensuring precise alignment between each micro-lens and its corresponding photodetector. Subsequently, this

combined structure is flexed or curved to conform to a predetermined curved surface design.

As for the second type, when optical fibres serve as light guides, a pre-perforated three-dimensional structure is typically fabricated at the outset. Following this, optical fibres are threaded through preformed apertures. In cases where homemade light guides are employed, an initial step involves the fabrication of a host structure (for instance, through methods such as projection micro stereolithography 3D printing). Subsequently, a liquid light guide is introduced into pre-established channels, utilizing techniques such as microfluidic-assisted moulding. The liquid light guide is then solidified through a curing process, resulting in the formation of an elastomeric connection. These processes effectively establish the connection of the light guides to other system components.

2.6 Applications

Although the planar micro-lens array has been applied widely, for example, in the endoscopic system [78]-[80], intraoral diagnosis [81]-[83], and photolithography [84], when it comes to the application of BCACEs, it primarily focuses on the detection of motion. Noteworthily, the detection of motion focuses on recognizing motion behaviours through consecutive frames of a scene that encompasses various techniques such as capturing optical flow fields, while the conventional capture of video-rate images emphasizes the process of recording a rapid succession of frames to produce a video. Importantly, BCACEs possess unique merits in the detection of motion. For example, its wide FOV

helps BCACEs to excel in motion detection under a wide field compared with common cameras, and thus BCACEs are more fitting for being applied in areas such as obstacle avoidance. In the future, if BCACEs mimicking superposition NCEs make huge progress, they will also be more effective in detecting motion under dim light conditions compared with common cameras.

Specifically, Leitel et al. qualitatively measured the optics flow fields for yaw and pitch rotation with the BCACE mentioned before [33], as shown in Fig. 2-11a [85], where the optical flow vectors' direction represented motion direction and length represented motion velocity. Similarly, Yoo et al. proposed to combine the BCACE and the convolutional neural network to achieve the ego-motion (the movement of the camera itself, rather than the transition between two scenes) classification [86].

Ulteriorly, in order to test the linear motion and circular motion quantitively, Pang et al. proposed a seven-micro-lenses BCACE, as shown in Fig. 2-11b [87]. The experimental setup is arranged as depicted in Fig. 2-11c. Throughout the experiment, the LED target underwent a circular motion within the *x*-*y* plane, while the translation stage executed linear motion at a rate of 10 mm/s in the *z*-direction, spanning a range from 100 to 200 mm. Fig. 2-11d illustrates an exquisite match between the reconstructed *z* value and the true *z* value, where the diagonal line of Fig. 2-11d represents the true *z* value since the translation stage moves at a constant speed between 100 and 200 mm. Correspondingly, Fig. 2-11e shows that the reconstructed *x* and *y* coordinates follow a circle relationship whose diameter closely matches the true diameter of the circular motion. Therefore, the possibility of using BCACEs in motion detection is quantitively researched.

Although, in some essays, so-called BCACEs were proposed [88]-[90], these systems, which disperse several cameras on curved structures, possessing large volumes and high weights, in reality, are not compact BCACEs. For instance, Floreano et al. proposed a vision system that was employed by unmanned aerial vehicles to evade obstacles, as shown in Fig. 2-11f [88],[89]. Similarly, for the purpose of extracting self-motion parameters of ground-moving robots from optical flow to surprisingly high precision, a prototype of a sensor head featuring eight sensors, each oriented at angular intervals of 45° from one another in azimuth, and looking downward to the ground at an angle of -45° below the horizon, is illustrated in Fig. 2-11g [90].

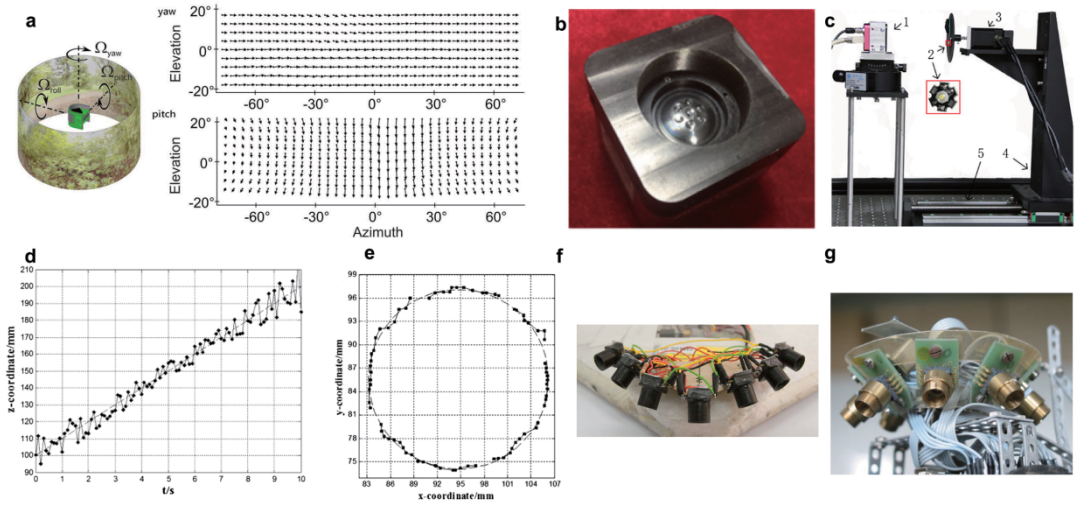

Figure 2-11. Applications of BCACEs. a, BCACE placed inside a circular arena lined with a natural pattern. It captures optical flow fields, which are depicted in a Mercator projection, showcasing yaw and pitch rotations at 22°/s [33]. **b-e,** BCACE used to test linear and circular motion [87]. **b,** Seven-micro-lens BCACE. **c,** Experimental setup. (1) Bionic compound eye system. (2) LED target. (3) Speed motor. (4) Translation stage. (5) Horizontal guide rail. **d,** Reconstructed *z*-values from 100 to 200 mm. **e,** Reconstructed *x*-*y* locations at 150 mm. **f,** Close-up view of a BCACE consisting of seven optic flow sensors

employed by unmanned aerial vehicles. The viewing directions are oriented towards each side and below the aircraft, with an eccentricity angle of 45° and azimuthal angles of 90°, 120°, 150°, 180°, 210°, 240°, and 270°, respectively [89]. **g,** BCACE containing eight optical mouse sensors, each looking at a 45° angle relative to each other in azimuth and inclined approximately -45° in relation to the horizon, towards the ground [90].

While BCACEs have made significant progress in motion detection, they still have a considerable journey ahead to meet requirements beyond laboratories. These challenges encompass small-scale, high-rate, and complex motions, among other factors, all of which are indispensable for practical applications. Moreover, other applications (such as real-time panoramic imaging with high resolution) demand higher performance from BCACEs. Consequently, there is still a considerable path to be traversed before BCACEs can find broader applications.

2.7 Summary

This chapter has provided a comprehensive review of biomimetic curved artificial compound eyes (BCACEs). Rooted in the foundational underpinnings of natural compound eyes (NCEs) and BCACEs, we have introduced a set of parameters to delineate the characteristics of BCACEs. The reviewed BCACEs are categorized into two primary types based on their working principles: those with fixed focal lengths and those with tunable focal lengths. In particular, the former type can be further subdivided into three categories, namely, simplified BCACEs, BCACEs with photodetector arrays within curved surfaces, and

BCACEs with light guides. The latter type can also be categorized based on various techniques for altering the shapes of micro-lenses, including fluidic pressure, thermal effects, and pH adjustments.

Concerning fabrication, while some innovative methods such as laser direct writing have been proposed for creating curved micro-lens arrays used in BCACEs, the production of a complete BCACE system that can rival the performance of sophisticated NCEs remains an exceedingly challenging task. Consequently, BCACEs still have a considerable journey ahead. For instance, novel design concepts and fabrication approaches need to be developed to emulate not only apposition NCEs but also optic superposition NCEs and neural superposition NCEs. Detailedly, research on apposition ACEs primarily focuses on mimicking the anatomical structures located on the outer regions of the brain (Chapter 4 of this thesis for an example). Similarly, studies on optic superposition ACEs have concentrated on mimicking the external structures related to optical performance, with limited exploration of the inner neural structures (chapter 5 of this thesis for an example). In contrast, mimicking neuron superposition NCEs requires detailed replication of complex inner neural structures situated near the brain's centre, significantly increasing the level of difficulty. This complexity likely explains the limited attention given to the mimicry of neuron superposition NCEs.

In summary, it is foreseeable that BCACEs will transform micro-optical imaging systems into versatile platforms, and from mimicking apposition NCEs to superposition NCEs, for practical applications, including but not limited to smart healthcare [91], intelligent robotic vision systems [92], and unmanned aerial vehicle vision systems [93].

Chapter 3 Design and fabrication of a novel artificial ommatidium

This work is reproduced in part from H. Jiang *et al*., "Optical Fibre based Artificial Compound Eyes for Direct Static Imaging and Ultrafast Motion Detection," *Light: Science & Applications*, in press.

The research project of this chapter focuses on primarily theoretical analysis and fabrication of a novel artificial ommatidium, which is the basic imaging unit of ACEs. Conical microlensed plastic optical fibres faithfully mimic the anatomic structure of natural ommatidium to work as the artificial ommatidium. Specifically, Optical fibres function as light guides in ACEs to transmit the light from the curved light detection surface to a flat imaging sensor chip. Therefore, in order to reduce the overlap of the receiving areas of adjacent fibres, the acceptance angle of each fibre should be low to increase the angular resolution (Fig. 3-1). Here, the acceptance angle of a bare plastic optical fibre (Fig. 3-1a), and a plastic optical fibre with a microlens (Fig. 3-1b) is theoretically analyzed. Further, a new method to fabricate conical microlensed plastic optical fibres is proposed.

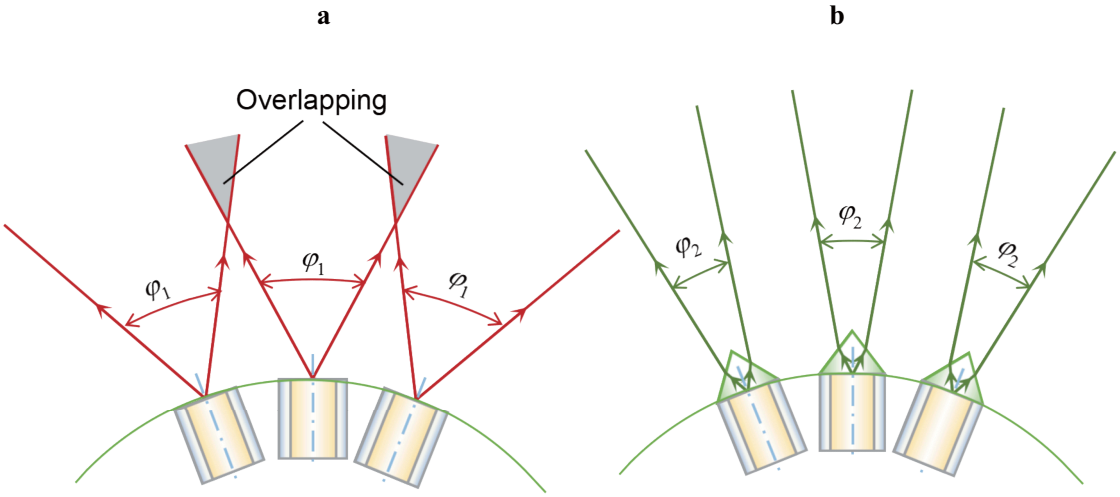

Figure 3-1. Overlapping acceptance angles between adjacent optical fibres (i.e., ommatidia). a, Bare optical fibres have flat ends and a large acceptance angle (φ_1), which causes severe overlap. **b,** With conical microlenses, the acceptance angle (φ_2) can be narrowed to reduce this overlap.

3.1 Brief description of optical fibres

Optical fibres play a crucial role in many fields due to their unique working principle. The difference in refractive index between the optical fibre core and cladding causes light to undergo total internal reflection at the core-cladding interface when it hits at certain angles, enabling efficient light transmission. Since the invention of low-loss optical fibres [94], they have found a wide range of applications, including telecommunications [95], sensors [96], light guides [40], and imaging systems [97].

Optical fibres can be categorized into two main types based on materials: silica optical fibre and plastic optical fibre. Silica optical fibres utilize SiO_2 with varying refractive indices for the core and cladding, resulting in very low loss. However, due to the rigidity of SiO_2, silica optical fibres have limited flexibility

and can only bend at low angles. On the other hand, plastic optical fibres are composed of polymers such as polymethyl methacrylate (PMMA) and poly tetra fluoroethylene (PTFE). Although plastic optical fibres have higher loss compared to silica fibres due to their materials, they offer superior flexibility. In the context of ACEs, where optical fibres need to bend at high angles over short distances for light transmission, plastic optical fibres are more suitable.

The majority of plastic optical fibres are characterized by a large core diameter, which precipitates dispersion during the transmission of light through these fibres [98]. Consequently, images of objects transmitted through plastic optical fibres manifest as speckle patterns. Although several methodologies, including the transmission matrix approach [99] and artificial intelligence algorithms [100], have been explored to revert these speckle patterns to their original form, the practical application of these techniques remains elusive due to their complexity and the extensive prerequisite knowledge required. In this chapter, we propose an alternative strategy that utilizes the light emitted from each plastic optical fibre as an individual imaging pixel, thereby obviating the need to reconstruct speckle patterns. To enhance angular resolution, it is imperative that the acceptance angle of each plastic optical fibre is low. Thus, the focus of this chapter is on the design and fabrication of microlensed plastic optical fibres with reduced acceptance angles to function as aritificial ommatidia.

3.2 Analysis of plastic optical fibres

3.2.1 Acceptance angle of the bare plastic optical fibre

A plastic optical fibre usually has a core (PMMA) and a cladding (PTFE). Based

on the principle of optical path reversibility, the acceptance angle of the optical fibre is equal to the divergence angle when the light exits the fibre end. Therefore, we can study the divergence angles of optical fibres in different scenarios (Fig. 3-2).

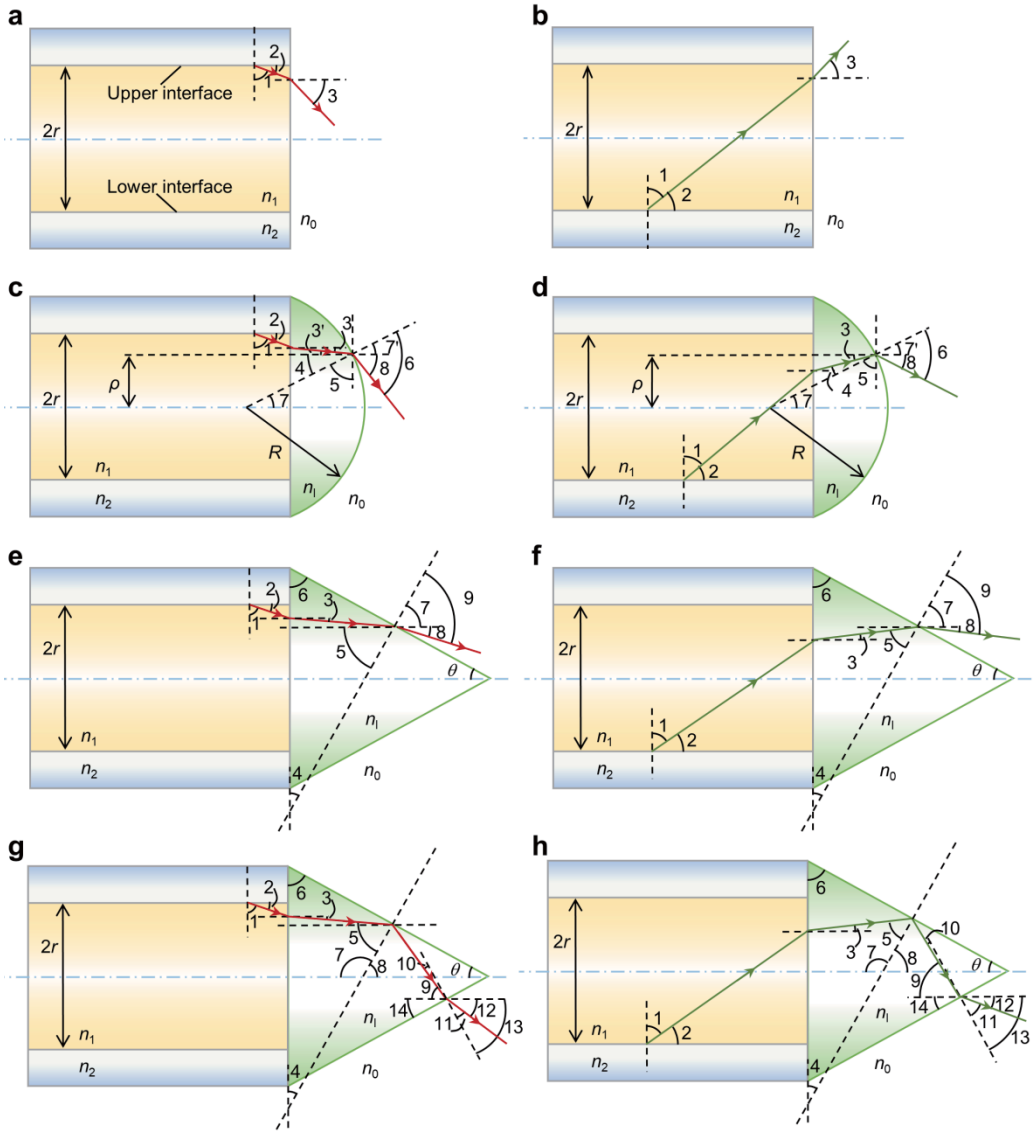

Figure 3-2. Light paths in different optical fibres for the analysis of the divergence angles (or equivalently, the acceptance angles). Red paths represent the light reflected from the upper core/cladding interface of the optical fibre, and green paths represent the light reflected from the lower core/cladding interface of the optical fibre. **a–b,** In the bare multimode optical fibre, the light can be reflected from the upper (**a**) or lower (**b**) core/cladding interface. **c–d,** In

the optical fibre capped with a spherical microlens, the light can be reflected from the upper (**c**) or lower (**d**) core/cladding interface. **e–h,** In the optical fibre capped with a conical microlens, the light has various paths. In one case, the light experiences no reflection in the conical surface after being reflected from the upper (**e**) or lower (**f**) core/cladding interface. In the other case, the light experiences one hop (i.e., reflection) in the conical surface after being reflected from the upper (**g**) or lower (**h**) core/cladding interface.

In the simplest case of a bare multimode optical fibre, the light is reflected from the interface of the core and the cladding (Fig. 3-2). Let n_0, n_1, and n_2 represent the refractive index of the air, core and cladding, respectively, and r denotes the core radius.

Specifically, when $\angle 1$ reaches its minimum (Fig. 3-2a&b), it follows that

$$n_1 \sin \angle 1 = n_2 \sin \frac{\pi}{2}. \tag{3-1}$$

Similarly, when $\angle 2$ reaches its maximum, it follows that

$$\sin \angle 2 = \cos \angle 1 = \cos\left(\sin^{-1} \frac{n_2}{n_1} \right) = \frac{\sqrt{n_1^2 - n_2^2}}{n_1}. \tag{3-2}$$

Based on the law of refraction, at this time, the divergence angle $\angle 3$ reaches its maximum absolute value when

$$\sin \angle 3 = \frac{n_1}{n_0} \sin \angle 2 = \frac{n_1}{n_0} \frac{\sqrt{n_1^2 - n_2^2}}{n_1} = \frac{\sqrt{n_1^2 - n_2^2}}{n_0}. \tag{3-3}$$

Here, $n_0 \sin \angle 3$ is also called the numerical aperture (NA). Typically, a plastic optical fibre has an n_0 value of 1, with $\sqrt{n_1^2 - n_2^2} = 0.5$, and thus, $\angle 3 = 30^{\circ}$.

Similarly, when light is reflected from the opposite side of the interface

between the core and cladding (Fig. 3-2b), the maximum absolute value of $\angle 3$ is 30°. Therefore, the acceptance angle φ_{flat} of the flat end of the plastic optical fibre is $\varphi_{flat} = 60°$.

3.2.2 Acceptance angle of the plastic optical fibre with a spherical microlens

Here, we analyze the acceptance angle of the plastic optical fibre with a spherical or conical microlens (Section 3.2.3) based on light paths. When the light is reflected from the upper core/cladding interface (Fig. 3-2c), it is first refracted at the fibre/microlens interface and then at the microlens/air interface. Let ρ, R and n_l represent the radial position at the microlens surface, the radius of the microlens surface and the refractive index of the microlens, respectively. Then, $\angle 3$ and $\angle 5$ can be calculated as follows:

$$\angle 3 = \sin^{-1}\frac{\sqrt{n_1^2 - n_2^2}}{n_l}. \tag{3-4a}$$

$$\angle 5 = \cos^{-1}\frac{\rho}{R}. \tag{3-4b}$$

Since $\angle 5$ and $\angle 4$ are complementary, we have

$$\angle 4 = \frac{\pi}{2} - \angle 5 = \frac{\pi}{2} - \cos^{-1}\frac{\rho}{R}. \tag{3-5}$$

Then,

$$\angle 3' + \angle 4 = \angle 3 + \angle 4 = \frac{\pi}{2} + \sin^{-1}\frac{\sqrt{n_1^2 - n_2^2}}{n_l} - \cos^{-1}\frac{\rho}{R}. \tag{3-6}$$

Based on the law of refraction, we have

$$\sin(\angle 7' + \angle 8) = n_l \sin(\angle 3' + \angle 4) = n_l \cos\left(\sin^{-1}\frac{\sqrt{n_1^2 - n_2^2}}{n_l} - \cos^{-1}\frac{\rho}{R}\right). \tag{3-7}$$

$$\angle 7' = \angle 7 = \sin^{-1}\frac{\rho}{R}. \tag{3-8}$$

Finally, we have that

$$\angle 8 = \sin^{-1}\left[n_l \cos\left(\sin^{-1}\frac{\sqrt{n_1^2 - n_2^2}}{n_l} - \cos^{-1}\frac{\rho}{R} \right) \right] - \sin^{-1}\frac{\rho}{R}. \tag{3-9}$$

In addition, the angle of the tangent line (Fig. 3-3) at the curved surface is defined as follows:

$$\text{Angle of tangent line} = \cos^{-1}\left(\frac{\rho}{R}\right). \tag{3-10}$$

Thus, the ***upper*** limit angle α_{upper} should be the smaller value between $\angle 8$ and the angle of the tangent line. The analytic results are plotted in Fig. 3-4a for microlenses with different radii.

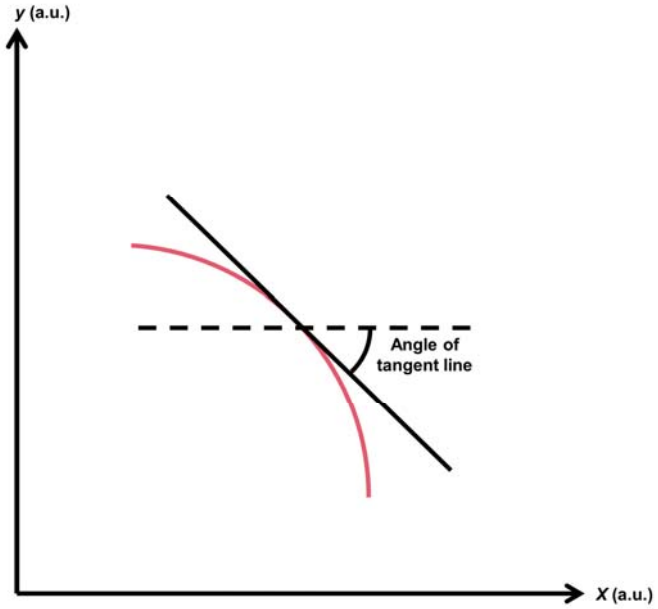

Figure 3-3. Schematic diagram of the angle of the tangent line. The Cartesian coordinate system, featuring the *x*-*y* axis, defines the 2D plane. The black solid line is the tangent line of the curved surface (red line) of a microlens. The angle of the tangent line is determined with respect to the horizontal line (dotted line).

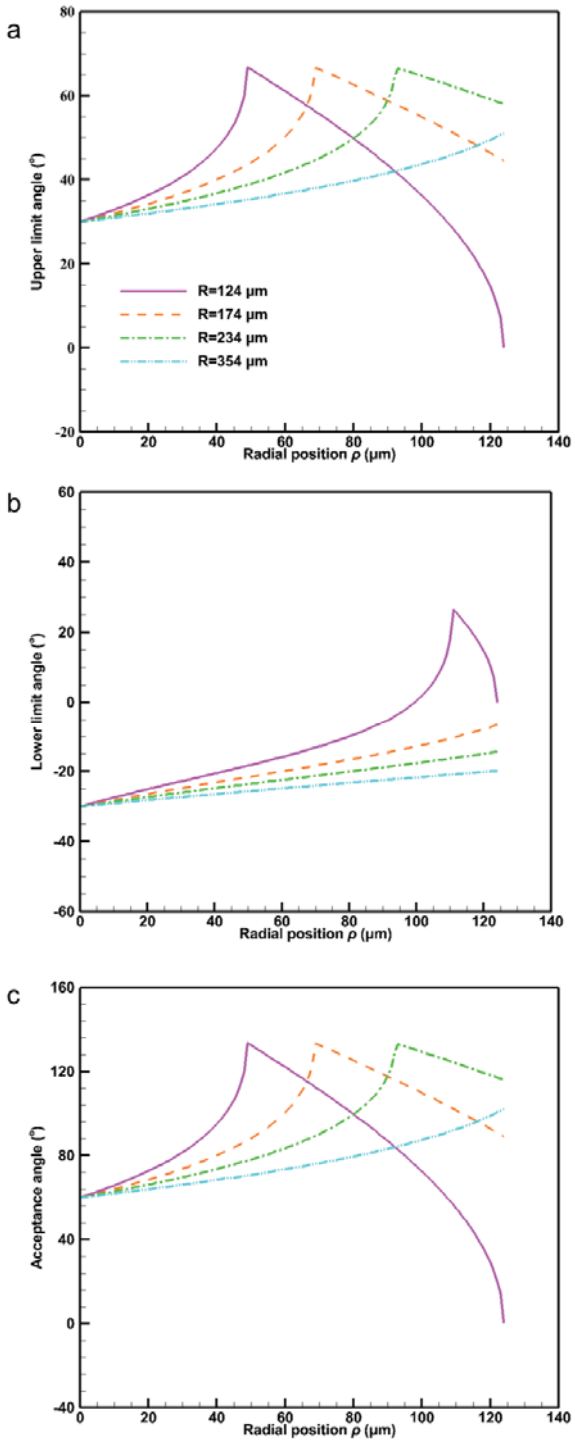

Figure 3-4. Acceptance angles of the *spherical* microlens optical fibres for the microlenses with different radii. a, The upper limit angle, which is theoretically calculated, versus the radial position ρ at which the light hits the

microlens surface (Fig. 3-2c). **b,** The lower limit angle versus ρ (Fig. 3-2d). **c**, The acceptance angle versus ρ.

On the other hand, when light is reflected from the lower core/cladding interface (Fig. 3-2d), $\angle 3$, $\angle 5$ and $\angle 7$ can be calculated with Eqs. (3-4a), (3-4b) and (3-8), respectively. However, $\angle 4$ becomes

$$\angle 4 = \frac{\pi}{2} - (\angle 3 + \angle 5). \tag{3-11}$$

Based on the law of refraction, we have

$$\sin \angle 6 = n_l \sin \angle 4 = n_l \cos\left(\sin^{-1} \frac{\sqrt{n_1^2 - n_2^2}}{n_l} + \cos^{-1} \frac{\rho}{R} \right). \tag{3-12}$$

Since $\angle 6 = \angle 7 + \angle 8$, $\angle 8$ can be expressed as

$$\angle 8 = \sin^{-1}\left[n_l \cos\left(\sin^{-1} \frac{\sqrt{(n_1^2 - n_2^2}}{n_l} + \cos^{-1} \frac{\rho}{R} \right) \right] - \sin^{-1} \frac{\rho}{R}. \tag{3-13}$$

This gives the ***lower*** limit angle $\alpha_{lower} = \angle 8$. The analytic results are plotted in Fig. 3-4b for microlenses with different radii.

Based on the analysis of the optical path, if $\alpha_{lower} \leq 0$, the half acceptance angle φ_{sm} should follow $\varphi_{sm}/2 = \alpha_{upper}$; here, the subscript *sm* represents the spherical microlens. In contrast, if $\alpha_{lower} > 0$, the half acceptance angle should follow $\varphi_{sm}/2 = \alpha_{upper} - \alpha_{lower}$. The analytic results are plotted in Fig. 3-4c for microlenses with different radii, assuming that the material of the microlenses is NOA81 and the refractive index n_l is 1.56 (NOA81, a widely used UV-curable Norland optical adhesive, meets both economic and optical practicality requirements, making it highly suitable as the material for microlenses). In this case, a hollow area is observed in the centre of the acceptance area. A detailed

explanation of the cone will be presented below.

According to the theoretical analysis results (Fig. 3-4c), we find that:

(1) The acceptance angles φ_{sm} at different radial positions ρ vary significantly with the microlens radius R, increasing the difficulty of design and analysis.

(2) In many cases, the acceptance angle has $\varphi_{sm} > 60^{o}$, which is similar to the acceptance angle of 60^{o} of a bare plastic optical fibre. Thus, the **use of a spherical microlens does not reduce the acceptance angle**.

Therefore, the spherical microlens is not a good choice if the acceptance angle of the optical fibre needs to be reduced. Instead, we use a conical microlens to reduce the acceptance angle (Fig. 3-5).

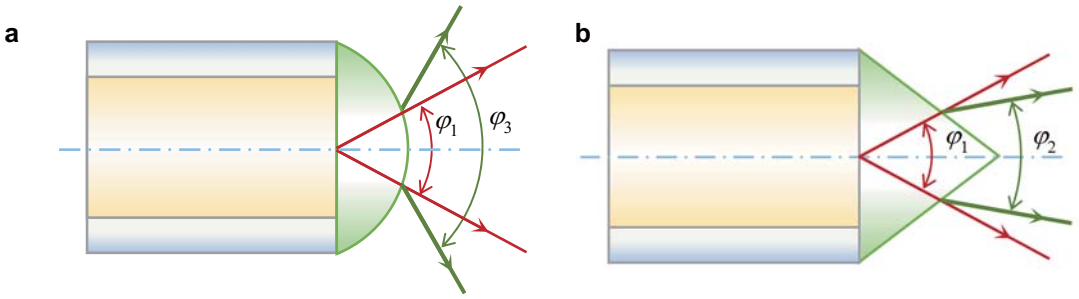

Figure 3-5. Comparison of the acceptance (divergence) angles of the plastic optical fibres with spherical or conical microlenses, with red paths representing the light emitted directly from the bare end of plastic optical fibres, and green paths representing the light emitted from microlenses. a, The spherical microlens has a larger acceptance angle than the flat-end optical fibre (i.e., $\varphi_3 > \varphi_1$). **b,** The conical microlens has a smaller acceptance angle (i.e., $\varphi_2 < \varphi_1$). Therefore, the use of conical microlenses can effectively narrow the acceptance angle.

3.2.3 Acceptance angle of the plastic optical fibre capped with a conical microlens

The acceptance angle (or equivalently, the divergence angle) is strongly affected by whether the light experiences total internal reflection at the conical surface. Thus, we consider two cases, *no reflection* (Fig. 3-2e&f) and *one hop* (Fig. 3-2g&h). Here "hop" means "reflection" at the conical surface (not at the core/cladding interface). These two cases are discussed separately below.

3.2.3.1 No reflection at the conical surface of the microlens

When light is reflected from the upper core/cladding interface (Fig. 3-2e), $\angle 3$ follows Eq. (3-4a). In addition, based on the geometrical relationship, $\angle 5$ and $\angle 6$ follow

$$\angle 5 = \angle 6 = \angle 7 = \frac{\pi}{2} - \theta, \tag{3-14}$$

where θ is half-apex angle of the cone.

Then, based on the law of refraction, we have

$$\begin{aligned} \sin\angle 9 &= n_l \sin(\angle 3 + \angle 5) = n_l \sin\left(\sin^{-1}\frac{\sqrt{n_1^2 - n_2^2}}{n_l} + \frac{\pi}{2} - \theta \right) \\ &= n_l \cos\left(\sin^{-1}\frac{\sqrt{n_1^2 - n_2^2}}{n_l} - \theta \right) \end{aligned}. \tag{3-15}$$

Since $\angle 9 = \angle 7 + \angle 8$, $\angle 8$ is defined as

$$\angle 8 = \sin^{-1}\left[n_l \cos\left(\sin^{-1}\frac{\sqrt{(n_1^2 - n_2^2}}{n_l} - \theta \right) \right] - \frac{\pi}{2} + \theta. \tag{3-16}$$

Similarly, the ***upper*** limit angle α_{upper} should be the smaller value of $\angle 8$ and the angle of the tangent line, which is equal to θ. In φ_{cm}, the subscript *cm* denotes

the conical microlens.

When light is reflected from the lower core/cladding interface (Fig. 3-2f), $\angle 3$ still follows Eq. (3-4a). In addition, based on the geometrical relationship, $\angle 4$ follows

$$\angle 4 = \theta . \tag{3-17}$$

Therefore, $\angle 5$ follows

$$\angle 5 = \frac{\pi}{2} - \angle 3 - \angle 4 = \frac{\pi}{2} - \sin^{-1}\frac{\sqrt{n_1^2 - n_2^2}}{n_l} - \theta . \tag{3-18}$$

Based on the geometrical relationship, $\angle 7$ follows

$$\angle 7 = \angle 3 + \angle 5 = \frac{\pi}{2} - \theta . \tag{3-19}$$

Then, according to the law of refraction, $\angle 9$ follows

$$\begin{aligned} \sin\angle 9 &= n_l \sin\angle 5 = n_l \sin\left(\frac{\pi}{2} - \sin^{-1}\frac{\sqrt{n_1^2 - n_2^2}}{n_l} - \theta\right) \\ &= n_l \cos\left(\sin^{-1}\frac{\sqrt{n_1^2 - n_2^2}}{n_l} + \theta\right) \end{aligned} . \tag{3-20}$$

Since $\angle 9 = \angle 7 + \angle 8$, $\angle 8$ is defined as

$$\angle 8 = \sin^{-1}\left[n_l \cos\left(\sin^{-1}\frac{\sqrt{(n_1^2 - n_2^2}}{n_l} + \theta\right)\right] - \frac{\pi}{2} + \theta . \tag{3-21}$$

Similarly, the ***lower*** limit angle α_{lower} should be the smaller value of $\angle 8$ and the angle of the tangent line, which is equal to θ. In addition, when $\alpha_{lower} \le 0$, the half acceptance angle φ_{cm} (or equivalently, the half divergence angle) follows $\varphi_{cm}/2 = \alpha_{upper}$ (Fig. 3-6a), and when $\alpha_{lower} > 0$, φ_{cm} follows $\varphi_{cm}/2 = \alpha_{upper} - \alpha_{lower}$ (Fig. 3-6b). Thus, we find that the acceptance angle of the cone is independent of

the radial position ρ of the point at which the light hits the conical surface and is only dependent on the half-apex angle θ. This feature is very different from that of the spherical microlens and also makes it easy for analysis.

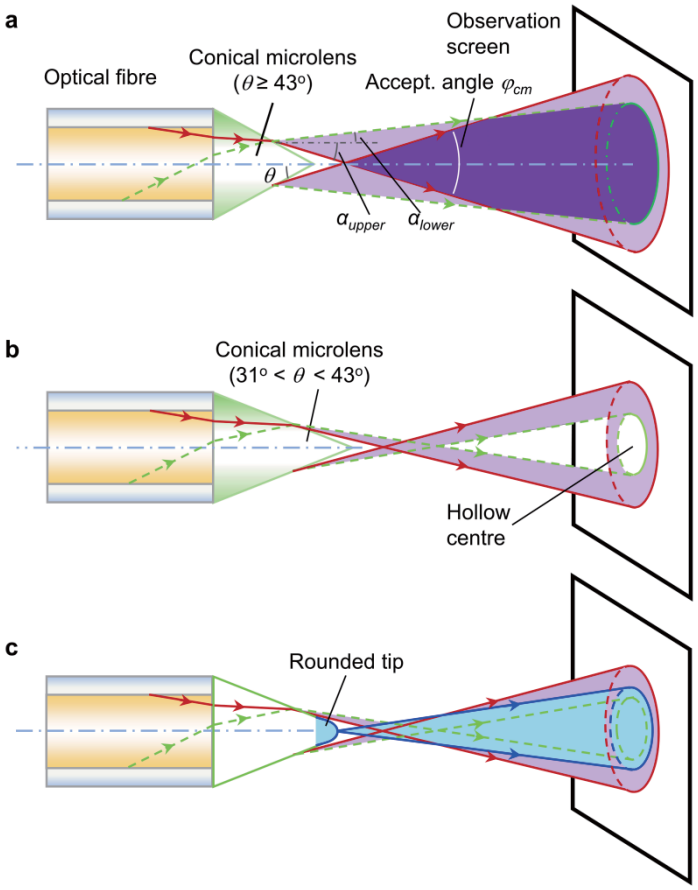

Figure 3-6. Divergence angles of the optical fibres capped with *conical microlenses* with different half-apex angles. Red paths represent light reflected from the upper core/cladding interface of the optical fibre, green paths represent light reflected from the lower core/cladding interface of the optical fibre, and blue paths represent light emitted from the rounded tip of the optical fibre**. a**, When the cone has a half-apex angle $\theta \geq 43^{\circ}$, the rays from the upper core/cladding interface go out at a *downward* angle, and those from the lower core/cladding interface go out at an *upward* angle, forming a solid circle on the observation screen. The acceptance angle is determined by the upper limit angle

α_{upper}. **b**, When $31^o < \theta < 43^o$, the rays from the upper core/cladding interface and the lower core/cladding interface both travel *downwards*, causing a hollow central region on the observation screen. The rays from the hollow central region cannot be collected by the conical microlens optical fibre. **c**, The tip of the cone is rounded to prevent the appearance of the hollow central region.

3.2.3.2 One hop at the conical surface of the microlens

When the light is reflected from the upper core/cladding interface of the optical fibre, $\angle 3$ still follows Eq. (3-4a) (Fig. 3-2g). Based on the geometrical relationship, $\angle 5$ and $\angle 6$ can be expressed as

$$\angle 5 = \frac{\pi}{2} - \theta + \angle 3 . \tag{3-22}$$

$$\angle 6 = \frac{\pi}{2} - \theta . \tag{3-23}$$

Since the sum of the angles in the quadrilateral is 2π, we can formulate the following relationship:

$$\angle 9 + \angle 14 = 2\pi - \left(\frac{\pi}{2} - \angle 3\right) - \angle 6 - 2\angle 5 = \frac{3\pi}{2} + \angle 3 - \angle 6 - 2\angle 5 . \tag{3-24}$$

Next, because

$$\angle 10 = \frac{\pi}{2} - (\angle 9 + \angle 14) = \angle 6 + 2\angle 5 - \angle 3 - \pi , \tag{3-25}$$

we have that

$$\begin{aligned} \angle 10 &= \left(\frac{\pi}{2} - \theta\right) + 2\left(\frac{\pi}{2} - \theta + \angle 3\right) - \angle 3 - \pi = \frac{\pi}{2} - 3\theta + \angle 3 \\ &= \frac{\pi}{2} - 3\theta + \sin^{-1}\frac{\sqrt{(n_1^2 - n_2^2}}{n_l} \end{aligned} . \tag{3-26}$$

Based on the law of refraction, we have

$$\angle 11 = \sin^{-1}\left(n_l \sin\angle 10\right). \tag{3-27}$$

In addition,

$$\angle 13 = \angle 9 + \angle 10 = \angle 6. \tag{3-28}$$

Therefore,

$$\begin{aligned}\angle 12 &= \angle 13 - \angle 11 = \angle 6 - \angle 11 \\ &= \frac{\pi}{2} - \theta - \sin^{-1}\left[n_l \sin\left(\frac{\pi}{2} - 3\theta + \sin^{-1}\frac{\sqrt{(n_1^2 - n_2^2)}}{n_l} \right) \right].\end{aligned} \tag{3-29}$$

Moreover, the angle of the tangent line is $-\theta$. Therefore, when $\angle 12 \geq 0$, the upper limit angle should be $\angle 12$, and when $\angle 12 < 0$, the upper limit angle should be the smaller one of the absolute values of $\angle 12$ and the tangent angle (i.e., the minimum of abs($\angle 12$) versus θ, here abs means taking the absolute value).

When the light is reflected from the lower core/cladding interface of the optical fibre (Fig. 3-2h), $\angle 3$ and $\angle 6$ follow Eqs. (3-4a) and (3-23). Then, based on the geometrical relationship, $\angle 5$ is defined as

$$\angle 5 = \frac{\pi}{2} - \theta - \angle 3. \tag{3-30}$$

Based on the sum of the angles in the quadrilateral, we have

$$\angle 9 + \angle 14 = 2\pi - \left(\frac{\pi}{2} + \angle 3 \right) - \angle 6 - 2\angle 5 = \frac{3\pi}{2} - \angle 3 - \angle 6 - 2\angle 5. \tag{3-31}$$

Then, we have

$$\begin{aligned}\angle 10 &= \frac{\pi}{2} - (\angle 9 + \angle 14) = \angle 3 + \angle 6 + 2\angle 5 - \pi \\ &= \angle 3 + \left(\frac{\pi}{2} - \theta\right) + 2\left(\frac{\pi}{2} - \theta + \angle 3\right) - \pi \\ &= \frac{\pi}{2} - 3\theta - \angle 3 = \frac{\pi}{2} - 3\theta - \sin^{-1}\frac{\sqrt{(n_1^2 - n_2^2}}{n_l}\end{aligned} \quad . \tag{3-32}$$

Based on the law of refraction, we have

$$\angle 11 = \sin^{-1}\left(n_l \sin \angle 10\right). \tag{3-33}$$

In addition, we have

$$\angle 13 = \angle 9 + \angle 10 = \angle 6. \tag{3-34}$$

Therefore, we find that

$$\begin{aligned}\angle 12 &= \angle 13 - \angle 11 = \angle 6 - \angle 11 \\ &= \frac{\pi}{2} - \theta - \sin^{-1}\left[n_l \sin\left(\frac{\pi}{2} - 3\theta - \sin^{-1}\frac{\sqrt{(n_1^2 - n_2^2}}{n_l}\right)\right].\end{aligned} \tag{3-35}$$

Therefore, when $\angle 12 \geq 0$, the lower limit angle should be $\angle 12$, and when $\angle 12 < 0$, the lower limit angle should be the smaller of the absolute values of $\angle 12$ and the angle of the tangent line (i.e., the minimum of abs($\angle 12$) versus θ).

3.2.3.3 Analysis of the acceptance angle

Based on theoretical optical path analysis, when $\theta > 31^o$, the lights emitted by the optical fibres that first impact the conical surface are directly refracted (corresponding to the no-reflection case discussed above; Fig. 3-2e&f), while the one hop case can be ignored. In contrast, when $\theta < 31^o$, the lights that first impact the conical surface experience total internal reflection and thus are reflected once before going out (corresponding to the one hop case discussed above; Fig. 3-2g&h and the red line in Fig. 3-7). Nevertheless, the one hop case

has low output energy. Therefore, we ignore the one hop case in the following discussions.

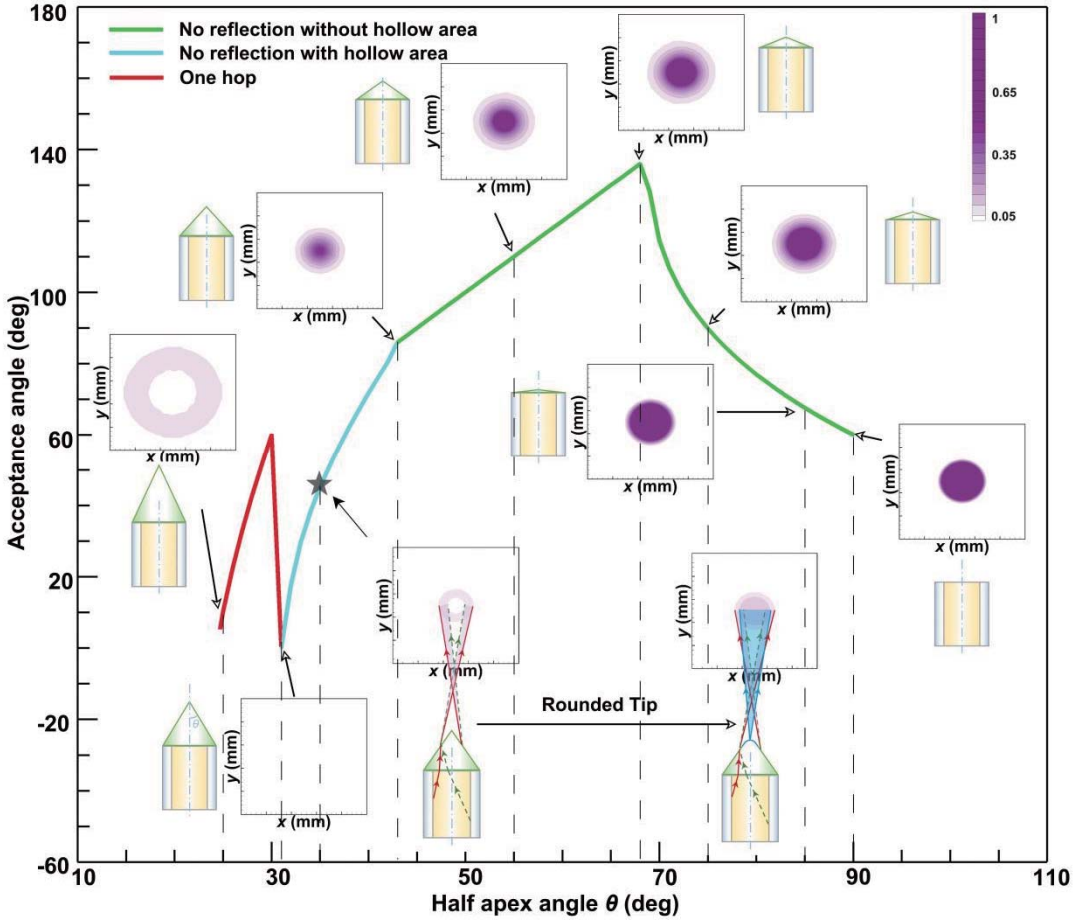

Figure 3-7. Acceptance angle as a function of the half-apex angles θ of the conical microlens. The theoretical analysis is presented using three distinct colour lines to illustrate different scenarios. (1) When $\theta \geqslant 43^{o}$, the green line represents the case in which light is directly emitted from the conical surface of the microlens without any reflection, and there is no hollow region within the emission pattern. However, the acceptance angle is too large (> 60°). (2) When $31^{o} \leq \theta < 43^{o}$, the cyan line represents the case in which light is directly emitted from the conical surface of the microlens without reflection. The acceptance angle is narrowed when θ goes smaller, but a hollow central region appears in the emission pattern. Equivalently, if the fibre collects light, the information in

the central hollow region cannot be detected, which is unfavourable. The star highlights the working conditions used in our experiments, i.e., $\theta = 35^{o}$ and an acceptance angle of 45^{o}. By rounding the sharp tip of the cone, the hollow central region can be eliminated from the emission pattern (the inset in the lower right part). (3) When $\theta < 31^{o}$, the red line represents the case in which the light undergoes a single reflection (or hop) in the conical microlens. The hollow central region reappears and the transmitted light intensity is very low. Therefore, this case is not suitable for collecting the light.

Fig. 3-6a and Fig. 3-6b depict two scenarios of light transmission from the cone. When $\alpha_{lower} \leq 0$ ($\theta \geq 43^{o}$), the critical light from the lower core/cladding interface travels upwards, and the light projected onto the receiving surface forms a circle on the observation screen. Since the microlens is axisymmetric, the actual acceptance area (or equivalently, the divergence area) has a circle shape with no hollow region (Fig. 3-6a). Consequently, the acceptance angle of the cone is determined by the larger absolute value between α_{upper} and α_{lower}. Notably, the absolute value of α_{upper} is consistently larger than α_{lower} based on the theoretical analysis. Therefore, the half acceptance angle $\varphi_{cm}/2$ of the conical microlens is ultimately determined by α_{upper} (i.e., $\varphi_{cm}/2 = \alpha_{upper}$) when $\alpha_{lower} \leq 0$ (Fig. 3-6a, the green line segments in Fig. 3-7).

However, when $\alpha_{lower} > 0$ ($31^{o} < \theta < 43^{o}$), the critical light from the lower core/cladding interface travels downwards, and the light projected onto the receiving surface forms a circle on the observation screen (Fig. 3-6b). The emission pattern on the observation screen is a ring with a hollow region at the centre. In this case, the half acceptance angle of the cone is determined by the

difference between both critical angles, that is, $\varphi_{cm}/2 = \alpha_{upper} - \alpha_{lower}$ (Fig. 3-6b, the cyan line segment in Fig. 3-7). The hollow central region is unfavourable since light information in that angular range is lost.

To eliminate the hollow central region, the tip of the cone can be rounded (Fig. 3-6c). With the rounded tip, the cone can project light to the central region. Equivalently, when used to receive light, the rounded tip can accept light from the central region.

3.3 Optical tracing simulation

An optical tracing simulation is conducted to verify the designs of the cone. Under each condition, the light observation screen is placed 15 cm away from the cone, the cone bottom radius is 0.15 mm, the cone height is determined by θ, and the refractory index at 550 nm is 1.56. The cone sits directly on the flat end of an optical fibre with the following parameters: length, 10 mm; core material, PMMA; core diameter, 0.24 mm; core refractory index, 1.4936 at 550 nm; cladding material, PTFE; cladding diameter, 0.25 mm; and cladding refractory index, 1.4074 at 550 nm. These parameters are consistent with the optical fibres employed in this study. The light is introduced into the other end of the optical fibre and emitted from the cone, forming an emission pattern (i.e., a light intensity distribution) on the observation screen (Fig. 3-6). As θ varies, the emission pattern changes considerably.

We consider the acceptance angle and the corresponding simulated optical field patterns for conical microlens optical fibres at different half-apex angles θ (Fig. 3-7). When $\theta \leq 31^{o}$, no light is directly emitted from the cone. Hence, $\theta =$

31° is the minimum half-apex angle of the conical microlens. As θ decreases ($\theta <$ 31°), the light is reflected one or more times (hops) within the cone before being emitted, and the emission pattern is finally displayed (the red line segments in Fig. 3-7). When 31° < θ < 43°, the acceptance angle increases with larger θ, and a hollow region appears in the middle of the emission pattern (the cyan line segment in Fig. 3-7). When 43° ≤ θ ≤ 68°, the acceptance angle increases further with increasing θ, and the emission pattern is a solid circle (the straight part of the green line segment in Fig. 3-7). When θ > 68°, the acceptance angle decreases as θ increases, and the emission pattern is still a solid circle (the curved part of the green line segment in Fig. 3-7). The simulation results are quantitatively consistent with the theoretical results.

3.4 Choice of shape and size of microlenses

In the artificial compound eye for a panoramic camera (ACEcam), the interommatidial angle $\Delta\Phi$ is 12.2°, while the acceptance angle of the flat-end plastic optical fibre is 60°, causing severe overlap between the views of adjacent ommatidia (Fig. 3-1a). Based on the above analyses, we choose a conical microlens with the half-apex angle θ = 35° (marked with a star in Fig. 3-7). This value serves as a balance between the acceptance angle and the output energy. Specifically, when θ exceeds 35°, the acceptance angle becomes elevated; conversely, if θ falls below 35°, the resultant output energy diminishes to an impractical extent. Correspondingly, the acceptance angle is 45°. At θ = 35°, a hollow centre in the emission pattern cannot be avoided (Fig. 3-7). To address this issue, the sharp tip of the conical microlens is rounded. With this approach,

the rays passing through the rounded part of the conical microlens are refracted towards the central part of the emission pattern, eliminating the hollow centre (Fig. 3-7). In summary, we choose a conical microlens with a rounded tip, a half-apex angle θ of 35^{o}, and an acceptance angle is 45^{o} to ensure that the emission pattern has no hollow centre.

3.5 Fabrication of a conical microlens on an optical fibre

Here, we present a pioneering method for fabricating a conical microlens on an optical fibre (Fig. 4-2a). First, a template with a conical groove array was designed with 3D CAD (Computer Aided Design) software (Fig. 3-8a). The size of the conical groove is equal to the abovementioned conical microlens, and four '+' markers are positioned out of plane at the four corners. Then, this template was fabricated using an ultrahigh precision 3D printing method (microArch® S140, BMF Precision Tech Inc.). Next, polydimethylsiloxane (PDMS) is used to transfer patterns of the template (Fig. 3-8b). This PDMS mould has convex cones and positioning grooves (Fig. 3-8c).

To smooth the rough surface of the convex cones due to the layered texture caused by the 3D printing method and to round the sharp tip of the convex cones, the PDMS mould is electroplated. A several nanometre thick Cu layer was coated on the PDMS surface using the physical vapour deposition method (PVD). The coated PDMS was then electroplated with Cu for 7 h at 1 A/dm^2 electric current density (Fig. 3-8d). Since Cu has a faster deposition rate at positions with higher current density, the edges of the layered texture are connected, forming a smooth surface, and the sharp tip of each convex cone is rounded (Fig. 3-8e).

Subsequently, the Cu-coated PDMS mould was transferred to another PDMS mould (Fig. 3-8f), and this second PDMS mould has conical grooves and '+' positioning markers (Fig. 3-8g).

The material used for the microlens is NOA81, which is liquid and UV curable. A microsyringe was used to deposit the same volume of NOA81 (0.15 μL/drop) into each conical groove (Fig. 3-8h).

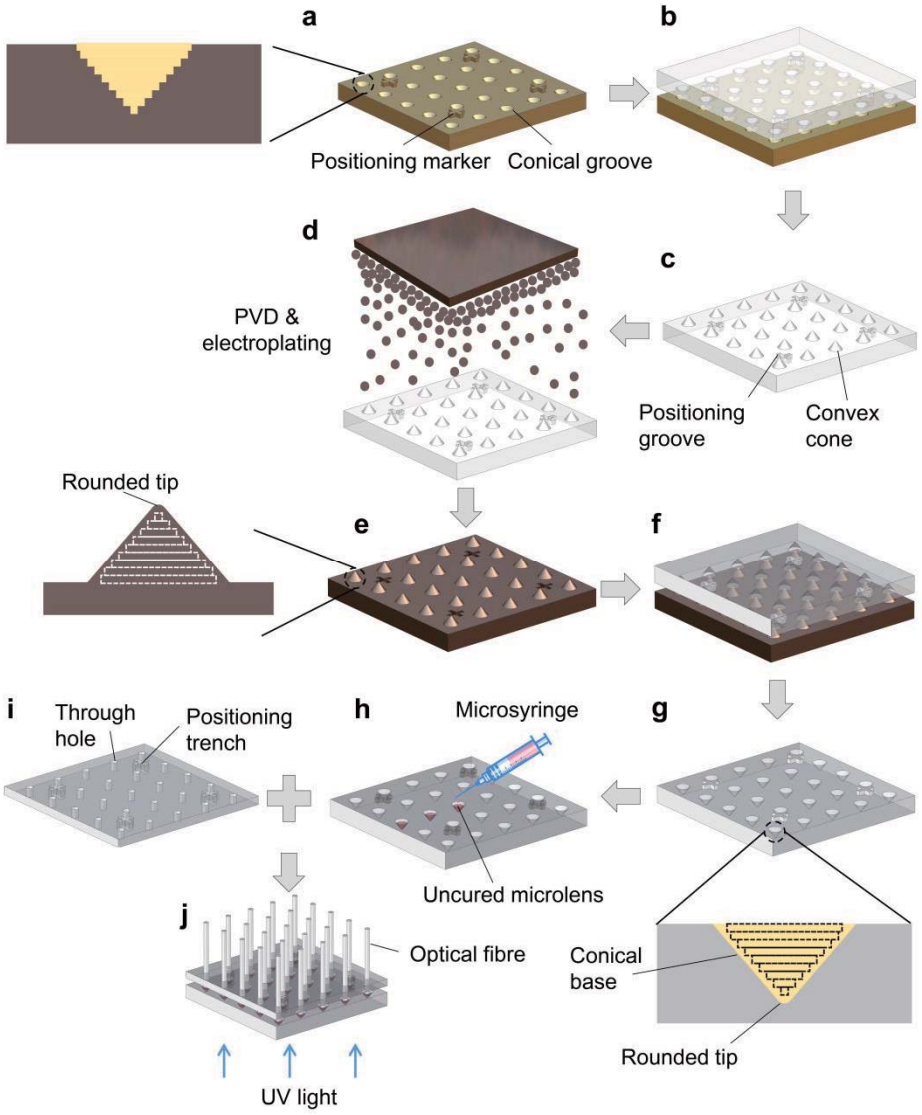

Figure 3-8. Fabrication process flow of conical microlens optical fibres. a, A 3D-printed template with an array of conical grooves and 4 protruded '+' alignment markers at the corners. The enlarged view shows that the conical

surface of each groove has a layered texture and is not smooth. **b,** Polydimethylsiloxane (PDMS) is used to transfer patterns. **c,** The first PDMS mould. **d,** Physical vapour deposition (PVD) and electroplating. **e,** Cu-coated mould. The inset shows that the layered texture is smoothened and the tip of the cone is rounded. **f,** PDMS is used to transfer patterns again. **g,** The second PDMS mould with conical grooves. **h,** The same volume (~0.15 μL) of NOA81 liquid is deposited into each conical groove. **i,** A 3D-printed optical fibre buncher with many through-holes. **j,** UV light is used to cure the conical microlenses on top of the optical fibres.

To mount each microlens on each optical fibre end in a batch process, an optical fibre buncher was designed and fabricated by the 3D printing (Fig. 3-8i). The optical fibre buncher has 4 '+' positioning trenches and an array of through-holes, each corresponding to the position of a conical groove in the second PDMS mould. The through-holes have a diameter of 0.28 mm, which is slightly larger than the diameter of the plastic optical fibre (0.25 mm) to address potential fabrication errors with the 3D printing method (±0.025 mm).

Thereafter, the optical fibre buncher was mounted on the second PDMS mould by carefully aligning the positioning trenches of the former to the protruded positioning markers of the latter under an optical microscope. As a result, each through-hole in the optical fibre buncher is well aligned to one conical groove in the second PDMS mould. Then, the optical fibres were manually threaded into the through-holes to contact the NOA81 microlenses (Fig. 3-8j), followed by a UV illumination to cure the NOA81. With this approach, each conical microlens was firmly fixed on the end of the corresponding optical

fibre.

Oxygen inhibits the free-radical polymerization of liquid NOA81, and the permeability of PDMS in air ensures that an ultrathin surface layer of NOA81 remains uncured near each PDMS surface, though most of the body part of NOA81 is already hardened [101],[102]. This uncured layer facilitates the easy detachment of the NOA81 microlenses from the second PDMS mould. Finally, many conical microlens optical fibres (~ 200 pieces) are obtained with this batch process. Interestingly, the moulds and the fibre buncher can be reused for more fabrication runs of conical microlens optical fibres.

The proposed fabrication method can be extended to create other 2.5D microlens shapes, such as hemispherical microlenses. By modifying the shape of the 3D-printed mould used during the fabrication process, the final microlens shape at the distal end of the optical fibre can be tailored to meet specific design requirements while following the same fabrication steps outlined in this section.

In the future, we aim to simplify this manual process through automation. There are two possible approaches to achieve this automation:

(1) AI-assisted robots: Artificial intelligence (AI) can be utilized to identify the through-holes in both the dome and the buncher. Subsequently, AI can control a robotic arm to insert the plastic microlensed fibres into these holes. The integration of AI with industrial processes has become increasingly popular in recent years due to the rapid advancements in AI technology, and it has the potential to significantly enhance automated fabrication.

(2) Liquid waveguides: Traditional plastic optical fibres could be replaced with new liquid optical guides. Although a recent study attempted to use liquid optical guides by filling silicone elastomer into hollow pipelines within a 3D-

printed black substrate [39], the waveguiding effect was not well achieved due to the layered texture and black colour of the 3D-printed pipeline inner surfaces. Moreover, that recent study did not address the optical design criteria essential for optical waveguides in ACEs. In the future, we can develop microlensed liquid optical guides, consisting of a microlens, liquid optical guide core, and cladding, based on the design criteria discussed in this article. Further, these microlensed liquid optical fibres may be incorporated into the ACEcam components through spin coating.

3.5.1 Fabrication of the PDMS mould

(1) A transparent elastomeric PDMS material and a curing agent are mixed with a mass ratio of 10:1.

(2) The mixture is stirred thoroughly.

(3) The mixture is centrifuged for 2 min at a speed of 1,400 rpm to remove bubbles.

(4) The mixture is poured on the surface of the conical groove template prefabricated by the ultrahigh precision 3D printing method.

(5) The PDMS layer on the template is placed into a vacuum pump under a vacuum environment for 3 h.

(6) The PDMS layer on the template is annealed at 85^{o}C for 45 min.

(7) The cured PDMS layer is peeled off from the template, forming the PDMS mould.

3.5.2 Fabrication of liquid microlenses

(1) A microsyringe (volume 0.15 μL/drop) is used to hold the NOA81 liquid.

(2) The microsyringe is used to inject the same volume of NOA81 into each conical groove.

3.5.3 Mounting the microlenses on the optical fibre

(1) The '+' positioning trenches in the optical fibre buncher are precisely aligned with the protruded '+' positioning markers in the second PDMS mould under an optical microscope.

(2) The optical fibres are individually inserted into the through-holes in the optical fibre buncher until they contact the conical grooves filled with liquid NOA81.

(3) The liquid NOA81 is cured by UV illumination for 2 min.

(4) The optical fibre buncher is carefully removed from the other end of the optical fibres.

(5) The conical microlens optical fibres are removed from the second PDMS mould and further UV cured.

3.5.4 Alignment error analysis

The alignment marks on the PDMS mould and the optical fibre buncher are designed to have the same size to ensure precise alignment. During the alignment process, the elasticity of the PDMS allows the alignment marks on the PDMS to fit into the positioning trenches in the optical fibre buncher, despite being the same size. This alignment process mimics the hard contact alignment used in common multiple photolithography, ensuring high positioning accuracy across different layers. Therefore, the alignment accuracy is correspondingly high.

The alignment error primarily arises from the fabrication error of these

markers, which is less than 0.025 mm (microArch® S140, BMF Precision Tech Inc.). This fabrication error can be further reduced by using devices with a higher precision.

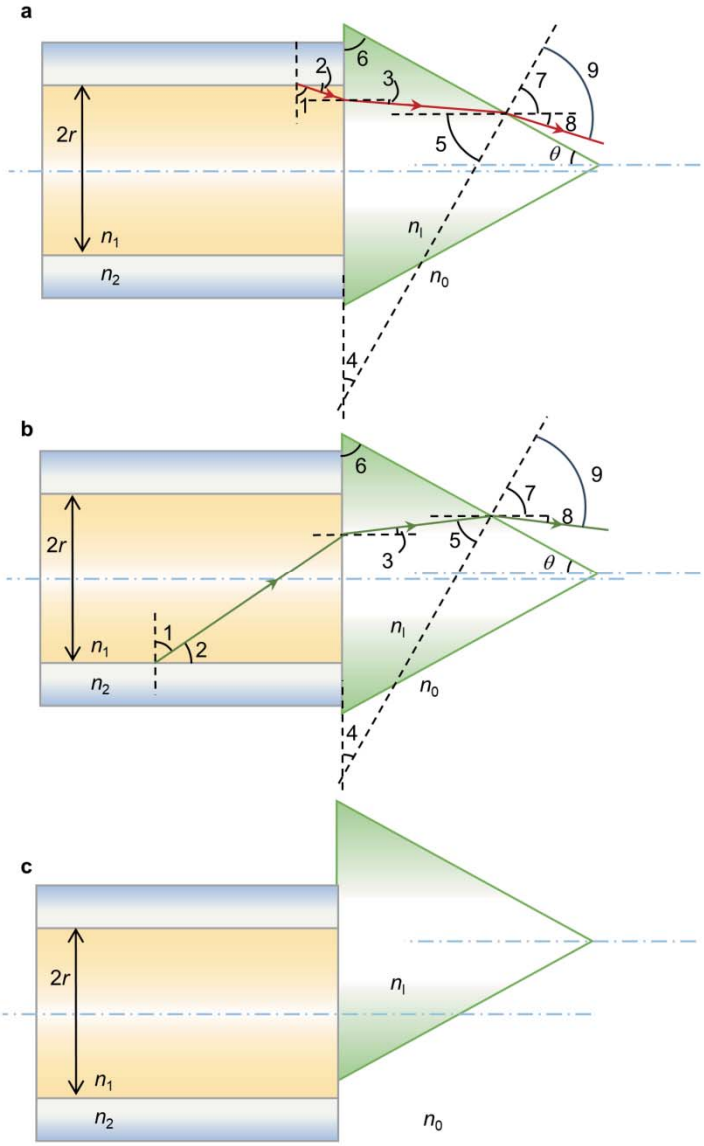

Figure 3-9. Light paths in deviated conical microlens optical fibres for the alignment error analysis. a-b, In the optical fibre capped with a slightly deviated conical microlens, the light has various paths. The light experiences no reflection in the conical surface after being reflected from the upper (**a**) or lower (**b**) core/cladding interface. **c,** Then conical microlens deviates significantly from the optical fibre.

Based on our optical path analysis of this alignment error, when the optical axis of the optical fibre and microlens are slightly deviated (~10 μm), the relationship between the upper limit angle and the half-apex angle (Fig. 3-9a), and the lower limit angle and the half-apex angle (Fig. 3-9b) still comply with the principles described in Section 3.2.3. Thus, this slight error can be considered negligible. Only when the deviation becomes too large (Fig. 3-9c), the acceptance angle of the optical fibre deviates significantly, which would affect the detection performance. Therefore, utilizing four markers to ensure a hard contact alignment is crucial for maintaining optimal performance.

3.6 Summary

This chapter delineates the theoretical analysis of plastic optical fibres and the fabrication process for conical microlensed plastic optical fibres which function as artificial ommatidia. Although plastic optical fibres are a good choice due to their flexibility and durability, the light acceptance angle of a plastic optical fibre is usually large (e.g., 60^{o}). Therefore, the acceptance angle of the optical fibre should be reduced by properly engineering the fibre tip (Fig. 3-1b). Here, we add a microlens with a conical shape onto the distal end of the plastic optical fibre. Although spherical microlenses are easy to fabricate via surface tension and are thus widely used, the use of these microlenses often increases the acceptance angle. In contrast, a conical microlens could reduce the acceptance angle; however, these microlenses with optical smoothness are more difficult to fabricate due to the unique shape and low melting point of plastic optical fibres.

Our analysis and simulations show that a half-apex angle of $\theta = 35^{o}$ is the best choice for the conical microlens, reducing the acceptance angle of the fibre from 60^{o} to 45^{o}. Moreover, the sharp tip of the conical microlens is rounded during the fabrication process. This rounded tip is beneficial since it ensures that light information in the central angular range is not lost.

The conical microlensed plastic optical fibres are fabricated in batches by a sequence of 3D printing, electroplating and two moulding processes, which is a novel approach to add a microlens onto the distal end of an optical fibre. Approximately 200 conical-microlens optical fibres are obtained in each batch process, and each conical microlens has a smooth surface and naturally a rounded tip.

One aspect worth further discussion is that the theoretical analysis method and fabrication process can not only be used to create microlensed plastic optical fibres for artificial compound eyes but also have potential applications in other areas. For instance, the ring light pattern design, which features a hollow central region in the emission pattern, offers promising applications in fields such as endoscopy and machine vision. In endoscopy, this design provides uniform, shadow-free illumination, enabling clearer visualisation of target areas. In machine vision, the ring light pattern enhances edge detection by concentrating light intensity at the periphery, effectively highlighting boundary features and improving object edge illumination.

Chapter 4 Optical fibre based apposition artificial compound eyes for direct static imaging and ultrafast motion detection

This work is reproduced in part from H. Jiang *et al*., "Optical Fibre based Artificial Compound Eyes for Direct Static Imaging and Ultrafast Motion Detection," *Light: Science & Applications*, in press.

Based on the designed and fabricated artificial ommatidia, this chapter will present an apposition ACE. Although many ACEs using various microlens arrays have been inspired before, the reported ACEs have limited performances in static imaging and motion detection. Particularly, it is challenging to mimic the apposition modality to effectively transmit light rays collected by many microlenses on a curved surface to a flat imaging sensor chip while preserving their spatial relationships without interference. In this chapter, we integrate 271 conical microlensed plastic optical fibres into a dome-like structure to faithfully mimic the structure of NCE. This ACE has several parameters comparable to the NCEs: 271 ommatidia versus 272 for bark beetles, and 180° FOV versus 150–180° FOV for most arthropods. In addition, our ACE outperforms the typical NCEs by ~100 times in dynamic response: 31.3 kHz versus 205 Hz for *Glossina morsitans*. Compared with other reported ACEs, this ACE enables real-time, 180° panoramic direct imaging and depth estimation within its nearly infinite depth of field. Moreover, our ACE can respond to an angular motion up to 5.6×10^6 deg/s with the ability to identify translation and rotation, making it

suitable for applications to capture high-speed objects, such as surveillance, unmanned aerial/ground vehicles, and virtual reality.

4.1 Brief introduction

Table 4-1. Detailed comparison of this work with reported artificial compound eyes (ACEs) and natural compound eyes (NCEs)

Specification	**BIC**	**-**	**-**	**Curv -ACE**	**Digital cameras**	**BAC -eye**	**NCEs**	**ACEcam**
Field of view	90°	140°	-	180°×60°	160°	170°	150°-180°	180°
Crosstalk prevention	×	×	√	√	√	√	√	√
Nearly infinite depth of field	√	√	√	√	√	×	√	√
Distance estimation	×	×	×	×	×	×	√	√
Optical guiding	×	×	√	×	×	√	√	√
Panoramic Imaging	×	×	×	×	√	√	√	√
Real-time direct imaging	×	×	×	×	×	√	√	√
Dynamic detection	×	×	×	√	×	×	√	√
Fast motion detection	×	×	×	×	×	×	√	Ultrahigh
Reference	[30]	[108]	[36]	[33]	[7]	[39]	[10],[11],[39],[46],[106],[109]	-
Literature source*	AOM	AFM	Science	PNAS	Nature	NC	-	This work
Generation	1st generation ACEs		2nd generation ACEs				-	-

*: BIC: Biologically Inspired Compound Eyes; CurvACE: Curved Artificial Compound Eye; BAC-eye: Biomimetic Apposition Compound Eye; AOM: Advanced Optical Materials; AFM: Advanced Functional Materials; PNAS: Proceedings of the National Academy of Sciences; NC: Nature Communications.

As mentioned in Chapter 2, NCEs were first investigated by Robert Hooke in 1665 after he observed orderly arranged *pearls* in the cornea of a grey drone fly (Fig. 4-1a) [10]. This research increased interest in NCEs [103]. Later, Sigmund Exner proposed the ommatidium as the basic unit of a compound eye. In each ommatidium of the NCE, light is first collected by a corneal facet lens (i.e., a *pearl*) at a certain acceptance angle and then transmitted by a crystalline cone and rhabdom (i.e., a light guide) to photoreceptor cells [11] (Fig. 4-1b). Ommatidia are further innervated by axon bundles that execute synaptic connections in lamina cartridges [46]. After the primary signal is processed in deeper neural centres, such as the medulla and lobula (Fig. 4-1c) [104], information is finally transmitted to central brain regions. Unlike the monocular eyes of vertebrates, NCEs utilize ommatidia arrayed on a curved surface (Fig. 4-1c). Furthermore, NCEs have many advantages, such as a panoramic FOV, good depth perception, negligible aberration, and fast motion tracking capability [42],[105],[106].

NCEs have inspired the development of artificial compound eyes (ACEs) based on planar microlens arrays [21], curved microlens arrays [7],[8],[30],[33],[36], and metasurfaces [28] as mentioned in Chapter 2. In ACEs, the photodetector cells are arranged on either curved [7],[8],[33] or planar [39] surfaces. Nevertheless, most of the reported ACEs do not faithfully replicate the NCE structures and therefore lack some of their advantages. Since ACE designs using planar microlens arrays or metasurfaces usually have limited FOVs [107], they are therefore not investigated in this study. ACEs with curved microlens arrays are briefly compared in Table 4-1. Specifically, the 1st generation ACEs

primarily focused on the fabrication of ACE microlenses, lacking the ability to achieve panoramic imaging and dynamic detection [30],[108] (Fig. 4-1d). In the 2nd generation ACEs, some showed the capability of panoramic imaging, but they needed post-processing to retrieve the images, such as single-pixel imaging technique [6], scanning method with mapping algorithm [7],[8] and backpropagation neural networks [9]. Despite recent efforts on real-time direct imaging, those ACEs still struggled with quantitative distance estimation [39]. Some other ACEs could realise dynamic motion detection but at common speeds [33]. Nevertheless, none of those ACEs can match the NCEs in achieving real-time panoramic direct imaging and dynamic motion detection simultaneously (Fig. 4-1d, Table 4-1). Currently, the main challenge with curved microlens array-based ACEs is how to transmit the light rays collected by many microlenses on a curved surface to a flat imaging sensor (e.g., a CMOS chip) while maintaining their spatial relationships. Optical waveguides could address this challenge, as presented in one recent study [39] that filled silicone elastomer into the hollow pipelines in a 3D-printed black substrate. Nevertheless, the waveguiding effect was unmet due to the layered texture and the black colour in the 3D-printed pipeline inner surfaces. Additionally, it did not mention the optical design criteria that are essential for optical waveguides in ACEs. Luckily, conical microlensed plastic optical fibres mentioned in Chapter 3 are promising to solve this challenge.

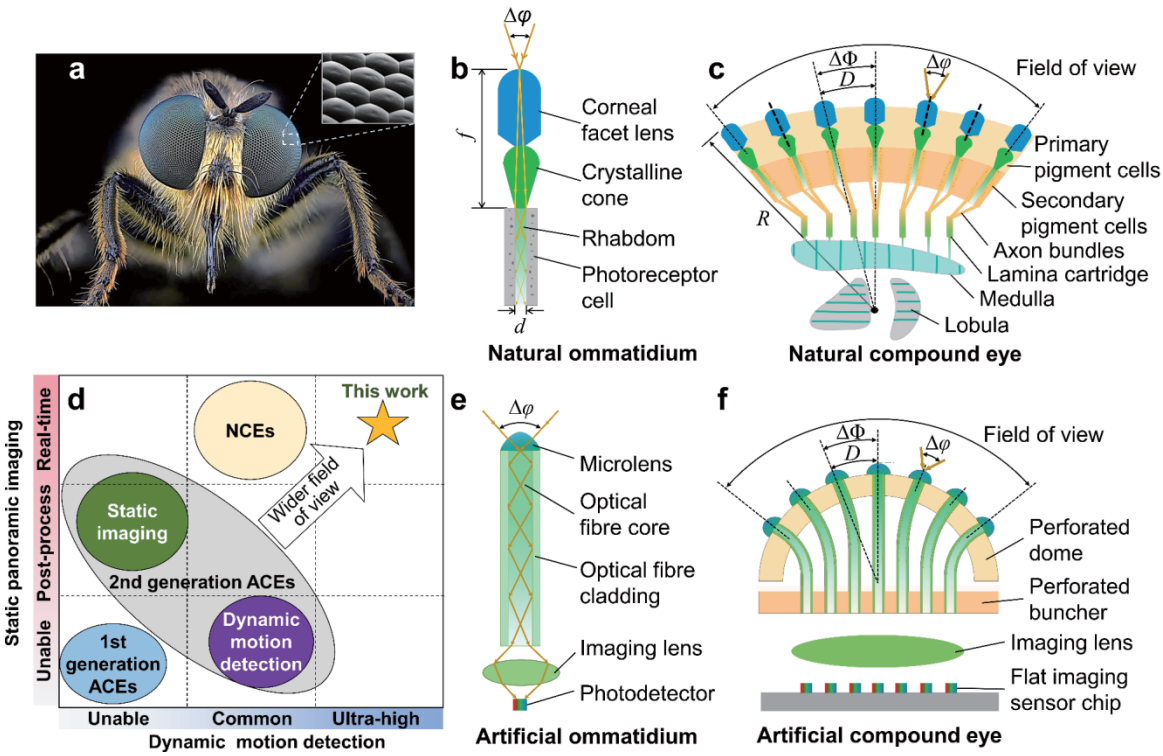

Figure 4-1. Concept and principle of the artificial compound eye for a panoramic camera (ACEcam) that uses conical-microlens optical fibres to mimic natural ommatidia. a, The fly *Choerades fimbriata* has natural compound eyes (NCEs) for imaging; photograph courtesy of Mr. Thorben Danke of Sagaoptics. The inset shows compactly arranged corneal facet lenses in the NCEs. **b,** In a natural ommatidium, the facet lens with a focal length f collects light at a specific acceptance angle $\Delta\varphi$, the crystalline cone ensures light convergence, the rhabdom (diameter d) transmits light through the inner structure, and the photoreceptor cell records the light information. **c,** An NCE consists of numerous natural ommatidia, which are surrounded by pigment cells to prevent crosstalk. Here, the interommatidial angle $\Delta\Phi = D/R$, where D and R denote the arc distance of adjacent ommatidia and the local radius of curvature, respectively. **d,** Comparison of different compound eyes in the functions of static panoramic imaging and dynamic motion detection. The 1st generation ACEs

primarily focused on the fabrication of ACE microlenses, lacking the ability of static imaging or dynamic detection. In the 2nd generation ACEs, none of these ACEs could realise real-time panoramic direct imaging and dynamic motion detection simultaneously, as what the NCEs can do. In contrast, our ACEcam is comparable to the NCEs in aspects of 180^{o} field of view and static imaging, and surpasses the NCEs in ultrafast motion detection. **e,** An artificial ommatidium closely resembles a natural ommatidium by using a microlens to mimic the facet lens and the crystalline cone, an optical fibre core to mimic the rhabdom, an optical fibre cladding to mimic the pigment cells, an imaging lens to mimic synaptic units to focus each optical fibre onto an individual photodetector, and a photodetector in the flat imaging sensor chip to mimic the photoreceptor cell. **f,** An artificial compound eye consists of numerous artificial ommatidia, with a flat imaging sensor chip mimicking the deeper neural centres (medulla and lobula), where signals are pre-processed. The signals are then transmitted to a computer for further analysis.

In this chapter, conical microlensed plastic optical fibres (Fig. 4-2a) mimic the structure and functions of a natural ommatidium (Fig. 4-1e). The lensed ends of 271 fibres (versus 272 ommatidia for bark beetles [109]) are incorporated onto a curved surface (Figs. 4-1f & 4-2b) and used to assemble a biomimetic ACE as a panoramic camera (Fig. 4-2c). The ACEcam faithfully mimics the structure of apposition ACEs and excels in both static and dynamic perceptions, thus finding niche applications in diverse imaging and dynamic detection domains.

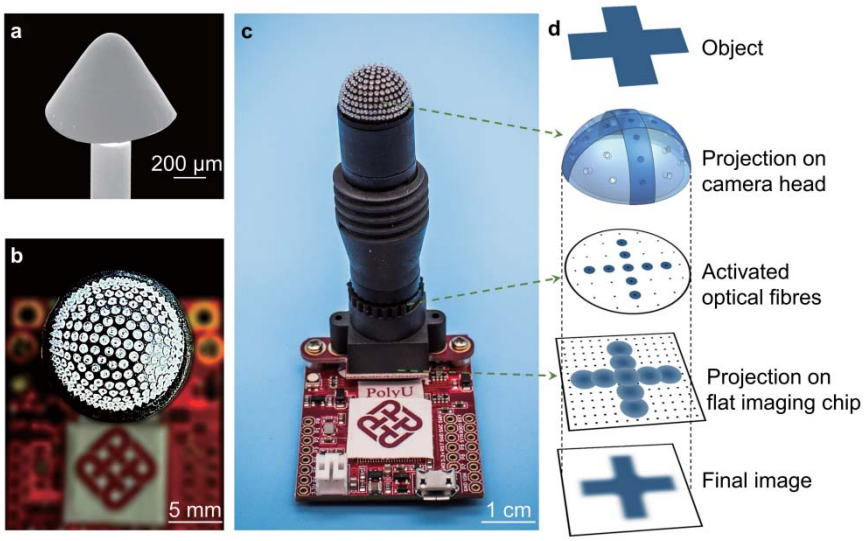

Figure 4-2. Operating principles and fabrication of the ACEcam. a, Scanning electron microscopy (SEM) image of the conical microlens on an optical fibre. **b,** Top view of the ACEcam light receiving head that uses a 3D-printed dome to host 271 fibre ends. **c,** Photograph of an assembled ACEcam. **d,** Concept of image formation. Using a '+' line-art pattern as the object (top panel), some fibres receive light from the object (second panel), and this pattern is transmitted from the lens end to the other end of the fibre (third panel). An imaging lens is employed to project the light from the fibre ends to a flat imaging sensor chip (fourth panel top), which is then converted into the final digital image (bottom panel).

4.2 Assembled device

In the NCE, if the ommatidium acceptance angle is $\Delta\varphi = d/f$ and the interommatidial angle is $\Delta\Phi = D/R$ (Fig. 4-1b&c), $\Delta\varphi$ should be slightly larger than $\Delta\Phi$ to ensure that no angular information is lost while reducing redundant angular overlap; here, d, f, D and R denote the rhabdom diameter, the focal

length of the facet lens, the arc distance of adjacent ommatidia and the local radius of curvature, respectively as mentioned in Chapter 2 [47]. Similarly, in ACEcam, $\Delta\varphi$ should be only slightly larger than $\Delta\Phi = 12.2^{o}$ (Fig. 4-1f). Otherwise, the receiving areas of adjacent fibres would have a large overlap, lowering the angular resolution (Fig. 3-1a). Therefore, conical microlensed plastic optical fibres mentioned in Chapter 3 are utilized in this assembled device.

In the assembly, 271 conical microlensed plastic optical fibres (Fig. 4-2a) are attached to a 3D-printed perforated dome (diameter 14 mm, Methods 4.5.1, Fig. 4-8a-b) so that all the lensed ends of the fibres are on the dome surface (Fig. 4-2b), while the bare ends of the fibres are placed into a perforated planar buncher (Fig. 4-8c). Light leaving the bare fibre ends is projected onto a flat imaging sensor via an imaging lens (Fig. 4-1f). The dome, the buncher, the imaging lens and a flat imaging sensor chip are hosted in a screwed hollow tube (Fig. 4-8d). In the assembly, the 3D-printed dome has the black colour so as to absorb the leaked or stray light, functioning the same as the pigment cells in the NCEs to prevent crosstalk. The lensed plastic fibres confine the collected light, preventing crosstalk and the associated ghost images, and the buncher maintains the relative positions of the microlenses on the dome. This setup enables the light collected at the curved surface to be transmitted to a flat image sensor, thus faithfully replicating the ommatidia in an NCE.

In the image formation process, the light emitted by the object is captured at different angles by the microlenses on the dome (Fig. 4-2d). At the bare fibre ends, the planar images are projected onto the flat imaging sensor chip. Then, the final images are obtained for digital image processing. The imaging lens prevents contact of the bare fibre ends with the vulnerable image chip surface.

After the assembly process, the fabricated ACEcam is ready for experiments.

4.3 Static imaging

Previous studies on ACEs focused on static imaging (e.g., point-source tracking and panoramic imaging [7],[8]) or dynamic motion extraction [33]. Nevertheless, static imaging usually requires a complex scanning system, which considerably reduces the imaging rate [7], whereas dynamic motion extraction often obtains mosaic results due to the discrete distribution of photodetectors on the curved surface [33]. The proposed ACEcam can perform both static imaging and dynamic motion detection and has several advantages. First, this design has an exceptionally wide FOV (i.e., 180^{o}). For experimental verification, laser spots are illuminated from 90^{o} to 0^{o} at steps of 22.5^{o} in both the *x* and *y* directions (see Fig. 4-3a for the combined result and Fig. 4-9 for the individual images). Over the whole 180^{o} FOV, the images are highly uniform in size, brightness and angular position. This 180^{o} FOV helps ACEcam to exceed most ACEs to capture wider light information, and thus to be more suitable in various applications such as surveillance and unmanned drones.

Secondly, ACEcam also supports real-time panoramic direct imaging without distortions. Different test patterns, such as the logo of our university and the letters 'HK', can be imaged clearly with ACEcam (Fig. 4-3b&e and Fig. 4-10). Unlike the ACEs developed in prior studies, which required redundant postprocessing approaches [6]-[9], ACEcam enables direct imaging, similar to the capabilities of real NCEs. In addition, object distances can be estimated (i.e., depth estimation). In these experiments, a checkerboard pattern is set at different object distances from the camera (red lines in Fig. 4-3c), and the grey values at

different distances along the vertical edge direction (pink lines in Fig. 4-3c) are analysed to determine the relationship between the point spread parameter σ and the reciprocal of the object distance u^{-1} (Fig. 4-3d), which should theoretically follow a linear relationship [110],[111] (Appendix A.2). Given the point spread parameter σ based on a measured image, the distance u can be obtained directly from the fitting expression. The absolute value of this slope is defined as the critical parameter m of the camera in this work, representing how the imaging quality of the camera is affected by the object distance. Here, the ACEcam is determined to have a value of m = 17.42 (Fig. 4-3d, Appendix A.2). If other images with unknown distances are captured, their σ values can be calculated, and then their distances u can be determined using the linear curve between σ and u^{-1}. Next, the letters 'HK' are placed at three different angular positions: -50^{o} (left), 0^{o} (centre) and 50^{o} (right). No image distortions are observed (Fig. 4-3e), showing the good panoramic imaging performance of ACEcam. In comparison with other ACEs that attain panoramic imaging through redundant post-processing methods [6]-[9], the capabilities of real-time direct imaging and object distance estimation of our ACEcam make it versatile across a broader range of applications. For instance, it can capture images and measure distances among moving objects in reality.

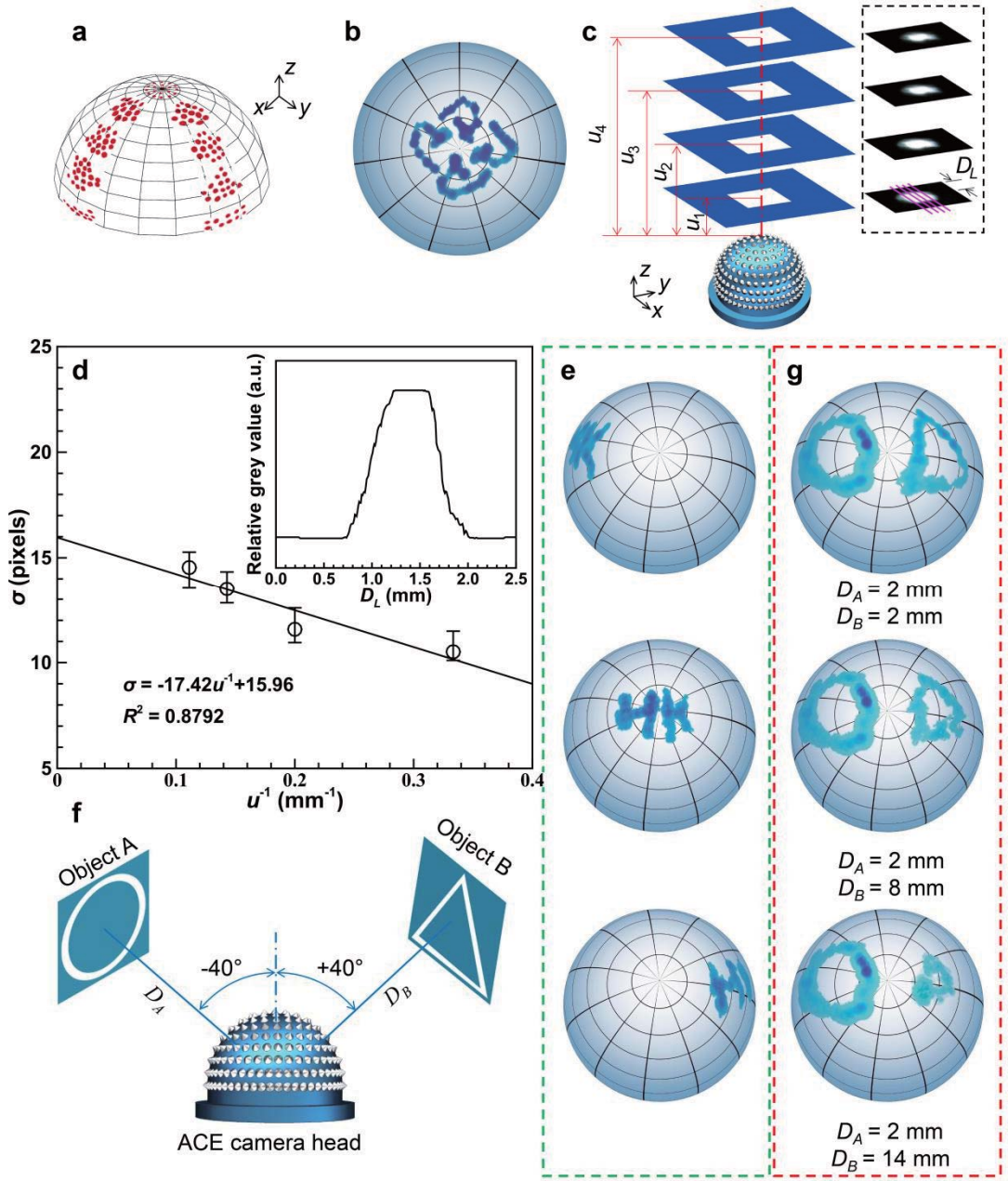

Figure 4-3. Static imaging and depth estimation of the ACEcam. a, Combined image of a laser spot from nine angles (from -90° to 90° in both the *x* and *y* directions at a step of 22.5°). **b,** Image of the logo of The Hong Kong Polytechnic University. **c and d,** Depth estimation using the linear relationship between the point spread parameter σ and the reciprocal of the object distance u^{-1}. In **c**, example images at four different distances u_1 = 3 mm, u_2 = 5 mm, u_2 = 7 mm, and u_4 = 9 mm are shown in the dotted box. In the image acquired at each

distance, the grey values along four parallel lines (shown here in pink) in the *x* direction are analysed to calculate the mean value and the errors shown in **d**. D_L is the distance between a point on the pink line and the upper boundary of an image. In **d,** the inset shows the relative grey value distribution along one sample pink line in **c**. A low error range signifies a high reliability of ACEcam's depth estimation. **e,** Images of the letters 'HK' captured at three different polar angles relative to the centre of the camera: -50° (top), 0° (centre) and 50° (bottom). **f,** Schematic of an experimental setup to verify the nearly infinite depth of field of ACEcam. Objects A (circle) and B (triangle) are placed at angular positions of -40° and 40°. **g,** Images of the circle and triangle patterns when the distance of the circle image is fixed at D_A = 2 mm and the distance of the triangle image varies from D_B = 2, 8 to 14 mm.

The third merit is the nearly infinite depth of field. To verify this property, two objects, a circle and a triangle, are placed at two widely separated angles and different distances (Fig. 4-3f). When the distances of both objects are the same, the image sizes are similar (Fig. 4-3g and Supplementary Video A-1). When the circle image is kept static and the triangle image is moved away from ACEcam, the circle image size remains unchanged, but the triangle image size decreases. The focus is always retained. The nearly infinite depth of field of ACEcam is attributed to the image formation process, as each fibre captures all the light information within its acceptance angle, regardless of the object distance. Compared with the ACEs without infinite depth of field [39], this characteristic enables the ACEcam to perform better in certain fields, including applications in virtual reality and augmented reality, contributing to an enhanced sense of

realism in augmented reality experiences.

4.4 Dynamic detection

Real-time perception ensures that the ACEcam is suitable not only for static imaging but also for dynamic detection. The fourth merit is that ACEcam can also be applied to determine optical flow according to visual translation and rotation signals. Here, the Lucas-Kanade method is adopted as the data processing algorithm due to its high efficiency in computing two-dimensional optical flow vectors based on images [112],[113] (Appendix A.3). In these experiments, when the ACEcam is placed 10 mm in front of a checkerboard pattern and moved vertically (Fig. 4-11a), the computed optical flow vectors have uniform direction and length, illustrating the reliability and stability of ACEcam in dynamic motion detection (Fig. 4-4a). Since the checkerboard pattern has alternating dark and bright regions, the direction and length of the vector represent the direction and velocity of the motion of a bright region. Moreover, when the ACEcam is rotated (Fig. 4-11b), the rotation centre can be easily identified (dark dot in Fig. 4-4b) since the length of the optical flow vector has a linear relationship with the distance from the rotation centre. This motion detection capability of ACEcam may facilitate various applications, such as kinestate tracking and motion state control in robots and unmanned aerial vehicles.

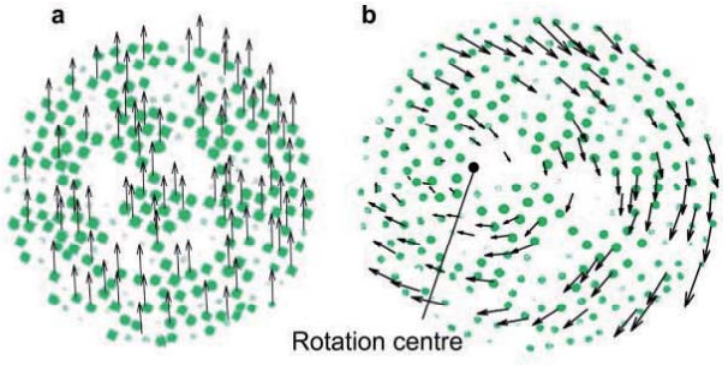

Figure 4-4. Dynamic motion detection of the ACEcam. a, Optical flow as the ACEcam is translated in front of a checkerboard pattern at a distance of 10 mm. Here green dots represent the ommatidia illuminated by bright squares of the checkerboard, and the direction and length of the vector denote the motion direction and velocity of a bright square. **b,** Optical flow as the ACEcam is rotated, with the dark spot indicating the calculated rotation centre.

As the fifth merit, ACEcam shows ultrafast angular motion perception capability. To demonstrate a simple object with a fast angular motion, 5 LEDs are equally spaced over 180° and sequentially activated by square waves with a period of Δt (Fig. 4-5). When a CMOS chip (OV7725, OmniVision Technologies Inc., 30 fps) is used as the photodetection unit, the frame rate is 30 Hz, and the angular perception is limited to 5.4×10^3 deg/s (Methods 4.5.2.1 and Supplementary Video A-2). Similarly, three 'T' objects are equally spaced over 180° and sequentially activated by square waves with a period of Δt (Supplementary Fig. A-1) to further demonstrate the angular motion perception capability (Supplementary Video A-3). Due to the frame rate limitations of the chip, a high flicker frequency $f_{flicker}$ may lead to missing the recording of some

objects.

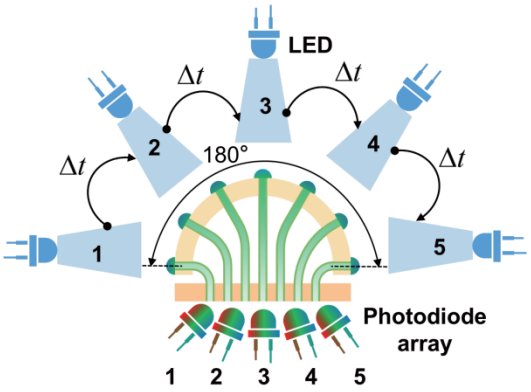

Figure 4-5. Experimental setup to generate very high angular velocities for the dynamic response measurement. Five LEDs are evenly spaced along 180° and lit up successively with a delay time Δt whose minimum value is equal to the response time of the photodiode Δt_{dec}, and five photodiodes are employed to record the light emitted by the corresponding LEDs.

To further investigate ACEcam's angular motion perception capability, a photodiode array with 5 electromagnetically shielded photodiodes (ElecFans) is used (Fig. 4-5), and the light produced by flickering LEDs is recorded with these photodiodes. When $f_{flicker}$ = 24 Hz is close to human flicker fusion frequency (FFF) [3],[5], the photodiodes get smooth response curves (Fig. 4-12). And, when $f_{flicker}$ = 240 Hz is close to the FFF of the fly *Glossina morsitans* (FFF = ~ 205 Hz [4],[14]), the photodiode signals remain smooth (Fig. 4-6a). To test the limit, the LEDs are set at $f_{flicker}$ = 31.3 kHz, which matches the response time of the photodiodes used in this experiment (i.e., 31.9 μs) and is ~100 times higher than the typical FFF of NCEs, the detected electrical signals of photodiodes change from a square wave to a spike wave (Fig. 4-6b). Equivalently, the ACEcam can respond to an angular velocity of up to 5.6×10^6 deg/s (Methods

4.5.2.2 and Supplementary Video A-4), which can be further improved by several orders using faster photodiode arrays (e.g., 28 Gbit/s, PD20V4, Albis). This property broadens the application range to high-speed objects, such as aeroplanes and even spacecraft, a capability that is impossible for common ACEs.

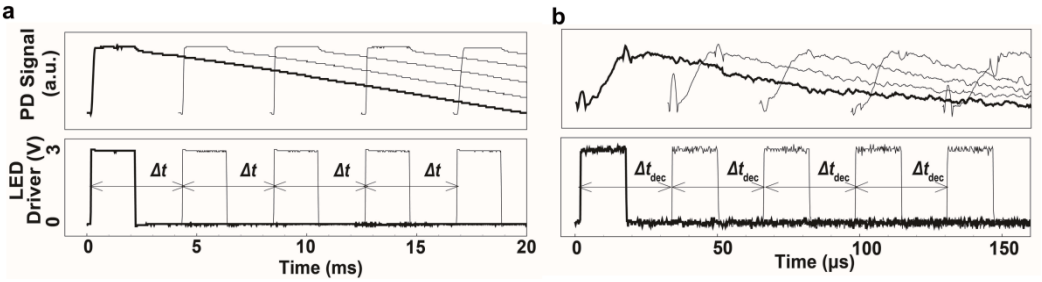

Figure 4-6. Response signals of the photodiodes (upper panel) when the LEDs are driven by square waves (lower panel) of $f_{flicker}$ = 240 Hz in a and 31.3 kHz in b.

In future work, commercial high-speed cameras can be incorporated to directly capture imaging results. This approach will provide more intuitive and visually accessible data, improving the presentation and analysis of high-speed dynamic motion detection.

The compelling reason behind ACEcam's remarkable ultrafast angular motion perception lies in its emulation and surpassing of NCEs' signal transmission. In contrast to spiking neurons, which exhibit an "all-or-none" behaviour due to their refractory period, nonspiking graded neurons in insects have multilevel responses and temporal summation characteristics when stimulated sequentially (Supplementary Fig. A-2) [14],[114]. This feature allows for a significant increase in the signal transmission rate between the retina and lamina neurons from approximately 300 bit/s (spiking neurons) to 1650 bit/s (nonspiking graded neurons) [15]. This feature enhances the performance of

NCE visual systems. In our ACEcam, we have simplified the signal conversion process from that of natural ommatidium, which involves multiple steps (e.g., photosignals to histamine biological signals, then to electric signals; Fig. 4-7a); specifically, in the artificial ommatidium, only one signal transduction step is needed (i.e., photosignals to electric signals; Fig. 4-7b). Thus, the theoretical limit of the signal transmission rate is determined only by the frequency response of individual photodetection units (e.g., photodiodes), which could reach up to 50 Gbit/s, 7 orders of magnitude higher than that in the natural ommatidium. The distinctive anatomical structure empowers the ACEcam with significant potential for ultrafast angular motion perception, surpassing not only the existing ACEs but also outperforming the NCEs, and thus this characteristic serves as a blueprint for advancing ACE development.

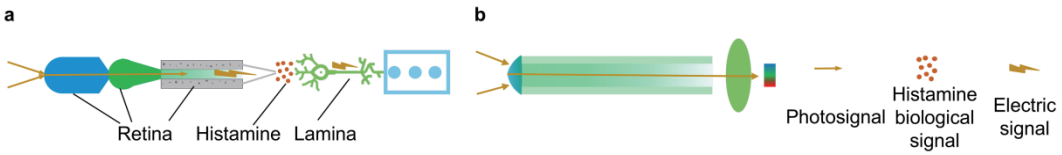

Figure 4-7. Signal transmission pathway in the natural ommatidium (a) and the artificial ommatidium (b).

4.5 Materials and methods

4.5.1 Fabrication of artificial compound eyes for a full-vision camera

The 3D-printed components are illustrated in Fig. 4-8. First, a dome (Fig. 4-8a, b, external radius R = 7.0 mm, open angle 180°) and a buncher (Fig. 4-8c) were 3D-printed by projection micro stereolithography (microArch® S140, BMF Precision Tech Inc.). To allow for positioning each of the fibres, 271 through-

holes with a diameter of 280 μm were evenly distributed in the dome (the number of through-holes from the centre to the outermost ring increases evenly, with values of 1, 6, 12, 18, 24, 30, 36, 42, 48, and 54, ensuring a uniform distribution) and another 271 through-holes were evenly distributed in the buncher. Then, 271 conical microlens optical fibres (external diameter d = 250 μm) were manually threaded through the holes in both the dome and the buncher while maintaining the relative positions of the optical fibres. The microlens ends of the optical fibres were placed on the curved surface of the dome, and the other ends of the optical fibres were cut to the same length after being passed through the buncher so that the fibre ends formed a flat surface. Next, the dome and the buncher were placed in a screwed hollow tube (Fig. 4-8d). This hollow tube was connected to another tube containing an imaging lens (standard M12 camera lens) and a flat imaging sensor chip (OV7725, OmniVision Technologies Inc.) (Figs. 4-1f&4-2c). With this setup, the light rays received by the microlenses on the curved surface (i.e., the surface of the dome) could be transmitted to the planar surface (i.e., the surface of the buncher) and projected through the imaging lens to the flat surface of the imaging sensor chip.

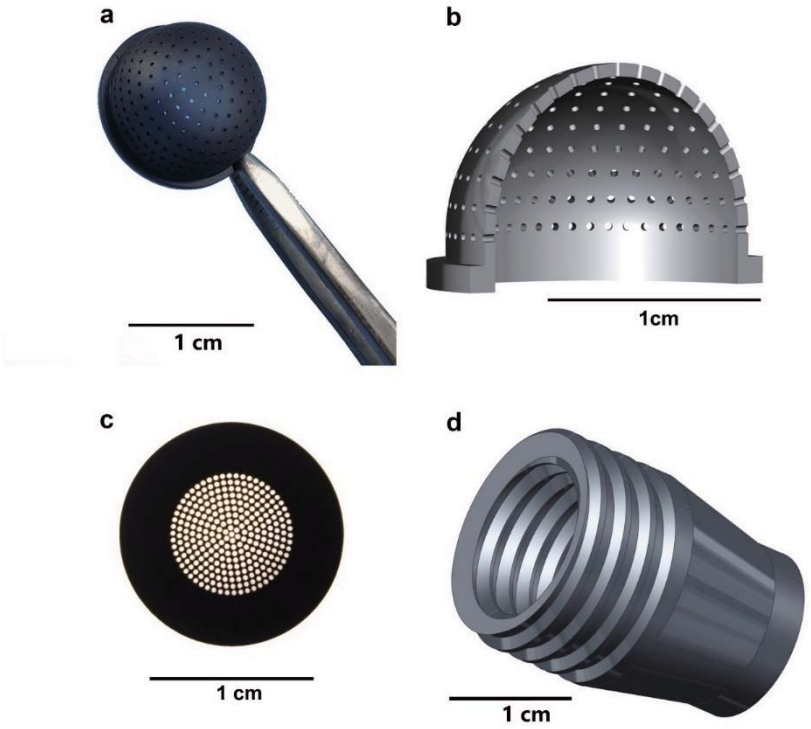

Figure 4-8. 3D-printed components for the assembly of ACEcam. a, Photograph of the perforated dome, held by tweezers. **b,** Design of the perforated dome. **c,** Photograph of the perforated buncher. **d,** Design of the screwed hollow tube that will be used to hold the dome and the buncher.

4.5.2 Calculation of maximum angular velocities

4.5.2.1 Using a CMOS chip as the photodetection unit

In our testing setup (Fig. 4-5), the moving object is mimicked by 5 equally spaced and sequentially driven LEDs. The delay time Δt_1 when one object moves from one side of the dome to the opposite side can be determined by the FOV and the angular speed ω as follows:

$$\Delta t_1 = \frac{\mathrm{FOV}}{\omega}. \tag{4-1}$$

The moving object is mimicked by 5 sequentially driven LEDs; thus, Δt_1

should be greater than or equal to the response time Δt_{dec} of the photodetector,

$$\Delta t_1 \geq \Delta t_{dec}\,. \tag{4-2}$$

The combination of both equations gives

$$\omega \leq \frac{\mathrm{FOV}}{\Delta t_{dec}}, \tag{4-3}$$

and, thus, the maximum angular velocity is given by

$$\omega_{\max} = \frac{\mathrm{FOV}}{\Delta t_{dec}}\,. \tag{4-4}$$

The response time of a CMOS chip with a frame rate of 30 Hz is 33.3 ms. Correspondingly, the highest angular perception speed is

$$\omega_{\max} = \frac{180°}{33.3\times10^{-3}} = 5.4\times10^{3}\ \mathrm{deg/s}\,. \tag{4-5}$$

4.5.2.2 Using a photodiode array as the photodetection unit

When a photodiode array with 5 electromagnetically shielded photodiodes (ElecFans) is used for photodetection, the response time is 31.9 μs (equivalently, 31.3 kHz). In this case, the highest angular perception speed is

$$\omega_{\max} = \frac{\mathrm{FOV}}{\Delta t_{dec}} = \frac{180°}{31.9\times10^{-6}} = 5.6\times10^{6}\ \mathrm{deg/s}\,. \tag{4-6}$$

4.5.3 Extended data figures

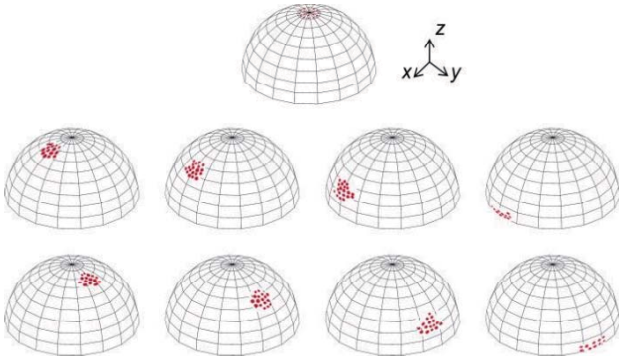

Figure 4-9. Images of the laser spots projected onto the full-field camera. The images are acquired at 9 different incident angles (from 0° to 90° in the *x* direction and the *y* direction in steps of 22.5°). They are rendered on a hemispherical surface for easy visualization.

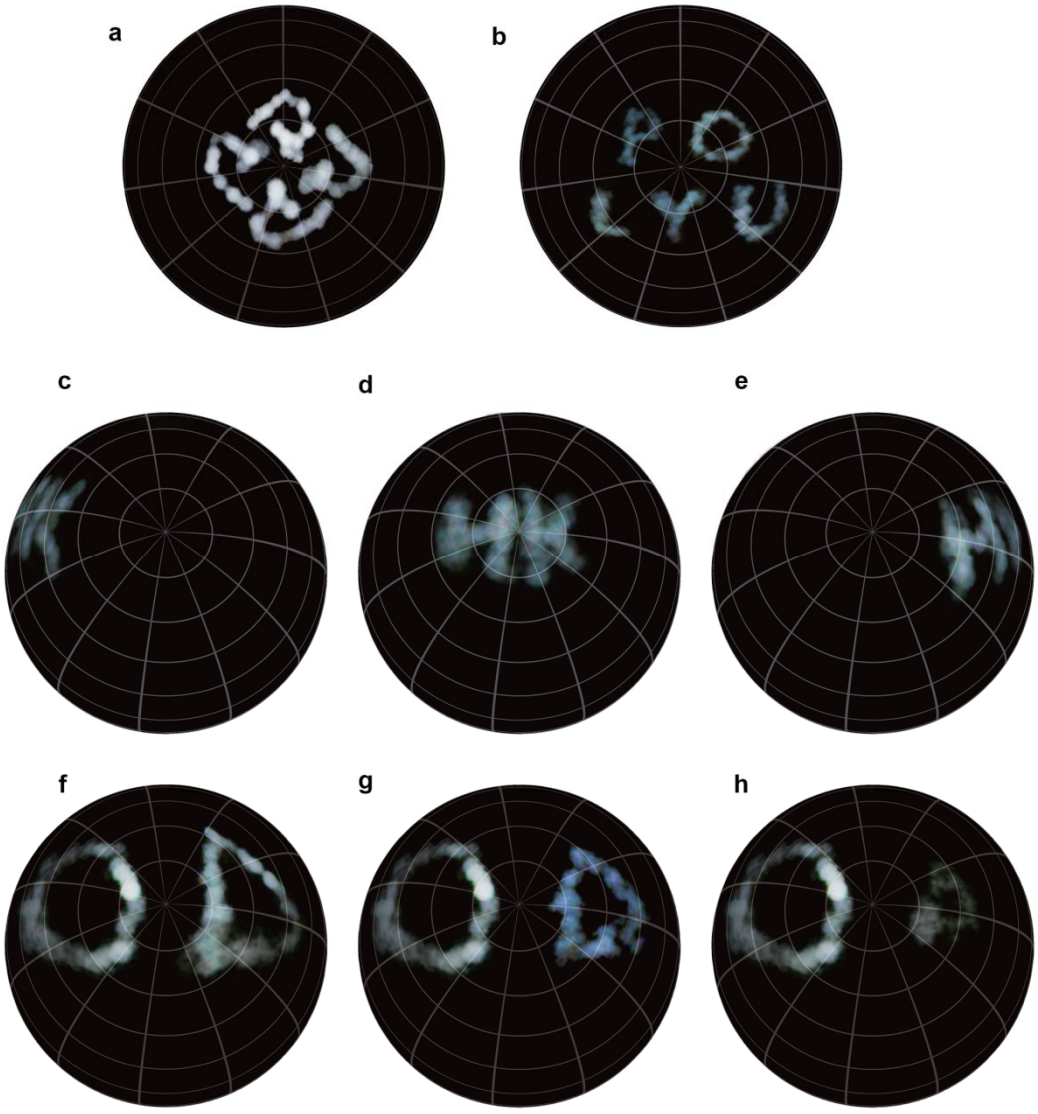

Figure 4-10. Static imaging results of different object patterns captured by the ACEcam. a, Logo of The Hong Kong Polytechnic University. **b,** The letters 'POLYU', the abbreviation of The Hong Kong Polytechnic University. **c-e,** The letters 'HK' captured at three different polar angles relative to the centre of the

camera: -50° (**c**), 0° (**d**), and 50° (**e**). **f-h,** Objects A (circle) and B (triangle) placed at angular positions of 40° and -40° with a fixed distance D_A and a varying distance D_B (from 2, 8 to 14 mm), respectively.

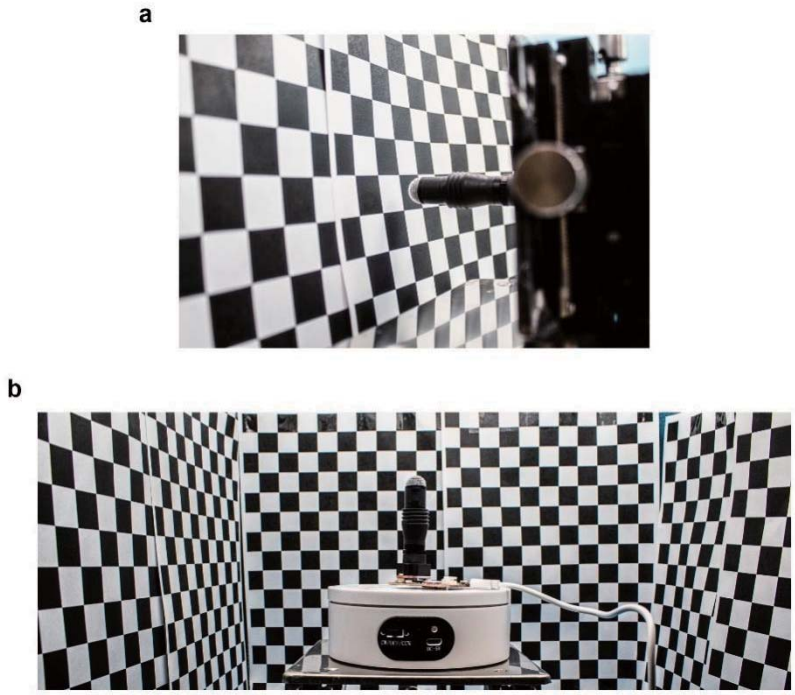

Figure 4-11. Setups for optical flow detection. a, The ACEcam is positioned 10 mm in front of a checkerboard pattern and translated. **b,** The ACEcam is rotated on a rotary stage.

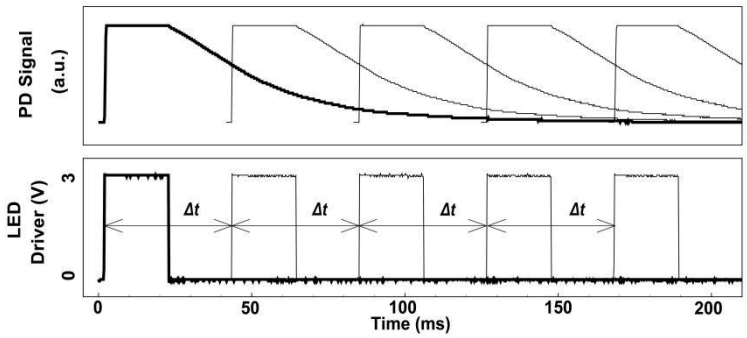

Figure 4-12. Dynamic angular perception results when $f_{flicker}$ = 24 Hz. The lower half shows the input signal to the LEDs, and the upper half shows the

signals recorded by the five photodiodes.

4.6 Summary

In the proposed ACEcam, conical microlensed plastic optical fibres are used as artificial ommatidia. By adding a conical microlens to the distal end of the fibre, the plastic optical fibre mimics the function of an ommatidium, collecting and transmitting light to the sensing unit. A bundle of lensed plastic optical fibres evenly distributed on a hemispherical surface is assembled to mimic NCEs, and the proposed ACEcam demonstrates excellent static imaging and dynamic motion detection capabilities. For example, a wide field of view (i.e., 180^{o}) enables the ACEcam to outperform the majority of ACEs, making it particularly well-suited for applications in areas such as surveillance; the real-time panoramic direct imaging without distortions eliminates the need for redundant post-processing methods, rendering the ACEcam more suitable for applications such as imaging and distance measurement among moving objects in real-world scenarios; a nearly infinite depth of field can enhance the sense of realism in augmented reality experiences, making it more niche in virtual reality and augmented reality compared to those lacking this property; translational and rotational motion perception capabilities and ultrafast angular motion detection (5.6×10^{6} deg/s at maximum) provide the ACEcam with the potential for kinestate tracking and motion state control across various machines, from common cars to high-speed aeroplanes and even spacecraft. The amalgamation of these merits also positions the ACEcam for niche applications. For instance, the 180^{o} field of view and ultrafast angular motion detection make ACEcam suitable for

integration into obstacle avoidance systems for high-speed unmanned aerial vehicles. This capability reduces the need for multiple obstacle avoidance lenses, consequently eliminating excess weight and size. The 180^{o} field of view and little size of ACEcam also let it suitable for endoscopy. Although the image resolution and size are limited by the number of artificial ommatidia, this ACEcam provides an overview of the imaging space, which is useful for complementing existing camera systems that observe regions of interest with high resolution to obtain fine details.

Chapter 5 Optic superposition artificial compound eyes for static and dynamic adaptive light perception

Natural optic superposition compound eyes catalyze circadian insects to adapt to distinct light levels with their exemplary anatomic structure, which elicits a blueprint for optic superposition artificial compound eyes (OSACE) to excel in static and dynamic perceptions under dissimilar illumination intensities. Most artificial compound eyes focused on emulating the apposition compound eyes due to the straightforwardness of simpler anatomic structure, limiting their functionality to daytime. The limited research focusing on OSACE is also subject to constraints intrinsic, such as low field of view, and coded illumination patterns training, and thus can not be regarded as completed OSACEs. In this chapter, we aim to faithfully mimic the adjustment in the anatomic structure and ganglia during the variable light intensities to enable OSACE to achieve static direct panoramic imaging devoid of distortions across nearly infinite depths of field, distance perception, dynamic motion capture, and rapid perception of angular motion. Conical microlensed plastic optical fibres are utilized to accurately mimic the anatomical structure of natural ommatidia again. Therefore, the assembled artificial ommatia can achieve a 180^{o} FOV for direct light perception. OSACE can further perform well under 1000 times varying light intensities by spatial and temporal adjustments in both hardware and software, such as focus mode switch, binning mode, Gaussian spatial summation, and

exposure time lengthening. Mimicry in archetypes and precise adjustment of anatomical structure and ganglia enables OSACE to fulfil the requirements of static and dynamic perception, synchronized with circadian rhythms. These striking biomimetic characteristics enable the interrogation of emerging applications such as surveillance and unmanned drones, medical imaging, autonomous driving, virtual reality, aeroplanes and even spacecraft.

5.1 Brief introduction

As a cornerstone, Robert Hooke's primitive investigation about a grey drone-fly's cornea provoked red-hot dissection in compound eyes [10]. Following that, Sigmund Exner classified natural compound eyes (NCEs) into apposition and superposition types based on the length of the crystalline tract underlying the crystalline cone [11]. Regarding the former, we have discussed a lot in Chapters 2 and 4. The apposition compound eye profits from a high spatial resolution, sacrificing its light sensitivity, which does not need to be high during the day. However, this is not in accord with the vision requirement for some nocturnal insects (e.g. moths), which are active in dim light. For those with optic superposition compound eyes, which is a sub-category of superposition NCEs, when the light is abundant, the anatomical structure of the NCEs is similar to the one of diurnal insects except for a longer crystalline tract including the crystalline cone clear zone. However, if the light level is subjected, some spatial and temporal approaches can improve the photo catch ability more than 100,000 times [53].

Most ACEs are accentuated mimicking apposition compound eyes due to

the ease of imitation. Emulation of optic superposition compound eyes undeniably heightens the challenge, as it necessitates not only the replication of anatomical structure but also the spatial and temporal approaches employed to enhance light sensitivity. Therefore, only a little research tried to mimic optic superposition compound eyes. For example, The Gabor superlens utilizing an array of Keplerian telescopes was promising to achieve the superposition, however, its FOV was subject to its natural planar structure [115],[116]. Like apposition ACEs, it was possible to enlarge the FOV of superposition ACEs by distributing a collection of gradient refractive index (GRIN) lenses along a curved surface [117]. However, GRIN lenses hindered by the complicated interplay of geometric relationships could only be dispatched along a curve on a 2D plane, thereby not realizing compelling 3D superposition compound eyes. Although the single-pixel computational imaging technology could reconstruct the 3D light information and finally assemble a 3D artificial superposition compound eye, a series of coded illumination patterns were inevitably required. Thus the real-time imaging could not be met [6]. Among these limitations, no ACEs realised panoramic real-time direct imaging, distance measurement, and dynamic detection under different light levels by changing their internal structures and data processing methods, just like optic superposition NCEs.

In this chapter, we propose the utilization of conical microlensed plastic optical fibres again to accurately mimic the anatomical structure of natural ommatidia. Therefore, the assembled artificial ommatia can achieve a 180^{o} FOV for light perception. Fundamentally, spatial and temporal adjustments in both hardware and software empower the Optic Superposition Artificial Compound Eye (OSACE) to achieve static direct panoramic imaging devoid of distortions

across nearly infinite depths of field, even amidst varying light intensities. Similarly, it enables the fulfilment of distance perception, dynamic motion capture, and rapid perception of angular motion under diverse light brightness. Practically, OSACE holds potential for diverse applications in fields such as autonomous driving, augmented reality, and unmanned aerial vehicles. Furthermore, it stands as a foundational element for the advancement of future ACE technologies.

5.2 Working principles

During daylight conditions, ample illumination allows for the projection of light from each facet lens into its corresponding rhabdom through the crystalline tract (Fig. 5-1a). The presence of pigment serves to avoid the crosstalk between neighbouring ommatidia. Consequently, the aperture angle μ, which dictates light transmission efficacy, is determined as $A/2f$, where A and f denote the aperture diameter and focal length of the facet lens, respectively [49],[54]. Subsequently, the signal from each rhabdom can be relayed to deeper brain regions (e.g., medulla and lobula) via synaptic connections within lamina cartridges.

Conversely, in dimly lit environments, conventional imaging methods face challenges. Nocturnal insects employ two strategies for vision enhancement. The first entails a spatial approach, wherein pigment migration between the crystalline cone and the clear zone facilitates light passage through the clear zone to reach the underlying rhabdom [51],[52] (Fig. 5-1b). Consequently, the effective aperture angle $\overline{\mu}$ is defined as $\overline{A}/2\overline{f}$, with $\overline{A}$ and $\overline{f}$ representing the effective aperture diameter and focal length, respectively [49],[54].

Furthermore, lateral neural connections characterized by a Gaussian spatial summation function among rhabdoms promote the integration of signal outputs into individual cells (Fig. 5-1b). The second method involves a temporal approach, where extended integration time enables NCEs to capture more photons, thereby enhancing imaging quality.

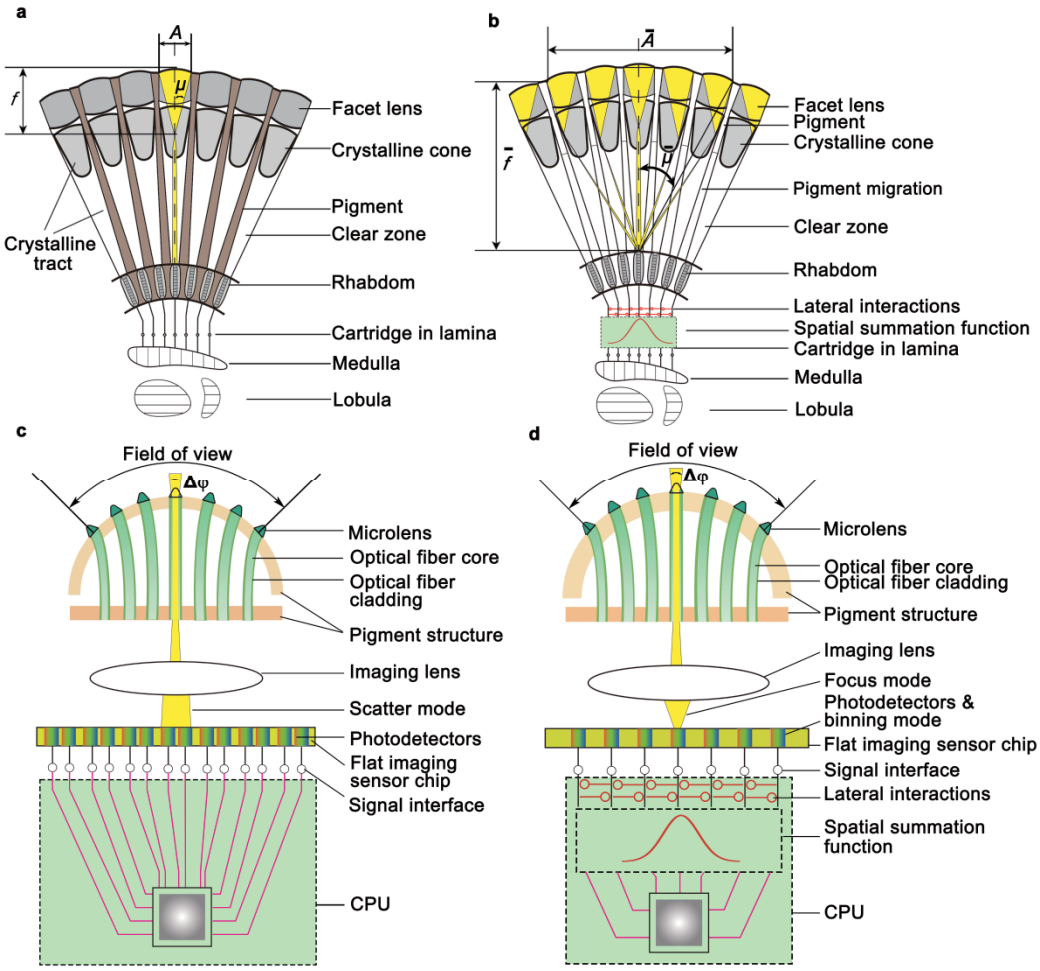

Figure 5-1. Concept and principle of the OSACE that uses lensed optical fibres to mimic natural counterparts. a, During the day, the facet lens with aperture angle μ, the aperture diameter A and focal length f focus light on the corresponding rhabdom through the long crystalline tract. Each rhabdom then transmits the signal to medulla and lobula through synaptic connections within lamina cartridges. **b,** At night, the pigment migration allows light from

neighbouring ommatidia to focus on one rhabdom with effective aperture angle $\overline{\mu}$, effective aperture diameter $\overline{A}$ and effective focal length $\overline{f}$. Lateral neural connections between rhabdoms facilitate Gaussian spatial summation of signal outputs. **c,** The OSACE effectively replicate natural structures during diurnal periods by employing a microlens to emulate facet lenses and crystalline cones, an optical fibre core to simulate the rhabdom, optical fibre cladding to mimic pigment cells, an imaging lens to replicate synaptic units facilitating signal transmission to deeper neural centres, a photodetector integrated into the flat imaging sensor chip to mimic photoreceptor cells, and a flat imaging sensor chip emulating deeper neural centres (medulla and lobula), where initial signal processing occurs. Subsequently, the signals are conveyed to the central processing unit (CPU) of a computer for advanced analysis. **d,** OSACE effectively emulates its natural counterparts at night by transitioning from scatter mode to focus mode and binning mode, mirroring the phenomenon of pigment migration, and facilitating lateral interactions among captured light spots on the planar imaging sensor chip to replicate the lateral neural connections.

Here, OSACE learns NCE's adaptation to varying light conditions. In bright environments, the imaging lens aids in scattering intense light (referred to as scatter mode) from each optical fibre to ensure slight overlap on the CMOS chip. Consequently, a significant portion of photodetectors on the CMOS chip can be activated, directly forming an image (Fig. 5-1c).

Conversely, in dim lighting, spatial and temporal approaches are employed to compensate for inadequate illumination. In the spatial approach, the imaging lens concentrates light onto specific photodetectors to enhance light intensity at

these locations (referred to as focus mode). Additionally, the binning mode is utilized to combine neighbouring pixels, further improving light intensity, akin to NCEs focusing light from neighbouring facet lenses onto a single rhabdom. However, merely activating isolated light spots on the CMOS chip does not yield a complete image. Drawing inspiration from NCEs, OSACE employs Gaussian spatial summation among these light spots to facilitate the formation of a complete image (Fig. 5-1d). In the temporal approach, a slight overlap is maintained (scatter mode). Similar to NCE behaviour, lengthening exposure time aids in recording more photons, thereby contributing to the formation of a clearer image.

5.3 Assembled device

Based on our analysis in Chapter 3, plastic optical fibres are a good choice due to their flexibility and durability. A conical microlens with a half-apex angle of θ = 35° helps to reduce the light acceptance angle of a plastic optical fibre from 60° to 45°. The tip of the conical microlens is rounded to avoid loss of acceptance area in the centre. A sequence of 3D printing, electroplating, and two moulding processes are proposed to fabricate the conical microlensed plastic optical fibres in batches (Fig. 5-2a).

In the assembly, 271 conical microlensed plastic optical fibres are fixed to a 3D-printed perforated dome with a diameter of 14 mm, positioning the lensed ends on the dome's surface (Fig. 5-2b). Bare fibre ends are inserted into a perforated flat buncher, directing light onto a flat imaging sensor via an imaging lens. The dome, buncher, imaging lens, and sensor chip are housed in a threaded

hollow tube (Fig. 5-2c). The lensed plastic fibres serve as optical guides to transmit light from the microlenses on the dome to the relative positions of the buncher plane. This setup facilitates the transmission of light collected from the curved surface to a flat image sensor (Fig. 5-2d), promising the ability to perceive static and dynamic light information under various lighting conditions.

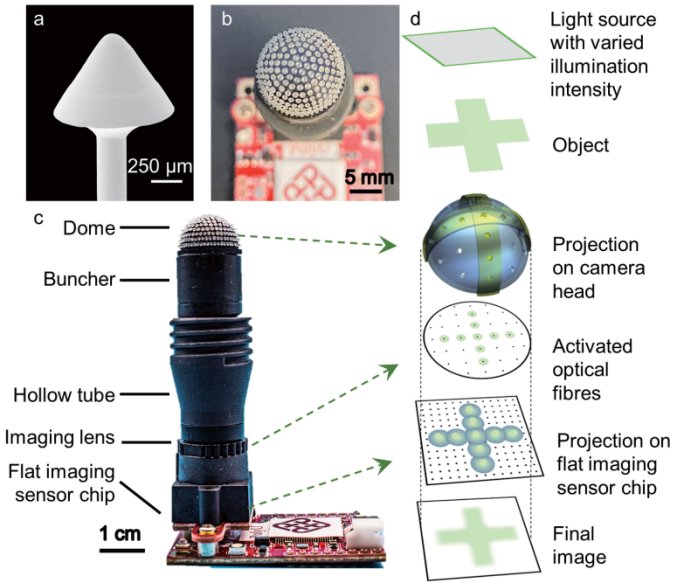

Figure 5-2. Operating principles of the OSACE. a, SEM image of the conical microlensed plastic optical fibre. **b,** Top view of the OSACE light receiving head with a 3D-printed dome to host 271 fibre lensed ends. **c,** Photograph of an assembled OSACE. **d,** Concept of image formation under hierarchical light levels. Using a '+' line-art object pattern (second panel) is illuminated by varied light intensities (top panel), certain fibres intercept light emitted by the object (third panel), subsequently transmitting this pattern from the lensed end to the opposite terminus of the fibre (fourth panel). In conditions of sufficient illumination, an imaging lens operating in scatter mode is utilized to project overlapping spots onto a flat imaging sensor chip (blue large spots in the fifth panel). Conversely, under low light conditions, the imaging lens switches to

focus mode, resulting in discrete light spots on the chip (green small spots in the fifth panel), which subsequently undergo lateral interactions. As a result, a final digital image can be generated across varying light intensities (bottom panel).

5.4 Results

Here, we evaluated the static and dynamic performance of OSACE under various lighting conditions. Initially, we confirmed OSACE's 180º FOV. Laser spots are illuminated within a range of 90° to 0° at intervals of 22.5° along both the *x* and *y* axes. Given the scatter mode of the imaging lens, the captured spots exhibit a high degree of uniformity in terms of size, brightness, and angular position, as depicted in the combined result (Fig. 5-3a) and individual images (Supplementary Fig. B-1). The expansive 180º FOV ensures a broader range of light information for both static and dynamic perception, and thus OSACE becomes more adaptable for diverse applications, including surveillance and unmanned drones.

5.4.1 Static characteristics

The second merit is its static direct imaging under different light conditions. A letter ‘F’ is placed at different distances (object distance) to test OSACE’s direct imaging ability at different object distances (red lines in Fig. 5-3b). When the light is quite adequate (about 100 Lux), the imaging results are quite clear (Fig. 5-3c and Supplementary Fig. B-2a). When the light becomes weaker, OSACE can still capture the object until its light intensity is down to about 10 Lux (Supplementary Figs. B-2b & B-3a for about 50 Lux, Supplementary Figs. B-2c

& B-3b for about 10 Lux). If the light intensity reduces to about 0.1 Lux, the low signal hiders OSACE to direct imaging. Just like what NCE does, we adopt both spatial and temporal approaches to solve this problem. For the spatial approach, the focus mode and the binning mode are chosen to improve local light intensity, mimicking the pigment migration of NCEs. In order to recover light spots to a full image, a Gaussian spatial summation among these light spots is added to the raw image (Fig. 5-3d and Supplementary Fig. B-2d, Appendix B.2) mimicking lateral neural connections of NCEs. For the temporal approach, we do not change the focus mode and binning mode. On the contrary, we change the exposure time to 75 ms, 150 ms, and 300 ms (Supplementary Figs. B-2e-g & B-3c-d, and Fig. 5-3e), with the clarity of raw images increasing dramatically.

To quantitatively assess the imaging performance under varying lighting conditions, we introduce the concept of information entropy (Appendix B.3). This metric characterizes the level of randomness or uncertainty present in an image, essentially reflecting the amount of information conveyed within the image [118]. Consequently, higher information entropy in Fig. 5-3f indicates a greater transmission of information, thus suggesting superior image quality. Low errors demonstrate the robustness of OSACE in capturing images under varying conditions. Additionally, under each light intensity, there remains a discernible downward trend in information entropy when object distance increases. Even at approximately 10 Lux light intensity, the diminishing trend of information entropy with increasing object distance remains apparent, signifying effective object capture under such illumination. However, at around 0.1 Lux light intensity, although the information entropy still diminishes with increasing object distance, both the extent of this change and the resulting information entropy

value are markedly low. Hence, a spatial or temporal approach becomes imperative to enhance image quality. As depicted in Fig. 5-3g, employing a spatial approach noticeably elevates information entropy under 0.1 Lux to a level comparable to that under 100 Lux. Furthermore, prolonging exposure time proves beneficial in augmenting information entropy, with a 600ms exposure time yielding information entropy levels comparable to those under 100 Lux. The capability of direct imaging under varying light intensities renders OSACE more apt for scenarios characterized by inconstant illumination levels, such as medical imaging.

The third merit is its distance perception (i.e., depth estimation) ability through captured images. The grey values along the vertical edge direction at various distances (illustrated by pink lines in Fig. 5-3b) are subject to analysis. For each condition, five lines are examined to derive the mean value and associated errors. This analytical endeavour aims to elucidate the correlation between the point spread parameter σ, derived from the edge grayscale gradient, and the reciprocal of the object distance u^{-1}, (Fig. 5-3h). Theoretically, this correlation is expected to exhibit a linear trend based on the research findings in Chapter 4. Notably, under conditions of high light intensity, the depth estimation sensitivity (indicated by the slope of lines) is proportionately high, leading to diminished distance estimation errors (Fig. 5-3h). Conversely, reduced light intensity results in diminished sensitivity and heightened errors. At approximately 0.1 Lux light intensity, direct calculation of the edge grayscale gradient becomes challenging due to the image consisting of light spots. Consequently, the ratio of edge pixels to the total number of non-zero pixels is employed as a surrogate measure for the edge grayscale gradient (Fig. 5-3i),

revealing a nearly linear association between this ratio (mean value and error computed from five repetitive experiments) and the reciprocal of the objective distance. Furthermore, adoption of a temporal approach to augment information entropy enables recalibration of σ for object distance estimation (Fig. 5-3j). This capability positions OSACE for specialized applications necessitating real-time object distance detection, such as autonomous driving.

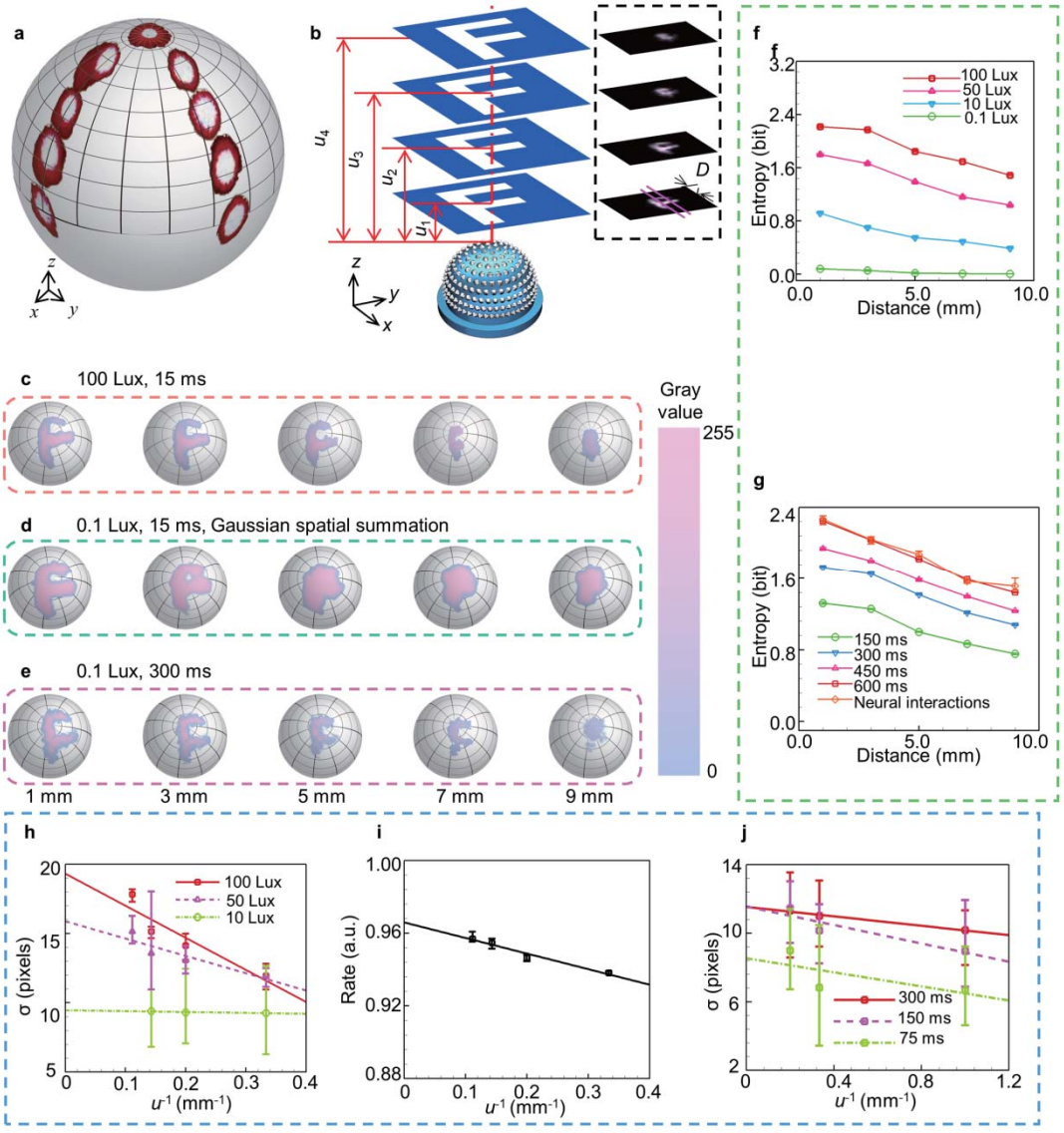

Figure 5-3. Static imaging and depth estimation of the OSACE. a, Combined image of a laser spot from nine angles captured from nine different angles, ranging from -90° to 90° in both the *x* and *y* directions, with an increment of

22.5°. **b,** Depth estimation relying on the linear correlation between the point spread parameter σ and the reciprocal of the object distance u^{-1}. Example images captured at four distinct distances u_1 = 3 mm, u_2 = 5 mm, u_2 = 7 mm, and u_4 = 9 are delineated within the dotted box. For each image obtained at these distances, grey values along five vertical edge direction lines (two example lines shown here in pink) in the *x*-direction undergo analysis to ascertain the mean value and associated errors, as depicted in **h** and **j**. D_L represents the distance between a point on the pink line and the upper boundary of the image. **c-e**, Images of the letter 'F' under different conditions. **f,** Information entropy of images captured under different light intensities. **g,** Information entropy of images employing spatial or temporal approaches at a light intensity of 0.1 Lux. For each condition in **f** and **g**, mean values and errors are computed based on 5 repetitive experiments. **h,** Relationship between the point spread parameter σ and the reciprocal of the object distance u^{-1} under different light intensities. **i,** Relationship between the ratio of edge pixels to the total number of non-zero pixels the reciprocal of the object distance u^{-1} at a light intensity of 0.1 Lux. **j,** Relationship between the point spread parameter σ and the reciprocal of the object distance u^{-1} under different exposure times at a light intensity of 0.1 Lux.

The fourth merit is its panoramic imaging without distortions under different light conditions. The letters 'HK' are positioned at three distinct angular orientations: -50°(left), 0° (centre), and 50° (right) under light intensities of approximately 100 Lux (Fig. 5-4a and Supplementary Fig. B-5a), 50 Lux (Supplementary Figs. B-4a & B-5b), and 10 Lux (Supplementary Figs. B-4b & B-5c). No image distortions are observed, demonstrating the effective panoramic

imaging performance of OSACE across varying light intensities. Similarly, when the light intensity is about 0.1 Lux, both spatial (Fig. 5-4b and Supplementary Fig. B-5d) and temporal (Fig. 5-4c and Supplementary Fig. B-5e) approaches are adopted to achieve panoramic imaging. The panoramic imaging capability across varying light conditions enables OSACE to discover diverse applications, including environmental monitoring.

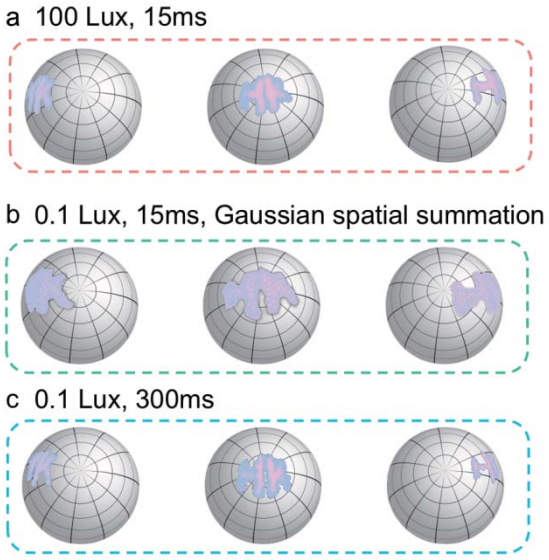

Figure 5-4. Panoramic imaging of the OSACE. a-c, Images of the letters 'HK' acquired at three distinct polar angles relative to the centre of the OSACE: -50° (left), 0° (centre), and 50° (right), under varying light intensities.

The fifth merit is its nearly infinite depth of field under different light conditions. To confirm this characteristic, for each light intensity, two objects, a circle and a triangle, are positioned at significantly spaced angles and varying distances (Fig. 5-5a). Given the light intensity is sufficient (approximately 100, 50, and 25 Lux), when the distances of both objects are equal, their respective image sizes appear similar (Fig. 5-5b, Supplementary Fig. B-4c&d, Supplementary Fig. B-5f-h, and Supplementary Video B-1). Additionally, when

the circle image remains stationary while the triangle image is moved away from OSACE, the size of the circle image remains constant, while that of the triangle image diminishes. When the light intensity is low, both mentioned spatial (Fig. 5-5c, Supplementary Fig. B-5i) and temporal (Fig. 5-5d, Supplementary Fig. B-5j) approaches are adopted to form the image. Notably, the focus is consistently maintained. The nearly infinite depth of field demonstrated by OSACE is ascribed to its image formation process, where each fibre captures all light information within its acceptance angle, irrespective of the object distance. When contrasted with ACEs lacking infinite depth of field [39], this attribute empowers OSACE to excel in specific domains, notably in virtual reality and augmented reality applications, where it facilitates heightened realism within augmented reality encounters.

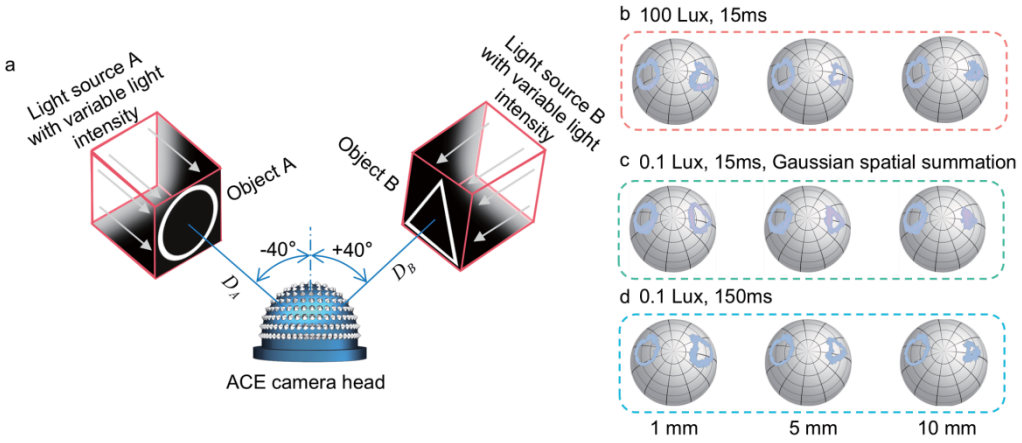

Figure 5-5. Nearly infinite depth of field of the OSACE. a, Diagram of an experimental configuration designed to validate the near-infinite depth of field capability of OSACE under hierarchical light intensities. Objects A (circle) and B (triangle) are positioned at angular orientations of -40° and 40° respectively. **b-d,** Images of the circle and triangle patterns captured with the circle image fixed at

a distance of D_A = 1 mm, while the distance of the triangle image shifts from D_B = 1, 5, to 10 mm, under various illumination intensities.

5.4.2 Dynamic characteristics

The sixth merit is its dynamic motion capture capability. Here, we placed OSACE on a slide affixed to a rail, allowing OSACE to move at a consistent speed, heading towards a standard checkerboard (Fig. 5-6a) under various light intensities (approximately 100 Lux, 50 Lux, and 10 Lux). For each light intensity, the optical flow is determined (Fig. 5-6b) using the conventional Lucas-Kanade method [112],[113] across 10 different velocities (ranging from 1mm/s to 10 mm/s), with each experiment conducted at least 3 times to obtain the mean measured speed value and associated errors (Supplementary Fig. B-6a-c). The resultant optical flow vectors exhibit homogeneous direction and length, underscoring the reliability and stability of OSACE in dynamic motion detection. The difference δv between the velocities derived from the fitted curves (e.g., the yellow point in Supplementary Fig. B-6b) and the theoretical velocities (Supplementary Fig. B-6d) can be computed. This difference, as illustrated in Fig. 5-6c, is found to be minimal, indicating excellent velocity estimation capability. OSACE's ability to detect dynamic motion opens the door to a range of applications, such as tracking kinestate and controlling motion in robots and unmanned aerial vehicles.

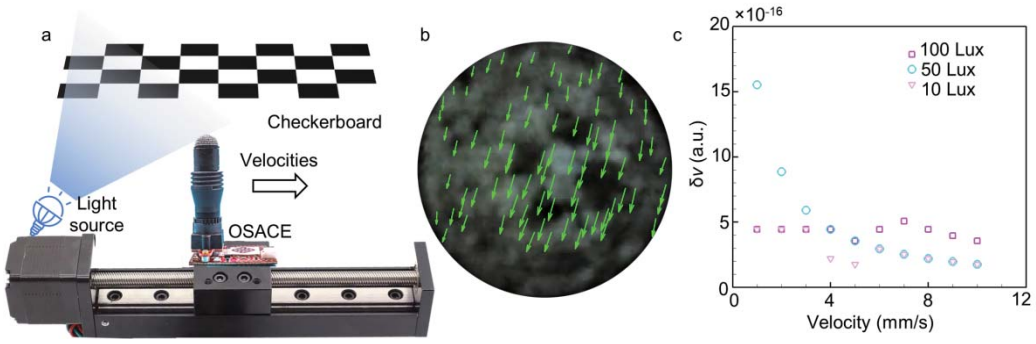

Figure 5-6. Dynamic motion detection of the OSACE. a, Diagram illustrating the positioning of the OSACE 10 mm in front of a checkerboard pattern, followed by its translation at different velocities under varying illumination intensities. **b,** Optical flow during OSACE translation in proximity to a checkerboard pattern at a distance of 10 mm. Herein, the white area is illuminated by bright squares of the checkerboard, while the black area corresponds to the dark squares of the checkboard. The direction and length of the vectors indicate the motion direction and velocity of a bright square. **c,** Differences between fitted velocities and true velocities under different illumination intensities.

The seventh advantage lies in the ultrafast perception of angular motion under varying background light intensities. To illustrate a basic object exhibiting rapid angular motion, Five LEDs are evenly spaced over 180^{o} and successively triggered by square wave signals with a period of Δt (Fig. 5-7a), while the background light intensity is varied (100 Lux, 50 Lux, 10 Lux, and 0 Lux). Utilizing a CMOS chip (OV7725, OmniVision Technologies Inc., 30 fps) as the photodetection unit results in a frame rate of 30 Hz. Consequently, when the flicker frequency exceeds 30 Hz, the absence of captured LED flickering can be observed (Supplementary Video B-2). Additionally, the angular perception is

limited to 5.4 × 10^3 deg/s (Appendix B.4.1). Subsequently, a photodiode array equipped with 5 electromagnetically shielded photodiodes (ElecFans) is employed (Fig. 5-7a), and the signal from flickering LEDs is preserved using these photodiodes. When the flicker frequency $f_{flicker}$ = 24 Hz approaches the human flicker fusion frequency (FFF) [3],[5], the photodiodes exhibit smooth response curves (Fig. 5-7c) under varied background light intensities. However, with the background light intensity increasing, the amplitude of the recorded signal decreases, meaning that the influence of the noise in the background on the signal increases. When $f_{flicker}$ = 240 Hz approaches the flicker fusion frequency (FFF) of the fly *Glossina morsitans* (FFF ≈ 205 Hz [4],[24]), and even at 2400 Hz, the photodiode signals still exhibit smoothness under varied background light intensities (Fig. 5-7d, Supplementary Fig. B-7a). To push the limits, the LEDs are configured to operate at $f_{flicker}$ = 25 kHz, aligning with the response time of the photodiodes used in this experiment (i.e., 40 μs) and surpassing the typical FFF of NCEs by approximately 100-fold. As a result, the electrical signals detected by the photodiodes shift from a square wave to a spike wave (Supplementary Fig. B-7b). Consequently, OSACE demonstrates the capability to respond to angular velocities of up to 4.5×10^6 deg/s (Appendix B.4.2, Supplementary Video B-3), a performance that can be further amplified by several orders of magnitude using faster photodiode arrays (e.g., 28 Gbit/s, PD20V4, Albis). To quantitatively evaluate the effect of background light, Contrast C = standard deviation / average value of recorded signals is adopted (Fig. 5-7b), where the standard deviation represents the variation range of the recorded LED signals, and the average value represents total recorded signals including recorded LED signals and background light signals. With the

frequency increasing, the decreased *C* is attributed to the decrease in standard deviation, meaning that the recorded effective LED signals decrease. When the frequency is low, the effect of the background light on *C* is obvious, while the frequency is high, the effect is not so obvious. Therefore, when OSACE is used to detect ultrafast angular motion, the effect of the background light can be ignored, while when it is used to detect a common speed motion, the effect of the background light should be noticed. This characteristic extends the scope of applications to include high-speed objects like aeroplanes and even spacecraft, a capability beyond the reach of typical ACEs.

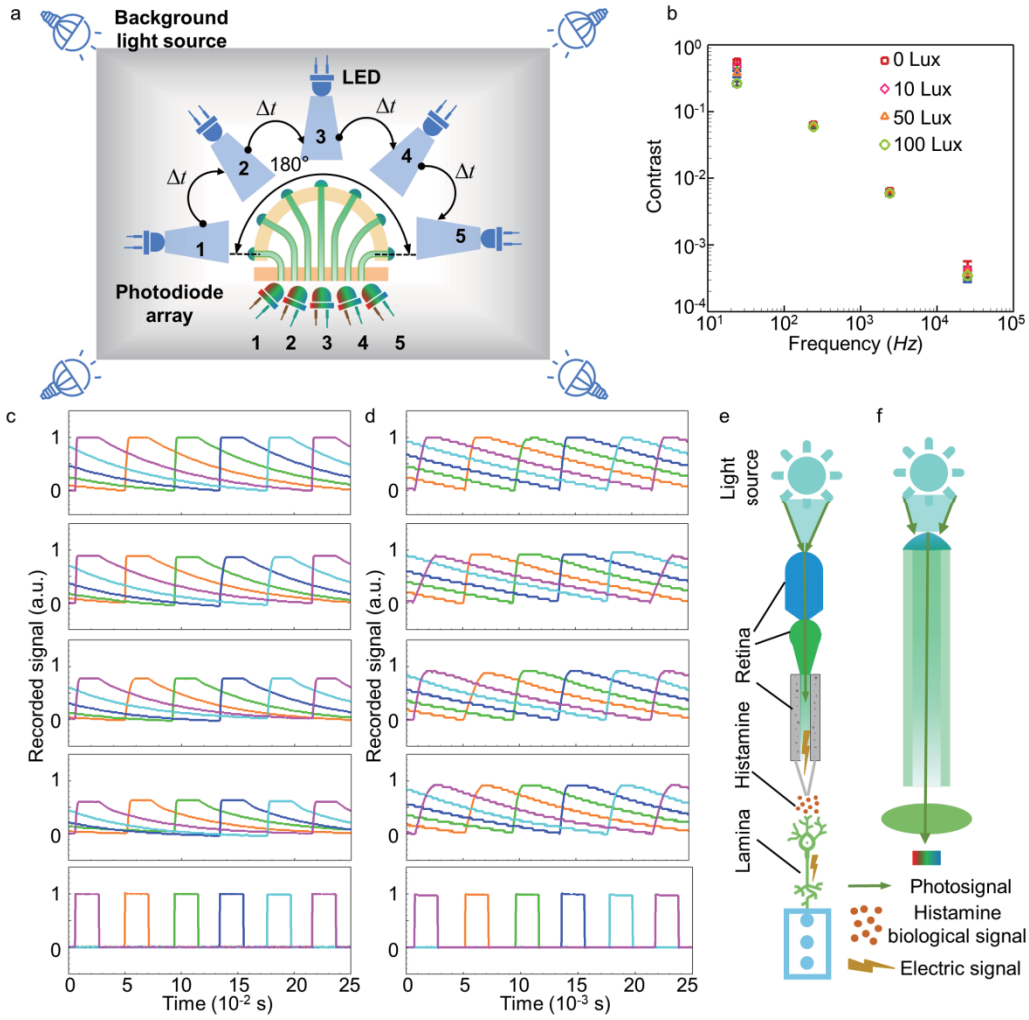

Figure 5-7. Ultrafast perception of angular motion of the OSACE. a, Experimental setup for generating very high angular velocities to perceive

angular motion under varied background light intensities. Under each background light intensity, five LEDs are evenly distributed along 180° and sequentially activated with a delay time Δt, with a minimum value equal to the response time of the photodiode Δt_{dec}. Five photodiodes are utilized to detect the light emanating from the corresponding LEDs. **b**, Relationship between the contrast, representing effective information variation among different background light intensities, and the flicker frequency. **c-d**, Response signals of the photodiodes under 0 Lux (top panel), 10 Lux (second panel from top), 50 Lux (third panel from top), and 100 Lux (fourth panel from top) when LEDs are activated by square waves (lowest panel) of $f_{flicker}$ = 24 Hz in **c** and $f_{flicker}$ = 240 Hz in **d**. **e,** Path of signal transmission within the natural ommatidium across varying light intensities. **f,** Path of signal transmission within the artificial ommatidium across varying light intensities.

The key factor driving OSACE's remarkable ultrafast angular motion perception is its emulation and surpassing of NCEs' signal transmission capabilities mentioned in Chapter 4 [14],[114]. Insects' nonspiking graded neurons enable a substantial boost in signal transmission rate between the retina and lamina neurons, surging from approximately 300 bit/s for spiking neurons found in humans to 1650 bit/s for nonspiking graded neurons [15]. Here, multiple signal conversion steps in natural ommatidium (e.g., photosignals-histamine biological signals-electric signals, Fig. 5-7e) can be further simplified to just one step, i.e. photosignals-electric signals in the artificial ommatidium (Fig. 5-7f), which helps to achieve a higher angular motion perception compared with NCE. More importantly, if photodiodes with higher frequency response,

which limits signal transmission, are utilized, a higher angular motion perception can be achieved, providing a roadmap for forwarding ACE development.

5.5 Summary

In this chapter, conical microlensed plastic optical fibres are distributed on a hemispherical surface to converge light from the curved surface to a plane. Essentially, learning from nocturnal insects, spatial and temporal approaches are adopted to adapt the hierarchical light intensities, which is firstly to faithfully mimic the transformation in optical superposition NCEs' structure and neuron. When light is dim, for the former, the scatter mode will be switched to focus mode and binning mode through controlling components such as the imaging lens, and a Gaussian spatial summation among light spots in an image further helps to form an entire image, mimicking the Gaussian spatial summation among NCE's rhabdoms. For the latter, a longer exposure time mimicking a longer integration time in NCE helps to form a clear image. These adjustments in hardware and software of OSACE replicate the pigment migration and connection between neuronal synapsis of superposition NCE, achieving static and dynamic perception under 1000 times varying illumination intensities, and thus find numerous niche applications. For example, the 180^{o} FOV helps OSACE to excel in surveillance and unmanned drones, the static direct imaging makes it suitable for scenarios such as medical imaging, the depth estimation ability makes it apt for autonomous driving, the panoramic imaging without distortions shows the possibility in applications including environmental monitoring, the nearly infinite depth of field facilitates heightened realism in

virtual reality and augmented reality, the dynamic motion capture capability opens the door to tracking kinestate and controlling motion in robots and unmanned aerial vehicles, and the ultrafast perception of angular motion extends the scope of applications to include high-speed objects like aeroplanes and even spacecraft. More importantly, combining these characteristics under varying light conditions would find more applications. For example, the combination of 180° FOV, panoramic direct imaging, depth estimation ability, and ultrafast dynamic detection shows its superiority in robots, and unmanned aerial vehicles, eliminating excess weight and size. Besides, OSACE shows a blueprint for further ACEs mimicking superposition NCEs to further improve the resolution under varied illumination intensities.

Chapter 6 Conclusions and Future Work

6.1 Conclusions

In this thesis, we demonstrate a novel artificial ommatidium and fibre based apposition and optic superposition artificial compound eyes (ACEs). Natural compound eyes (NCEs) have inspired researchers to develop a kind of biomimetic imaging device: ACEs. However, few ACEs have faithfully replicated the complex anatomical structure of NCEs, thus failing to achieve both static imaging and dynamic motion detection as NCEs do. Here, we have developed conical microlensed plastic optical fibres to function as artificial ommatidia by emulatinig natural ones. These specialized fibres enable the apposition and optic superposition ACEs to function similarly to NCEs in various scenarios. Due to their superior performance, these ACEs have the potential for diverse applications, including surveillance, unmanned drones, and virtual reality. Furthermore, unlike standard cameras, which are limited to observing objects within their focal plane, artificial compound eyes (ACEs) developed in this thesis offer a nearly infinite depth of field, enabling observation of objects at varying depths simultaneously. Moreover, ACEs provide a significantly wider field of view compared to standard cameras, making them highly suitable for achieving 3D vision across a broader perspective. In comparison to light detection and ranging (LiDAR) technology , which requires a scanning mechanism to achieve a wide field of view, ACEs can simultaneously observe objects at different angles, offering a distinct advantage.

In the first part, we have theoretically analyzed the optical paths of plastic optical fibers and fabricated conical microlensed plastic optical fibers that function as artificial ommatidia. Plastic optical fibres are chosen in applications of ACEs due to their flexibility and durability compared to silica fibres. Theoretical optical path analysis of a bare plastic optical fibre, a plastic optical fibre with a spherical microlens, and a plastic optical fibre capped with a conical microlens is conducted. This analysis reveals that a conical microlens with a 35° half-apex angle and a rounded tip can reduce the acceptance angle of plastic optical fibres from 60° to about 45° to effectively reduce the angular overlapping. Optical tracing simulations are performed to verify the theoretical optical path analysis of the conical microlens. A unique batch fabrication technique for these conical microlensed plastic optical fibres is developed using 3D printing, electroplating, and moulding processes.

In the second part, optical fibre based apposition artificial compound eyes for direct static imaging and ultrafast motion detection has been introduced. An apposition ACE is assembled using 271 of these conical microlensed plastic optical fibres and characterized. The microlens mimics the facet lens and crystalline cone of NCEs, the optical fibre core mimics the rhabdom, and the optical fibre cladding mimics the pigment cells. An imaging lens focuses each optical fibre onto an individual photodetector, mimicking the synaptic units. This assembled ACE obtains a 180° field of view, enabling real-time panoramic direct imaging without distortions across a nearly infinite depth of field. It can perceive translational and rotational motion, and detect ultrafast angular motion up to 5.6 $\times 10^6$ deg/s, about 100 times faster than the response speed of dragonflies, the best in nature.

In the third part, optic superposition artificial compound eyes for static and dynamic adaptive light perception has been demonstrated. This ACE is assembled with conical microlensed plastic optical fibres again. Spatial and temporal approaches are implemented to enhance the ACE's ability to perceive static and dynamic adaptive light information. In the spatial approach, when light levels are low, the imaging lens switches from scatter mode to focus mode, and the flat imaging sensor chip transitions to binning mode to increase the image brightness. Additionally, Gaussian spatial summation among light spots in an image contributes to an entire image. Meanwhile, in the temporal approach, prolonging the exposure time aids in capturing an image with adequate effective light information. The mimicry of archetypes and precise adjustment of anatomical structure and ganglia enable the optic superposition ACE to meet the requirements for both static and dynamic perception under adaptive light intensities.

6.2 Future work

Although ACEs in this thesis effectively achieve both static imaging and dynamic motion detection, there are still three tips for further development:

(1) Further extend the field of view. By leveraging the flexibility of plastic optical fibres, the distal ends of the fibres distributed on the dome structure can be bent. This adjustment would allow for an even wider field of view, enhancing the overall performance of the system.

(2) Further decrease the acceptance angle of plastic optical fibres to increase the angular resolution. Apertures at the distal end of optical fibres could

be used in the future to replace the microlens. By considering the relationship among diameter, thickness, and distance of these apertures from the optical fibre, a further reduction in the acceptance angle could be anticipated.

(3) Further improve the resolution. Here are also two specific approaches to improve the resolution. **a,** Narrower optical fibres or light guides: Plastic optical fibres with smaller diameters (e.g., from currently 250 μm to 25 μm) can be used to reduce the space occupied by each fibre and thus increase the number of plastic optical fibres. Additionally, advanced fabrication technologies and devices with better critical dimension capabilities (e.g., nanoArch S130, BMF Precision Tech Inc.) can be employed to create domes and bunchers with more through-holes. This would allow for a greater number of narrow plastic optical fibres, thereby enhancing the image resolution. Alternatively, if it is a challenge to integrate a high density of optical fibres, liquid light guides, which can be cured, can be developed. Specifically, a liquid suspension capable of temporarily solidifying in the air will be used as the light guide cladding, while a UV-curable liquid glue will form the light guide core. This innovative approach would eliminate the need for dense fibre integration, overcoming existing limitations while preserving optical performance. **b,** Optical fibre bundles: Plastic optical fibres can be replaced with imaging optical fibre bundles to mimic optical and neural superposition in NCEs. Since each imaging optical fibre bundle contains thousands of individual fibres, the resolution can be significantly increased if the relationship between the microlens and the imaging optical fibre bundles is well analysed, similar to the analysis presented in this article.

Moreover, the combination of optofluidic lenses and ACEcam offers the potential to harness both benefits found in both arthropods' compound eyes and

vertebrate monocular eyes.

Appendix

Appendix A: Supplementary information for the apposition compound eye

Appendix A.1 Supplementary information: Supplementary figures

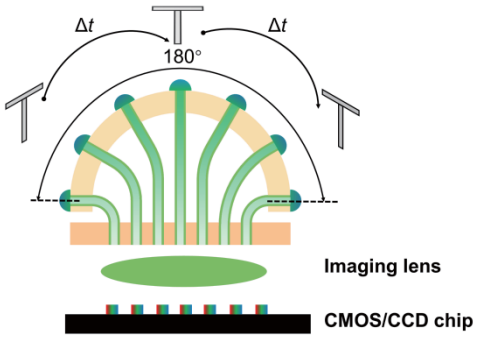

Supplementary Figure A-1. Experimental setup to generate high angular velocities for the dynamic response measurement. Three objects 'T' are evenly spaced along 180° and lit up successively with a delay time Δ*t*, and a CMOS chip is employed to record the patterns.

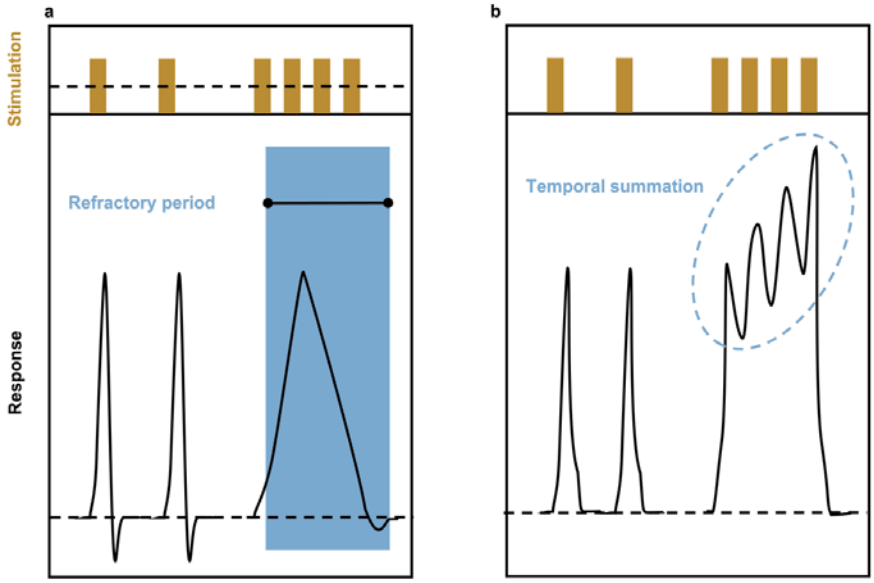

Supplementary Figure A-2. Response characteristics of spiking neurons (a)

and nonspiking graded neurons (b). a, In spiking neurons, an action potential can be triggered by strong stimulation. Then, the neuron enters a refractory period, during which it does not respond to stimulation. **b,** In nonspiking graded neurons, sequential stimulation leads to nonlinear temporal summed responses.

Appendix A.2 Supplementary information: The critical parameter *m* of a camera

The focusing property of the imaging lens used in ACEcam can be evaluated using geometrical optics. As shown in Supplementary Fig. A-3, the point p is the image position of the object point P. However, if p is not in the focal plane, a defocused, blurred circle appears in the detector plane, where p' denotes the centre of the blurred circle. Based on the geometrical analysis, the relationship among the blurred circle's diameter d_2, the lens diameter D, the distance from the lens to the focal plane s, the focal length f, and the object distance u can be expressed as

$$d_2 = Ds\left(\frac{1}{f} - \frac{1}{u} - \frac{1}{s}\right). \quad \text{(A-1)}$$

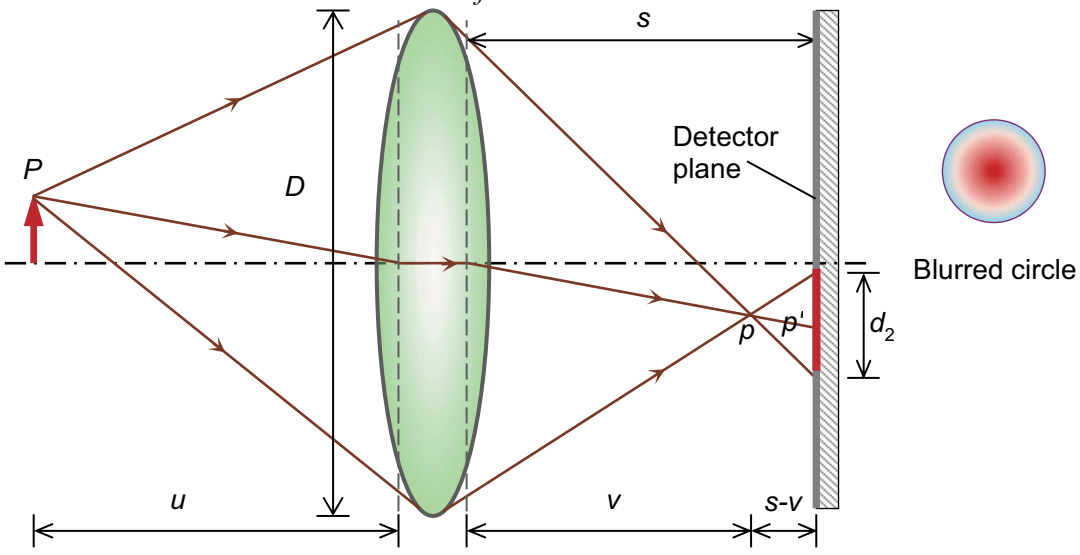

Supplementary Figure A-3. Imaging property of a lens using geometrical

optics. Here, p is the image point of the object point P, p' is the centre point of the blurred circle in the detector plane, and d_2 is the diameter of the blurred circle. The variables D, u, v and s denote the lens diameter, object distance, image distance, and distance between the lens and detector plane, respectively.

Due to the diffraction and the nonideal properties of lenses [119],[120], the intensity distribution $h(x, y)$ of the blurred circle follows a two-dimensional Gaussian distribution,

$$h(x,y)=\frac{1}{2\pi\sigma^2}e^{-\frac{x^2+y^2}{2\sigma^2}}, \tag{A-2}$$

where σ is the spread parameter, which has a linear relationship with d_2 (k is a constant):

$$\sigma = kd_2, \text{ here } k>0. \tag{A-3}$$

In fact, $h(x, y)$ is the point spread function of this camera, as discussed below. We can combine Eqs. (A-1) and (A-3) to formulate the relationship between the spread parameter σ and the object distance u:

$$\sigma = kDs\left(\frac{1}{f}-\frac{1}{u}-\frac{1}{s}\right). \tag{A-4}$$

For the camera used in our setup, the variables k, D, s and f are fixed camera parameters. Thus, Eq. (A-4) can be simplified as

$$\sigma = mu^{-1}+c, \tag{A-5}$$

where m and c are constants.

To determine the values of m and c using linear fitting, the values of σ and u under several different conditions should be measured. We first consider how to measure σ.

We introduce a step edge function along the *y* direction in the image plane *f*(*x*, *y*), which can be formulated as

$$f(x,y) = a + bu(x), \tag{A-6}$$

where *a* is the initial intensity, *b* is the height of the step, and *u*(*x*) is the standard unit step function. The observed image *g*(*x*, *y*) is then the convolution of *f*(*x*, *y*) and the point spread function *h*(*x*, *y*):

$$g(x,y) = f(x,y) * h(x,y), \tag{A-7}$$

where * represents the convolution operation. The derivative of *g* along the gradient direction can be written as

$$\frac{\partial g}{\partial x} = h(x,y) * \frac{\partial f}{\partial x} = h(x,y) * b\delta(x), \tag{A-8}$$

where $\delta(x)$ is the derivative of $u(x)$ along the x direction, which has the form of a Dirac delta function. This expression can be written as

$$\begin{aligned} \frac{\partial g}{\partial x} &= \int_{-\infty}^{\infty}\int_{-\infty}^{\infty} h(\varepsilon,\eta) b\delta(x-\varepsilon)\, d\varepsilon d\eta \\ &= \int_{-\infty}^{\infty}\left[\int_{-\infty}^{\infty} h(\varepsilon,\eta) b\delta(x-\varepsilon)\, d\varepsilon\right] d\eta = b\int_{-\infty}^{\infty} h(x,\eta)\, d\eta \end{aligned}. \tag{A-9}$$

$\theta_2(x)$, which is also called the line spread function, can be used to represent this line integral:

$$\theta_2(x) = \int_{-\infty}^{\infty} h(x,y)\, dy. \tag{A-10}$$

Then, Eq. (A-9) can be written as

$$\frac{\partial g}{\partial x} = b\theta_2. \tag{4-11}$$

The integration of this equation along the x direction is

$$\int_{-\infty}^{\infty} \frac{\partial g}{\partial x} dx = \int_{-\infty}^{\infty} b\theta_2 dx = b\int_{-\infty}^{\infty}\int_{-\infty}^{\infty} h(x,y)\, dx dy. \tag{A-12}$$

The integral of the point spread function should be unity, i.e.,

$$\int_{-\infty}^{\infty}\int_{-\infty}^{\infty} h(x,y)dxdy = 1. \tag{A-13}$$

Therefore, we have

$$\int_{-\infty}^{\infty} \frac{\partial g}{\partial x} dx = b. \tag{A-14}$$

Thus, $\theta_2(x)$ can be expressed as

$$\theta_2(x) = \frac{\frac{\partial g}{\partial x}}{\int_{-\infty}^{\infty} \frac{\partial g}{\partial x} dx}. \tag{A-15}$$

Since the point spread parameter σ of a line spread function [110] is the standard deviation of the line spread function $\theta_2(x)$, we have

$$\sigma = \sqrt{\int_{-\infty}^{\infty} (x-\bar{x})^2 \theta_2(x) dx}, \tag{A-16}$$

where $\bar{x}$ represents the average of the line spread function. Thus, it follows that

$$\bar{x} = \int_{-\infty}^{\infty} x\theta_2(x)dx. \tag{A-17}$$

If the greyscale gradient $\frac{\partial g}{\partial x}$ at the edge of an observed image is obtained, the line spread function $\theta_2(x)$ can be determined. Then, the average $\bar{x}$ and the point spread parameter σ can be obtained. Therefore, the point spread parameter σ indirectly represents the gradient at the edge. If several values of the point spread parameter σ and the object distance u are given, the values of m and c can be determined using Eq. (A-5). More importantly, m is the slope of the relationship between σ and u^{-1} and thus represents the extent to which a camera's

imaging quality (characterized by the gradient at the edge) is affected by a change in the object distance. In this work, this parameter *m* is defined innovatively as the *critical parameter*.

Appendix A.3 Supplementary information: Principle of the Lucas-Kanade method

In this work, we assume that the grey invariant hypothesis is valid, that is, that a pixel's grey value at a spatial site remains fixed in each image [112],[113].

The pixel at (x, y) at time t changes its position to ($x+dx$, $y+dy$) at time ($t+dt$). Based on our initial assumption, the grey value I should follow

$$I(x+dx, y+dy, t+dt) = I(x, y, t)\,. \tag{A-18}$$

When the left side of the above equation is Taylor expanded, we obtain

$$I(x+dx, y+dy, t+dt) \approx I(x, y, t) + \frac{\partial I}{\partial x}dx + \frac{\partial I}{\partial y}dy + \frac{\partial I}{\partial t}dt\,. \tag{A-19}$$

The combination of Eqs. (A-18) and (A-19) yields

$$\frac{\partial I}{\partial x}dx + \frac{\partial I}{\partial y}dy + \frac{\partial I}{\partial t}dt = 0\,. \tag{A-20}$$

The above expression can be rewritten as

$$\frac{\partial I}{\partial x}dx + \frac{\partial I}{\partial y}dy = -\frac{\partial I}{\partial t}dt\,. \tag{A-21}$$

Here, we use some variables to simplify the equation,

$$\frac{dx}{dt} = u_2,\ \frac{dy}{dt} = v_2,\ \frac{\partial I}{\partial x} = I_x,\ \frac{\partial I}{\partial y} = I_y\,. \tag{A-22}$$

Then, the equation can be written in matrix form as follows:

$$\begin{bmatrix} I_x & I_y \end{bmatrix} \begin{bmatrix} u_2 \\ v_2 \end{bmatrix} = -I_t\,. \tag{A-23}$$

As there are two variants, u_2 and v_2, a single point is insufficient for calculating their values. To address this issue, a calculation pixel window with a size of $w \times w$ is established. To calculate the variants, we assume that the pixels in the same window follow the same motion. Consequently, each window contains w^2 pixels, resulting in w^2 functions. The equation can then be expressed in matrix form as follows:

$$\begin{bmatrix} I_x & I_y \end{bmatrix}_k \begin{bmatrix} u_2 \\ v_2 \end{bmatrix} = -I_{tk}, \text{ here } k = 1, \ ..., \ w^2 . \tag{A-24}$$

Let

$$A = \begin{bmatrix} \begin{bmatrix} I_x & I_y \end{bmatrix}_1 \\ . \\ . \\ . \\ \begin{bmatrix} I_x & I_y \end{bmatrix}_{\omega^2} \end{bmatrix}, \ w = \begin{bmatrix} u_2 \\ v_2 \end{bmatrix}, \ b_2 = \begin{bmatrix} I_{t1} \\ . \\ . \\ . \\ I_{t\omega^2} \end{bmatrix}. \tag{A-25}$$

Then, the above equation becomes

$$Aw = -b_2 . \tag{A-26}$$

This is an overdetermined linear equation, and the least square method is adopted as follows:

$$\widehat{w} = -\begin{bmatrix} A^T & A \end{bmatrix}^{-1} A^T b_2 . \tag{A-27}$$

With this approach, the optical flow u_2 and v_2 in a window can be computed, and after calculating the values for all windows in an image, the overall optical flow can finally be obtained.

Appendix A.4 Supplementary videos

Supplementary Video A-1: ACEcam detects two objects that are placed at

angular positions of 40° and -40° with a fixed distance D_A or a varying distance D_B. When the distances of both objects are the same, the image sizes are identical. As D_B increases, the size of object B decreases (00:03 - 00:18); in contrast, as D_B decreases, the size of object B increases (00:22 - 00:33). Although the image size of the object varies with the change in distance, the focus is always retained.

Supplementary Video A-2: Dynamic angular perception experiment using a conventional CMOS imaging chip as the photodetector. Five sequentially illuminated LEDs are evenly arranged over 180° to mimic an object with high angular velocity. The CMOS chip has a frame rate of 30 Hz, corresponding to an angular velocity of 5.4×10^3 deg/s.

Supplementary Video A-3: Dynamic angular perception experiment on actual objects. Three objects 'T' are evenly arranged over 180° to mimic an object with high angular velocity. The CMOS chip is employed for object recording; however, at high flicker frequencies, there is a tendency for certain objects to be missed during recording.

Supplementary Video A-4: Dynamic angular perception experiments using a photodiode array that consists of 5 electromagnetically shielded photodiodes. The light emitted by flicker LEDs (representing a moving object) is recorded by the photodiodes. The number beneath each sub-video corresponds to the depicted photodiode in the right corner, recording the signal

emitted by the corresponding LED. The highest detection frequency is 31.3 kHz, corresponding to an angular velocity of 5.6×10^6 deg/s.

Appendix B: Supplementary information for the optic superposition compound eye

Appendix B.1 Supplementary information: Supplementary figures

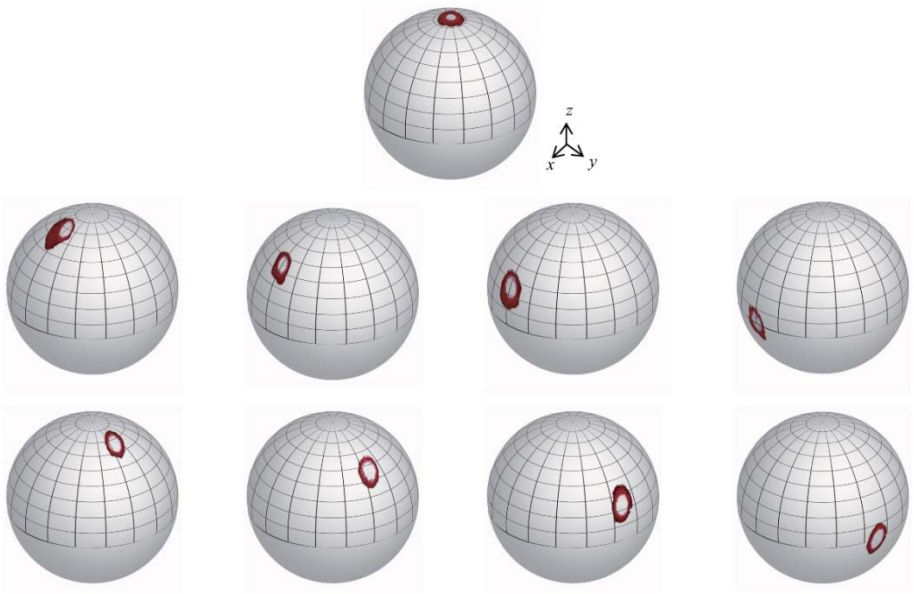

Supplementary Figure B-1. Visualization of laser spots projected onto the OSACE. These images are captured at 9 distinct incident angles (ranging from 0° to 90° in both the *x* and *y* directions, with increments of 22.5°). The visualization is presented on a hemispherical surface for enhanced clarity.

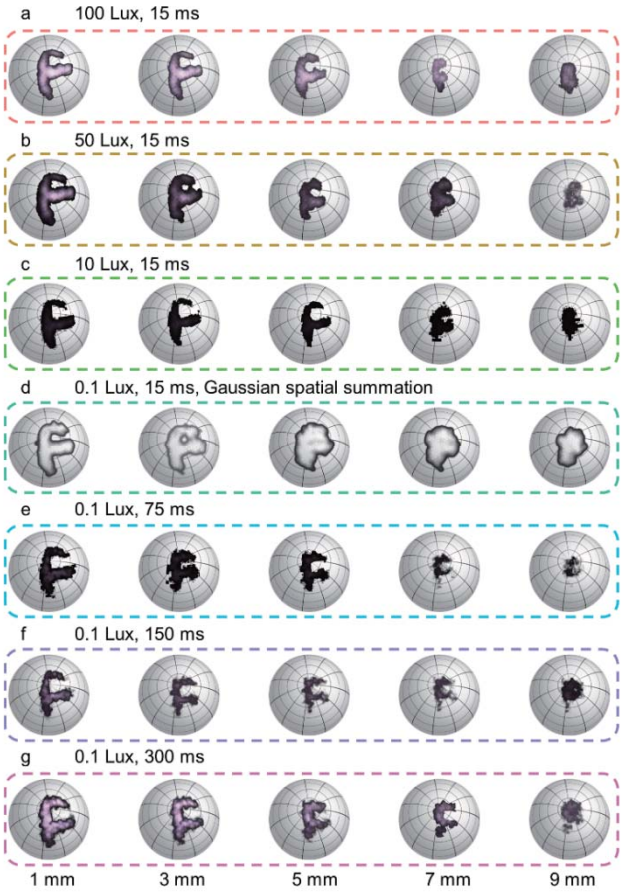

Supplementary Figure B-2. Original static imaging results of letter 'F' captured by the OSACE under different illumination intensities.

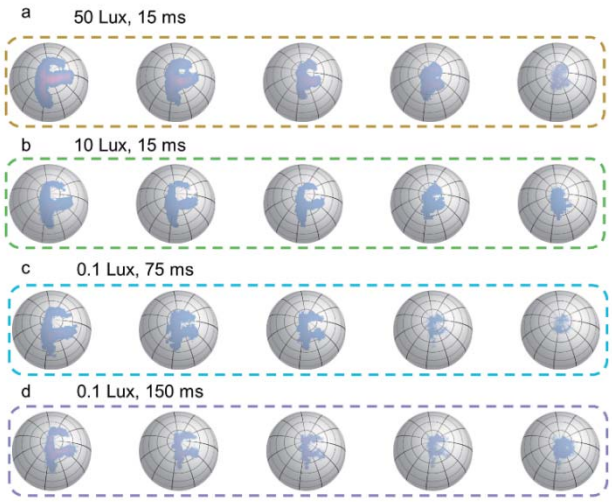

Supplementary Figure B-3. Static imaging of the letter 'F' under different conditions.

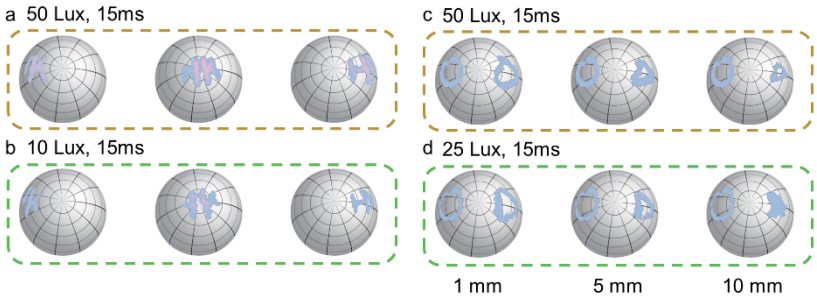

Supplementary Figure B-4. Panoramic imaging and nearly infinite depth of field of the OSACE. a-b, Images of the letters 'HK' acquired at three distinct polar angles relative to the centre of the OSACE: -50° (left), 0° (centre), and 50° (right), under varying light intensities. **c-d,** Images of the circle and triangle patterns captured with the circle image fixed at a distance of D_A = 1 mm, while the distance of the triangle image shifts from D_B = 1, 5, to 10 mm, under different illumination intensities.

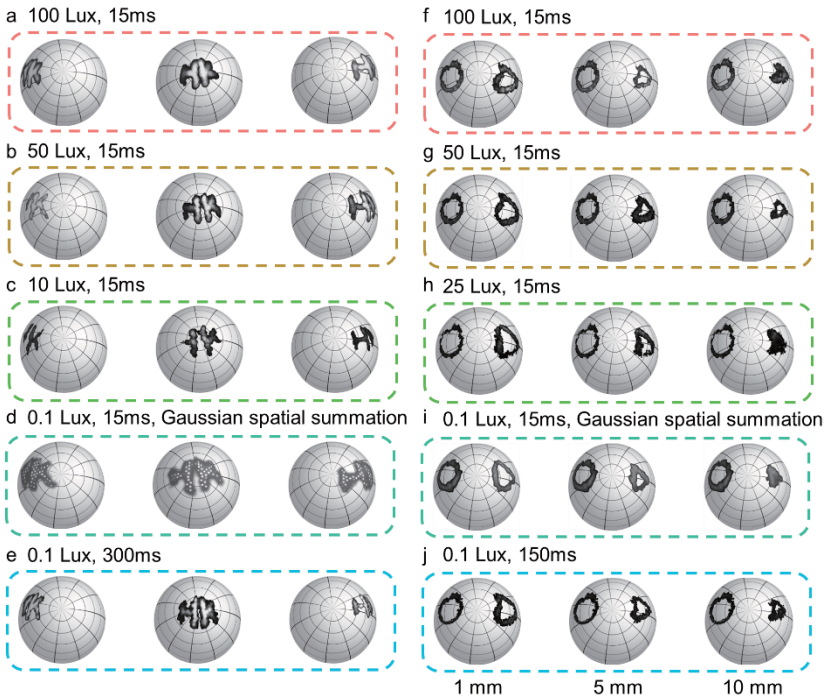

Supplementary Figure B-5. Original static imaging results of various object patterns captured by the OSACE under different illumination intensities. a-

e, The letters 'HK' acquired at three distinct polar angles relative to the centre of the OSACE: -50° (left), 0° (centre), and 50° (right), under varying light intensities. **f-j,** Objects A (circle) and B (triangle) positioned at angular orientations of 40° and -40° respectively, with a constant distance D_A and a shifting distance D_B (from 1, 5 to 10 mm), under different illumination intensities.

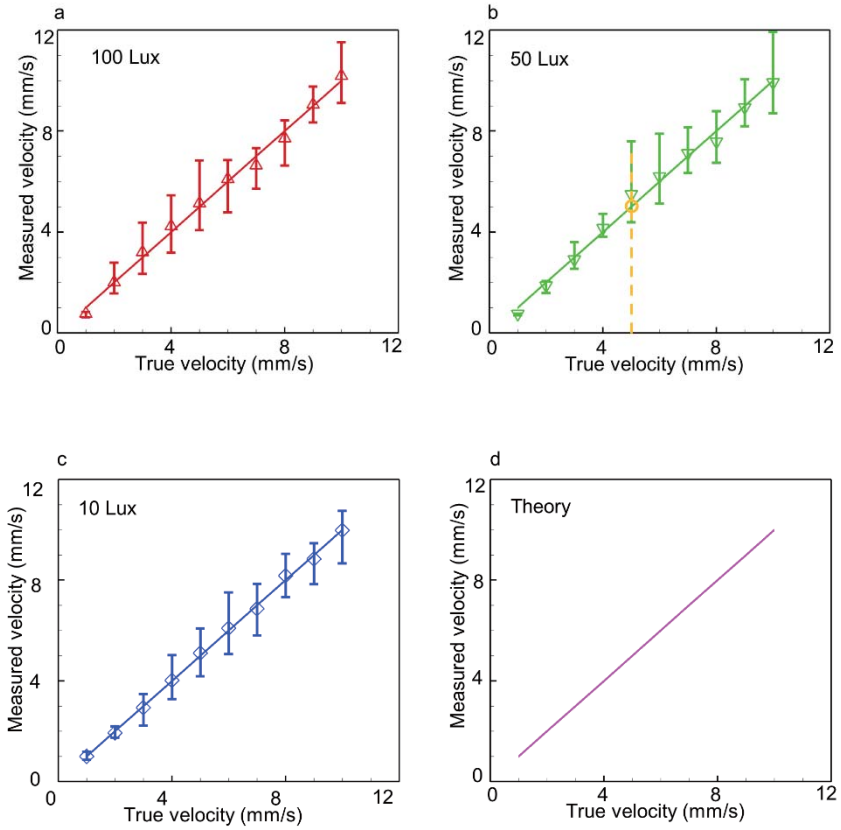

Supplementary Figure B-6. Relationships between measured velocities and true velocities under different light intensities. a-c, The light intensities are 100 Lux (a), 50 Lux (b), and 10 Lux (c), respectively. Optical flow is employed to compute velocities, which subsequently undergo a correction process prior to curve fitting for each light intensity condition. The yellow point on **b** denotes an exemplar point extracted from the fitted curve for assessing the disparity

between fitted velocities and true velocities. **d,** Theory relationship between measured velocities and true velocities.

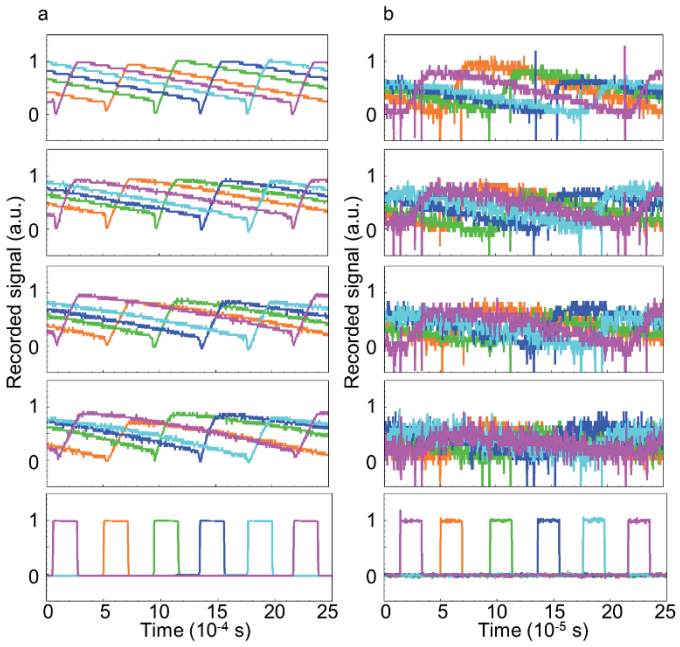

Supplementary Figure B-7. Response signals of the photodiodes. When LEDs are activated by square waves (lowest panel) of $f_{flicker}$ = 2400 Hz in **a** and $f_{flicker}$ = 25 kHz in **b**, response signals are recorded under 0 Lux (top panel), 10 Lux (second panel from top), 50 Lux (third panel from top), and 100 Lux (fourth panel from top) respectively.

Appendix B.2 Supplementary information: Gaussian spatial summation

For a 2D plane (x,y), if a two-dimensional coordinate point (0,0) is taken as the centre, the common 2D Gaussian distribution function G(x,y) can be expressed as,

$$G(x,y)=\frac{2}{2\pi\sigma^2}e^{-\frac{(x^2+y^2)}{2\sigma^2}}, \qquad \text{(B-1)}$$

where σ is the variance of (x,y). Similarly, if a two-dimensional coordinate point (u,v) is taken as the centre, the 2D Gaussian distribution function can be

expressed as,

$$G(x,y)=\frac{2}{2\pi\sigma^2}e^{-\frac{((x-u)^2+(y-v)^2)}{2\sigma^2}}. \quad \text{(B-2)}$$

Initially, we identify each pixel point (u,v) within the raw image whose grey value is non-zero. Subsequently, Eq. (B-2) is employed to compute the Gaussian distribution corresponding to these identified pixel points across the entire image. Ultimately, the summation of all Gaussian distributions is applied to the raw image, resulting in the final image.

Appendix B.3 Supplementary information: Information entropy

For a discrete random variable x, its information entropy $H(x)$ can be expressed as,

$$H(x)=-\sum_{i=1}^{m}p_i(x)\log_2 p_i(x), \quad \text{(B-3)}$$

where m is the number of possibilities and $p_i(x)$, i=1,2,3,…,m, represents the probability of each case. For an image, where x represents the grey value, $p_i(x)$ corresponds to the ratio of the occurrences of x to the total number of occurrences. Therefore, by analyzing the grayscale histogram of a captured photo, $p_i(x)$ can be calculated for each grey value, allowing for the determination of the information entropy of the photo.

Specifically, we captured five images for each scenario (corresponding to each object distance and light condition). Following the subtraction of the background image, the information entropy of these five images is computed. Subsequently, we calculate the mean information entropy value and associated errors for each condition, as illustrated in Figures.

Appendix B.4 Supplementary information: Calculation of maximum angular velocities

Appendix B.4.1 Using a CMOS chip as the photodetection unit

In our experimental configuration (Fig. 5-7a), the motion of the object is simulated using five equally spaced and successively triggered LEDs. The time delay Δt_1, during which an object traverses from one side of the dome to the opposite side, can be determined based on the FOV and the angular speed ω, as outlined below:

$$\Delta t_1 = \frac{\mathrm{FOV}}{\omega}. \tag{B-4}$$

The motion of the object is replicated using 5 successively triggered LEDs; therefore, the time delay Δt_1 must exceed or be equal to the response time Δt_{dec} of the photodetector.

$$\Delta t_1 \geq \Delta t_{dec}. \tag{B-5}$$

The combination of Eqs. (B-4) and (B-5) yields

$$\omega \leq \frac{\mathrm{FOV}}{\Delta t_{dec}}, \tag{B-6}$$

and, hence, the maximum angular velocity is determined by

$$\omega_{\max} = \frac{\mathrm{FOV}}{\Delta t_{dec}}. \tag{B-7}$$

The response time (33.3 ms) of a CMOS chip (30 Hz frame rate) determines the highest angular perception speed:

$$\omega_{\max} = \frac{180°}{33.3\times10^{-3}} = 5.4\times10^{3}\ \mathrm{deg/s}. \tag{B-8}$$

Appendix B.4.2 Using a photodiode array as the photodetection unit

When utilizing a photodiode array containing 5 electromagnetically shielded photodiodes (ElecFans) for photodetection, the response time is 40 μs (equivalent to 25 kHz). In such instances, the maximum angular perception speed is

$$\omega_{\max} = \frac{\mathrm{FOV}}{\Delta t_{dec}} = \frac{180°}{40\times10^{-6}} = 4.5\times10^{6}\ \mathrm{deg/s}. \quad \text{(B-9)}$$

Appendix B.5 Supplementary videos

Supplementary Video B-1: OSACE detects two objects that are placed at angular positions of 40º and -40º with a fixed distance D_A or a varying distance D_B under different light intensities. When the light intensity is ample (approximately 25, 50, and 100 Lux), a 15ms exposure time is adequate to capture clear images. However, under very low light conditions (0.1 Lux), both spatial and temporal approaches are required for imaging. When the distances to both objects are equal, their respective image sizes are identical. As the distance D_B increases, the size of object B decreases; conversely, as D_B decreases, the size of object B increases. Despite variations in object distance affecting image size, focus remains consistently maintained.

Supplementary Video B-2: Dynamic angular perception experiment utilizing a conventional CMOS imaging chip as the photodetector under hierarchical light intensities. Five LEDs are sequentially illuminated in an evenly arranged manner over 180º, mimicking an object with rapid angular velocity under varying light conditions. The CMOS chip, with a frame rate of 30 Hz, equates to an angular velocity of 5.4×10^3 deg/s.

Supplementary Video B-3: Ultrafast perception of angular motion utilizing a photodiode array comprising 5 electromagnetically shielded photodiodes under hierarchical background light intensities. Under each background light intensity (0, 10, 50, 100 Lux), the emitted light from flickering LEDs (representing a moving object) is captured by photodiodes. The numerical annotation beneath each sub-video denotes the specific photodiode depicted in the right corner, capturing the emitted signal from the respective LED. The maximum detection frequency reaches 25 kHz, associated with an angular velocity of 4.5×10^6 deg/s.

Reference

[1] M. S. Kim, J. E. Yeo, H. Choi, S. Chang, D. H. Kim, and Y. M. Song, "Evolution of natural eyes and biomimetic imaging devices for effective image acquisition," *Journal of Materials Chemistry C,* vol. 11, no. 36, pp. 12083-12104, 2023.

[2] M. J. Klowden, "CHAPTER 11 - Nervous Systems," in *Physiological Systems in Insects (Second Edition)*, M. J. Klowden Ed. San Diego: Academic Press, 2008, pp. 523-595.

[3] J. Chen *et al.*, "Optoelectronic graded neurons for bioinspired in-sensor motion perception," *Nature Nanotechnology,* pp. 1-7, 2023.

[4] R. Miall, "The flicker fusion frequencies of six laboratory insects, and the response of the compound eye to mains fluorescent 'ripple'," *Physiological Entomology,* vol. 3, no. 2, pp. 99-106, 1978.

[5] D. Kelly and H. Wilson, "Human flicker sensitivity: two stages of retinal diffusion," *Science,* vol. 202, no. 4370, pp. 896-899, 1978.

[6] M. Ma *et al.*, "Super-resolution and super-robust single-pixel superposition compound eye," *Optics and Lasers in Engineering,* vol. 146, p. 106699, 2021.

[7] Y. M. Song *et al.*, "Digital cameras with designs inspired by the arthropod eye," *Nature,* vol. 497, no. 7447, pp. 95-99, 2013.

[8] M. Lee *et al.*, "An amphibious artificial vision system with a panoramic visual field," *Nature Electronics,* vol. 5, no. 7, pp. 452-459, 2022.

[9] M. Ma *et al.*, "Target orientation detection based on a neural network with a bionic bee-like compound eye," *Optics Express,* vol. 28, no. 8, pp. 10794-10805, 2020.

[10] R. Hooke, *Micrographia, or Some Physiological Descriptions of Minute Bodies, made by Magnifying Glasses, with Observations and Inquiries thereupon*. Printers to Council of the Royal Society of London, 1665.

[11] S. Exner, *Die Physiologie der facettirten Augen von Krebsen und Insecten: eine Studie*. Franz Deuticke, 1891.

[12] M. Land, "Compound eyes: old and new optical mechanisms," *Nature,* vol. 287, no. 5784, pp. 681-686, 1980.

[13] L. P. Lee and R. Szema, "Inspirations from biological optics for advanced photonic systems," *Science,* vol. 310, no. 5751, pp. 1148-1150, 2005.

[14] J. Chen et al., "Optoelectronic graded neurons for bioinspired in-sensor motion perception," *Nature Nanotechnology*, vol. 18, no. 8, pp. 882-888, 2023.

[15] R. De Ruyter van Steveninck and S. Laughlin, "The rate of information transfer at graded-potential synapses," *Nature*, vol. 379, no. 6566, pp. 642-645, 1996.

[16] W. L. Liang, J. G. Pan, and G. D. J. Su, "One-lens camera using a biologically based artificial compound eye with multiple focal lengths," *Optica,* vol. 6, no. 3, pp. 326-334, 2019.

[17] K. Kagawa, K. Yamada, E. Tanaka, and J. Tanida, "A three-dimensional multifunctional compound-eye endoscopic system with extended depth of field," *Electronics and Communications in Japan,* vol. 95, no. 11, pp. 14-27, 2012.

[18] J. Lecoeur, E. Baird, and D. Floreano, "Spatial encoding of translational optic flow in planar scenes by elementary motion detector arrays," *Scientific Reports,* vol. 8, no. 1, pp. 5821, 2018.

[19] J. M. Ong and L. da Cruz, "The bionic eye: a review," *Clinical & Experimental Ophthalmology,* vol. 40, no. 1, pp. 6-17, 2012.

[20] P. Nussbaum, R. Voelkel, H. P. Herzig, M. Eisner, and S. Haselbeck, "Design, fabrication and testing of microlens arrays for sensors and microsystems," *Pure and Applied Optics: Journal of the European optical society part A,* vol. 6, no. 6, pp. 617, 1997.

[21] A. Brückner, J. Duparré, R. Leitel, P. Dannberg, A. Bräuer, and A. Tünnermann, "Thin wafer-level camera lenses inspired by insect compound eyes," *Optics Express,* vol. 18, no. 24, pp. 24379-24394, 2010.

[22] J. Tanida *et al.*, "Thin observation module by bound optics (TOMBO): an optoelectronic image capturing system," in *Optics in Computing 2000*, 2000, vol. 4089: SPIE, pp. 1030-1036.

[23] M. Shankar *et al.*, "Ultra-thin multiple-channel LWIR imaging systems," in *Infrared and Photoelectronic Imagers and Detector Devices II*, 2006, vol. 6294: SPIE, pp. 298-307.

[24] H. Ren and S. T. Wu, "Tunable-focus liquid microlens array using dielectrophoretic effect," *Optics Express,* vol. 16, no. 4, pp. 2646-2652, 2008.

[25] C. Y. Fan, C. P. Lin, and G. D. J. Su, "Ultrawide-angle and high-efficiency metalens in hexagonal arrangement," *Scientific Reports,* vol. 10, no. 1, pp. 15677, 2020.

[26] Z. B. Fan et al., "A broadband achromatic metalens array for integral imaging in the visible," *Light: Science & Applications*, vol. 8, no. 1, pp. 67,

2019.

[27] A. Salmanogli, H. S. Geçm, and E. Piskin, "Plasmonic system as a compound eye: image point-spread function enhancing by entanglement," *IEEE Sensors Journal,* vol. 18, no. 14, pp. 5723-5731, 2018.

[28] L. C. Kogos, Y. Li, J. Liu, Y. Li, L. Tian, and R. Paiella, "Plasmonic ommatidia for lensless compound-eye vision," *Nature Communications,* vol. 11, no. 1, pp. 1637, 2020.

[29] L. Li, Y. Hao, J. Xu, F. Liu, and J. Lu, "The design and positioning method of a flexible zoom artificial compound eye," *Micromachines,* vol. 9, no. 7, pp. 319, 2018.

[30] D. Wu *et al.*, "Bioinspired fabrication of high-quality 3D artificial compound eyes by voxel-modulation femtosecond laser writing for distortion-free wide-field-of-view imaging," *Advanced Optical Materials,* vol. 2, no. 8, pp. 751-758, 2014.

[31] G. X. Jin, X. Y. Hu, Z. C. Ma, C. H. Li, Y.L. Zhang, and H. B. Sun, "Femtosecond laser fabrication of 3D templates for mass production of artificial compound eyes," *Nanotechnology and Precision Engineering (NPE),* vol. 2, no. 3, pp. 110-117, 2019.

[32] G. Lian *et al.*, "Fabrication and characterization of curved compound eyes based on multifocal microlenses," *Micromachines,* vol. 11, no. 9, pp. 854, 2020.

[33] D. Floreano *et al.*, "Miniature curved artificial compound eyes," *Proceedings of the National Academy of Sciences,* vol. 110, no. 23, pp. 9267-9272, 2013.

[34] W. B. Lee, H. Jang, S. Park, Y. M. Song, and H. N. Lee, "COMPU-EYE: a

high resolution computational compound eye," *Optics Express,* vol. 24, no. 3, pp. 2013-2026, 2016.

[35] R. Pericet-Camara *et al.*, "An artificial elementary eye with optic flow detection and compositional properties," *Journal of The Royal Society Interface,* vol. 12, no. 109, pp. 20150414, 2015.

[36] K. H. Jeong, J. Kim, and L. P. Lee, "Biologically inspired artificial compound eyes," *Science,* vol. 312, no. 5773, pp. 557-561, 2006.

[37] F. M. Reininger, "Fiber coupled artificial compound eye," U.S. Patent, 7 376 314 B2, May 20, 2008.

[38] R. Krishnasamy, P. Thomas, S. Pepic, W. Wong, and R. I. Hornsey, "Calibration techniques for object tracking using a compound eye image sensor," in *Unmanned/Unattended Sensors and Sensor Networks*, 2004, vol. 5611: SPIE, pp. 42-52.

[39] B. Dai *et al.*, "Biomimetic apposition compound eye fabricated using microfluidic-assisted 3D printing," *Nature Communications,* vol. 12, no. 1, pp. 6458, 2021.

[40] F. Liu *et al.*, "Artificial compound eye-tipped optical fiber for wide field illumination," *Optics Letters,* vol. 44, no. 24, pp. 5961-5964, 2019.

[41] Y. Cheng *et al*., "Reducing defocus aberration of a compound and human hybrid eye using liquid lens," *Applied Optics,* vol. 57, no. 7, pp. 1679-1688, 2018.

[42] K. Wei, H. Zeng, and Y. Zhao, "Insect–Human Hybrid Eye (IHHE): an adaptive optofluidic lens combining the structural characteristics of insect and human eyes," *Lab on a Chip,* vol. 14, no. 18, pp. 3594-3602, 2014.

[43] L. Wang *et al.*, "Graphene-based bioinspired compound eyes for

programmable focusing and remote actuation," *ACS Applied Materials & Interfaces,* vol. 7, no. 38, pp. 21416-21422, 2015.

[44] D. Zhu, C. Li, X. Zeng, and H. Jiang, "Hydrogel-actuated tunable-focus microlens arrays mimicking compound eyes," in *TRANSDUCERS 2009-2009 International Solid-State Sensors, Actuators and Microsystems Conference*, 2009: IEEE, pp. 2302-2305.

[45] Z. C. Ma *et al.*, "Smart compound eyes enable tunable imaging," *Advanced Functional Materials,* vol. 29, no. 38, pp. 1903340, 2019.

[46] E. Agi, M. Langen, S. J. Altschuler, L. F. Wu, T. Zimmermann, and P. R. Hiesinger, "The evolution and development of neural superposition," *Journal of Neurogenetics,* vol. 28, no. 3-4, pp. 216-232, 2014.

[47] M. F. Land, "Variations in the structure and design of compound eyes," in *Facets of Vision*: Springer, 1989, pp. 90-111.

[48] M. F. Land, "The optical structures of animal eyes," *Current Biology,* vol. 15, no. 9, pp. R319-R323, 2005. 10.1016/j.cub.2005.04.041

[49] K. Kirschfeld, "The absolute sensitivity of lens and compound eyes," *Zeitschrift für Naturforschung C,* vol. 29, no. 9-10, pp. 592-596, 1974.

[50] A. Fischer and G. Horstmann, "Fine structure of the eye of the meal moth, Ephestia kuehniella Zeller (Lepidoptera, Pyralididae)," *Zeitschrift für Zellforschung und Mikroskopische Anatomie,* vol. 116, pp. 275-304, 1971.

[51] S. R. Shaw, "Optics of arthropod compound eye," *Science,* vol. 165, no. 3888, pp. 88-90, 1969.

[52] S. Berry, "The use of optical coherence tomography to demonstrate dark and light adaptation in a live moth," *Environmental Entomology,* vol. 51, no. 4, pp. 643-648, 2022.

[53] E. J. Warrant, "Seeing better at night: life style, eye design and the optimum strategy of spatial and temporal summation," *Vision Research,* vol. 39, no. 9, pp. 1611-1630, 1999.

[54] R. Frederiksen and E. J. Warrant, "The optical sensitivity of compound eyes: theory and experiment compared," *Biology Letters,* vol. 4, no. 6, pp. 745-747, 2008.

[55] L. Li and Y. Y. Allen, "Microfabrication on a curved surface using 3D microlens array projection," *Journal of Micromechanics and Microengineering,* vol. 19, no. 10, pp. 105010, 2009.

[56] L. Li and Y. Y. Allen, "Development of a 3D artificial compound eye," *Optics Express,* vol. 18, no. 17, pp. 18125-18137, 2010.

[57] M. C. Ma, F. Guo, Z. L. Cao, and K. Y. Wang, "Development of an artificial compound eye system for three-dimensional object detection," *Applied Optics,* vol. 53, no. 6, pp. 1166-1172, 2014.

[58] H. Deng *et al.*, "Catadioptric planar compound eye with large field of view," *Optics Express,* vol. 26, no. 10, pp. 12455-12468, 2018.

[59] M. C. Ma and K. Y. Wang, "Improvement on object detection accuracy by using two compound eye systems," in *7th International Symposium on Advanced Optical Manufacturing and Testing Technologies: Optical Test and Measurement Technology and Equipment*, 2014, vol. 9282: SPIE, pp. 100-106.

[60] J. Z. He, H. J. Jian, Q. T. Zhu, M. C. Ma, and K. Y. Wang, "Matching between the light spots and lenslets of an artificial compound eye system," in *Aopc 2017: 3d Measurement Technology for Intelligent Manufacturing*, 2017, vol. 10458: SPIE, pp. 44-53.

[61] M. C. Ma, X. C. Gao, J. Zhang, and H. X. Deng, "Design of a compound eye system with planar micolens array and curved folded mirrors," in *8th International Symposium on Advanced Optical Manufacturing and Testing Technologies: Optical Test, Measurement Technology, and Equipment*, 2016, vol. 9684: SPIE, pp. 100-107.

[62] M. C. Ma *et al.*, "Design and optical characterization of compound eye type solar concentrator," *Results in Optics,* vol. 6, pp. 100202, 2022.

[63] G. M. Gibson, S. D. Johnson, and M. J. Padgett, "Single-pixel imaging 12 years on: a review," *Optics Express,* vol. 28, no. 19, pp. 28190-28208, 2020.

[64] O. I. Abiodun, A. Jantan, A. E. Omolara, K. V. Dada, N. A. Mohamed, and H. Arshad, "State-of-the-art in artificial neural network applications: A survey," *Heliyon,* vol. 4, no. 11, 2018.

[65] A. O. Govorov and H. H. Richardson, "Generating heat with metal nanoparticles," *Nano Today,* vol. 2, no. 1, pp. 30-38, 2007.

[66] G. L. Hornyak, C. J. Patrissi, and C. R. Martin, "Fabrication, characterization, and optical properties of gold nanoparticle/porous alumina composites: The nonscattering maxwell− garnett limit," *The Journal of Physical Chemistry B,* vol. 101, no. 9, pp. 1548-1555, 1997.

[67] A. W. Adamson, "An adsorption model for contact angle and spreading," *Journal of Colloid and Interface Science,* vol. 27, no. 2, pp. 180-187, 1968.

[68] A. W. Adamson, "Potential distortion model for contact angle and spreading. II. Temperature dependent effects," *Journal of Colloid and Interface Science,* vol. 44, no. 2, pp. 273-281, 1973.

[69] S. Wei *et al.*, "Protein-based 3D microstructures with controllable morphology and pH-responsive properties," *ACS Applied Materials &*

Interfaces, vol. 9, no. 48, pp. 42247-42257, 2017.

[70] C. L. Lay, M. R. Lee, H. K. Lee, I. Y. Phang, and X. Y. Ling, "Transformative two-dimensional array configurations by geometrical shape-shifting protein microstructures," *ACS Nano,* vol. 9, no. 10, pp. 9708-9717, 2015.

[71] B. P. Chan, J. N. Ma, J. Y. Xu, C. W. Li, J. P. Cheng, and S. H. Cheng, "Femto-second laser-based free writing of 3D protein microstructures and micropatterns with sub-micrometer features: a study on voxels, porosity, and cytocompatibility," *Advanced Functional Materials,* vol. 24, no. 3, pp. 277-294, 2014.

[72] E. T. Ritschdorff, R. Nielson, and J. B. Shear, "Multi-focal multiphoton lithography," *Lab on a Chip,* vol. 12, no. 5, pp. 867-871, 2012.

[73] S. Huang, L. Wang, Y. Zheng, Y. Su, and F. Wang, "A simple process optimization route to fabricate curved bionic compound eye array," in *IOP Conference Series: Materials Science and Engineering*, 2020, vol. 892, no. 1: IOP Publishing, pp. 012099.

[74] J. Li *et al*., "Fabrication of artificial compound eye with controllable field of view and improved imaging," *ACS Applied Materials & Interfaces,* vol. 12, no. 7, pp. 8870-8878, 2020.

[75] R. R. Gattass and E. Mazur, "Femtosecond laser micromachining in transparent materials," *Nature Photonics,* vol. 2, no. 4, pp. 219-225, 2008.

[76] L. Zhu, Y. Gao, X. Hu, Z. Ma, and W. Zhang, "Progress in femtosecond laser fabrication of artificial compound eye," *Chin. Sci. Bull,* vol. 64, no. 12, pp. 1254-1267, 2019.

[77] J. J. Cao, Z. S. Hou, Z. N. Tian, J. G. Hua, Y. L. Zhang, and Q. D. Chen,

"Bioinspired zoom compound eyes enable variable-focus imaging," *ACS Applied Materials & Interfaces,* vol. 12, no. 9, pp. 10107-10117, 2020.

[78] K. Yamada, T. Asano, J. Tanida, R. Shougenji, and T. Nagakura, "Development of three dimensional endoscope by compound optics," in *European Conference on Biomedical Optics*, 2005: Optica Publishing Group, pp. SuD5.

[79] K. Kagawa, R. Shogenji, E. Tanaka, K. Yamada, S. Kawahito, and J. Tanida, "Variable field-of-view visible and near-infrared polarization compound-eye endoscope," in *2012 Annual International Conference of the IEEE Engineering in Medicine and Biology Society*, 2012: IEEE, pp. 3720-3723.

[80] K. Kagawa, E. Tanaka, K. Yamada, S. Kawahito, and J. Tanida, "Deep-focus compound-eye camera with polarization filters for 3D endoscopes," in *Three-Dimensional and Multidimensional Microscopy: Image Acquisition and Processing XIX*, 2012, vol. 8227: SPIE, pp. 185-192.

[81] K. Kagawa *et al.*, "A compact shape-measurement module based on a thin compound-eye camera with multiwavelength diffractive pattern projection for intraoral diagnosis," in *Optics and Photonics for Information Processing III*, 2009, vol. 7442: SPIE, pp. 235-242.

[82] K. Kim, K. W. Jang, H. K. Kim, S. Bean Cho, and K. H. Jeong, "Biologically inspired intraoral camera for multifunctional dental imaging," *Journal of Optical Microsystems,* vol. 2, no. 3, pp. 031202-031202, 2022.

[83] K. Kagawa *et al.*, "An active intraoral shape measurement scheme using a compact compound-eye camera with integrated pattern projectors," *Japanese Journal of Applied Physics,* vol. 48, no. 9S2, pp. 09LB04, 2009.

[84] R. Voelkel, H. P. Herzig, P. Nussbaum, R. Daendliker, and W. B. Hugle,

"Microlens array imaging system for photolithography," *Optical Engineering,* vol. 35, no. 11, pp. 3323-3330, 1996.

[85] R. Leitel *et al.*, "Curved artificial compound-eyes for autonomous navigation," in *Micro-Optics 2014*, 2014, vol. 9130: SPIE, pp. 109-119.

[86] H. Yoo, G. Cha, and S. Oh, "Deep ego-motion classifiers for compound eye cameras," *Sensors,* vol. 19, no. 23, pp. 5275, 2019.

[87] K. Pang, F. Fang, L. Song, Y. Zhang, and H. Zhang, "Bionic compound eye for 3D motion detection using an optical freeform surface," *JOSA B,* vol. 34, no. 5, pp. B28-B35, 2017.

[88] J. C. Zufferey, A. Beyeler, and D. Floreano, "Autonomous flight at low altitude using light sensors and little computational power," *International Journal of Micro Air Vehicles,* vol. 2, no. 2, pp. 107-117, 2010.

[89] A. Beyeler, J. C. Zufferey, and D. Floreano, "Vision-based control of near-obstacle flight," *Autonomous Robots,* vol. 27, no. 3, pp. 201-219, 2009.

[90] H. Dahmen and H. A. Mallot, "Odometry for ground moving agents by optic flow recorded with optical mouse chips," *Sensors,* vol. 14, no. 11, pp. 21045-21064, 2014.

[91] S. Tuli *et al.*, "Next generation technologies for smart healthcare: challenges, vision, model, trends and future directions," *Internet Technology Letters,* vol. 3, no. 2, pp. e145, 2020.

[92] R. Boutteau, R. Rossi, L. Qin, P. Merriaux, and X. Savatier, "A vision-based system for robot localization in large industrial environments," *Journal of Intelligent & Robotic Systems,* vol. 99, pp. 359-370, 2020.

[93] N. Al Said, Y. Gorbachev, and A. Avdeenko, "An unmanned aerial vehicles navigation system on the basis of pattern recognition applications—Review

of implementation options and prospects for development," *Software: Practice and Experience,* vol. 51, no. 7, pp. 1509-1517, 2021.

[94] K. C. Kao and G. A. Hockham, "Dielectric-fibre surface waveguides for optical frequencies," in *Proceedings of the Institution of Electrical Engineers*, 1966, vol. 113, no. 7: IET, pp. 1151-1158.

[95] E. Säckinger, *Broadband Circuits for Optical Fiber Communication*. John Wiley & Sons, Inc., 2005.

[96] B. Lee, "Review of the present status of optical fiber sensors," *Optical Fiber Technology,* vol. 9, no. 2, pp. 57-79, 2003.

[97] B. A. Flusberg, E. D. Cocker, W. Piyawattanametha, J. C. Jung, E. L. Cheung, and M. J. Schnitzer, "Fiber-optic fluorescence imaging," *Nature Methods,* vol. 2, no. 12, pp. 941-950, 2005.

[98] S.-Y. Lee, V. J. Parot, B. E. Bouma, and M. Villiger, "Efficient dispersion modeling in optical multimode fiber," *Light: Science & Applications,* vol. 12, no. 1, p. 31, 2023.

[99] M. Kim, W. Choi, Y. Choi, C. Yoon, and W. Choi, "Transmission matrix of a scattering medium and its applications in biophotonics," *Optics Express,* vol. 23, no. 10, pp. 12648-12668, 2015.

[100] R. Takagi, R. Horisaki, and J. Tanida, "Object recognition through a multi-mode fiber," *Optical Review,* vol. 24, pp. 117-120, 2017.

[101] L. Lei, N. Wang, X. Zhang, Q. Tai, D. P. Tsai, and H. L. Chan, "Optofluidic planar reactors for photocatalytic water treatment using solar energy," *Biomicrofluidics,* vol. 4, no. 4, p. 043004, 2010.

[102] D. Bartolo, G. Degré, P. Nghe, and V. Studer, "Microfluidic stickers," *Lab on a Chip,* vol. 8, no. 2, pp. 274-279, 2008.

[103] C. Darwin, *On the Origin of Species by Means of Natural Selection, or the Preservation of Favoured Races in the Struggle for Life*. John Murray, 1859.

[104] K. Shinomiya *et al.*, "The organization of the second optic chiasm of the Drosophila optic lobe," *Frontiers in Neural Circuits,* vol. 13, p. 65, 2019.

[105] J. Duparré, P. Dannberg, P. Schreiber, A. Bräuer, and A. Tünnermann, "Thin compound-eye camera," *Applied Optics,* vol. 44, no. 15, pp. 2949-2956, 2005.

[106] R. Dudley, *The Biomechanics of Insect Flight: Form, Function, Evolution Ch. 5*. Princeton University Press, 2000.

[107] H. L. Phan *et al.*, "Artificial compound eye systems and their application: A review," *Micromachines,* vol. 12, no. 7, p. 847, 2021.

[108] Z. Deng *et al.*, "Dragonfly-eye-inspired artificial compound eyes with sophisticated imaging," *Advanced Functional Materials,* vol. 26, no. 12, pp. 1995-2001, 2016.

[109] J. Chapman, "Ommatidia numbers and eyes in scolytid beetles," *Annals of the Entomological Society of America,* vol. 65, no. 3, pp. 550-553, 1972.

[110] M. Subbarao and N. Gurumoorthy, "Depth recovery from blurred edges," in *Proceedings CVPR'88: The Computer Society Conference on Computer Vision and Pattern Recognition*, 1988: IEEE Computer Society, 1988, pp. 498-503.

[111] M. Subbarao and G. Surya, "Depth from defocus: A spatial domain approach," *International Journal of Computer Vision,* vol. 13, no. 3, pp. 271-294, 1994.

[112] B. D. Lucas and T. Kanade, *An Iterative Image Registration Technique with an Application to Stereo Vision*. Vancouver, 1981.

[113] D. J. Fleet and K. Langley, "Recursive filters for optical flow," *IEEE Transactions on Pattern Analysis and Machine Intelligence,* vol. 17, no. 1, pp. 61-67, 1995.

[114] M. Juusola, A. S. French, R. O. Uusitalo, and M. Weckström, "Information processing by graded-potential transmission through tonically active synapses," *Trends in Neurosciences,* vol. 19, no. 7, pp. 292-297, 1996.

[115] K. Stollberg, A. Brückner, J. Duparré, P. Dannberg, A. Bräuer, and A. Tünnermann, "The Gabor superlens as an alternative wafer-level camera approach inspired by superposition compound eyes of nocturnal insects," *Optics Express,* vol. 17, no. 18, pp. 15747-15759, 2009.

[116] A. Brückner, J. Duparré, P. Dannberg, A. Bräuer, and A. Tünnermann, "Artificial neural superposition eye," *Optics Express,* vol. 15, no. 19, pp. 11922-11933, 2007.

[117] S. Hiura, A. Mohan, and R. Raskar, "Krill-eye: Superposition compound eye for wide-angle imaging via grin lenses," *IPSJ Transactions on Computer Vision and Applications,* vol. 2, pp. 186-199, 2010.

[118] D.-Y. Tsai, Y. Lee, and E. Matsuyama, "Information Entropy Measure for Evaluation of Image Quality," *Journal of Digital Imaging,* vol. 21, no. 3, pp. 338-347, 2008/09/01 2008.

[119] B. Horn, B. Klaus, and P. Horn, *Robot vision*. MIT press, 1986.

[120] A. P. Pentland, "A new sense for depth of field," *IEEE Transactions on Pattern Analysis and Machine Intelligence,* no. 4, pp. 523-531, 1987.